Clays and Clay Minerals, Vol. 62, No. 3, 161–173, 2014.

INTERACTIONS OF RADIOACTIVE AND STABLE CESIUM WITH HYDROXY-INTERLAYERED VERMICULITE GRAINS IN SOILS OF THE SAVANNAH RIVER SITE, SOUTH CAROLINA, USA

MOMOKO GOTO[1,†], ROBERT ROSSON[2], W. CRAWFORD ELLIOTT[3], J. M. WAMPLER[3,4,*], STEVEN SERKIZ[5,6], AND BERND KAHN[1,2]

[1] Woodruff School of Mechanical Engineering, Georgia Institute of Technology, Atlanta, GA 30332-0405, USA
[2] Environmental Radiation Center, EOSL, GTRI, Georgia Institute of Technology, Atlanta, GA 30332-0826, USA
[3] Department of Geosciences, Georgia State University, Atlanta, GA 30302-4105, USA
[4] School of Earth and Atmospheric Sciences, Georgia Institute of Technology, Atlanta, GA 30332-0340, USA
[5] Savannah River National Laboratory, Aiken, SC, 29808, USA
[6] Environmental Engineering and Earth Sciences, Clemson University, Clemson, SC 29634, USA

Abstract—Sorption and fixation of Cs by the upland soils of the US Department of Energy's Savannah River Site (SRS) have been attributed to micaceous grains consisting mostly of hydroxy-interlayered vermiculite (HIV). Results of experiments to characterize SRS soil samples, to examine aspects of their radiocesium sorption, and to determine how much of their natural Cs is accessible for chemical extraction and isotope dilution are presented in support of mechanistic hypotheses to explain Cs sorption and fixation in HIV grains. The HIV is responsible for most of the soil cation exchange capacity, and concentrations of naturally occurring Cs, Rb, and K in soil samples are closely related to the concentration of HIV. Experiments with ^{137}Cs to examine (1) sorption kinetics, (2) blocking of exchange sites with silver thiourea, and (3) susceptibility of sorbed ^{137}Cs to chemical extraction, support the idea that added Cs is sorbed at different kinds of cation exchange sites in HIV grains. Sites highly selective for Cs but relatively few in number are inferred to exist in interlayer wedge zones within such grains. Little of the naturally occurring Cs in the soil samples was extractable by chemical agents that would remove Cs from ordinary cation-exchange sites and from within non-silicate soil components. Furthermore, most of the natural Cs was inaccessible for isotope dilution under slightly acidic conditions approximating the natural soil environment. These observations support the idea that most of the Cs in these soils has become effectively fixed in the narrower parts of interlayer wedge zones. Control of Cs uptake and fixation by highly Cs-selective interlayer wedge sites would account for the large distribution coefficients found for ^{137}Cs at the low aqueous Cs concentrations typical of environmental systems and also for the relatively large concentrations of stable Cs in the SRS soils.

Key Words—Hydroxy-interlayered Vermiculite, Interlayer Wedge Zones, Isotope Dilution, Natural Cesium, Radiocesium, Savannah River Site, Soil, Sorption.

INTRODUCTION

Sorption of ^{137}Cs in soil has been studied widely because it is a major fission product that exists in the environment as a consequence of fallout from nuclear weapon tests, discharges from nuclear facilities, and seepage from radioactive waste basins. Extensive handling and storage of ^{137}Cs at the U.S. Department of Energy's Savannah River Site (SRS) has stimulated attempts to predict its retention by soil and the extent of its subsurface movement. Interactions of ^{137}Cs with SRS soils and sediments have been studied since soon after plant operations began about 60 years ago (Prout, 1958; NCRP, 2006).

* E-mail address of corresponding author:
wampler@eas.gatech.edu
† Current name and affiliation: Momoko Tajiri, Department of Chemistry, Michigan Technological University, Houghton, MI 49931, USA
DOI: 10.1346/CCMN.2014.0620301

Kaolinite and hydroxy-interlayered vermiculite (HIV) are by mass the predominant clay minerals in the sandy coastal-plain soils of the southeastern U.S. (Harris *et al*. 1992a), including the upland soils that occupy most of the SRS area (Ruhe and Matney, 1980; Kaplan *et al*., 1996, 1997; Segall *et al*., 2000). They are also the predominant phyllosilicates in the fine fractions of bottom sediments from SRS streams (Elprince *et al*., 1977). Favored Cs sorption within interlayer wedge zones of hydroxy-interlayered clay, where expanded interlayers grade into the closed interlayers characteristic of mica, has been considered equivalent to the well known high selectivity for Cs in wedge zones at frayed edges of illite particles (Elprince *et al*., 1977). In highly weathered micaceous particles that are now mostly HIV [hereinafter, HIV grains], interlayer wedge sites should have much greater affinity for Cs than the sites on or between the planar structural layers, but these interlayer wedge sites are relatively few in number (Rich and Black, 1964; Barnhisel and Bertsch, 1989).

Cs solid-liquid distribution coefficients for five SRS soil samples were determined by Goto *et al*. (2008). The values

varied widely, from 2600 dm^3 kg^{-1} to 4.7 dm^3 kg^{-1}, with variations in pH, amounts of added Cs and Na, and cation exchange capacity (CEC) of the soil. Equilibrium constants, based on the CEC, ion concentrations in solution, and Freundlich isotherm exponents were the same for all five soils, however, and permitted prediction of distribution coefficients within 50%. The Cs sorption by the SRS soils was inferred by Goto *et al*. (2008) to be primarily by HIV grains and to occur at distinctly different types of ion exchange sites, including relatively few interlayer wedge sites that are highly selective for Cs. The Cs/K ratios in the same five SRS soil samples were found by Wampler *et al.* (2012) to be notably larger than the Cs/K ratio for the upper continental crust and larger than that ratio in soils from other regions of the U.S. Those authors presented evidence that only ~2% of the SRS soil Cs is native to the mica remnants in HIV grains and attributed the high Cs/K ratios to uptake and fixation of naturally occurring Cs in interlayer wedge zones of HIV grains during pedogenesis. K-Ar age values of ~300 million years were determined by Naumann *et al.* (2012) for clay fractions of the same soil samples, providing direct support for the idea (Harris *et al*., 1992a) that nanoscale remnants of the original mica are present in HIV grains that formed by extensive weathering of detrital mica.

The research reported herein is complementary to the work reported by Goto *et al*. (2008), Wampler *et al*. (2012), and Naumann *et al*. (2012). In the present study, two hypotheses developed during the earlier studies were addressed by establishing the mineralogical character of the soil samples and by examining additional aspects of the behavior of Cs in the soils. The first hypothesis is that sorption of Cs by the SRS soils is primarily by HIV grains at two or more kinds of sites, including highly Cs-selective sites in interlayer wedge zones (Goto *et al*., 2008). The second is that Cs sorbed by HIV grains becomes fixed by slow migration into the narrower parts of the interlayer wedge zones (Wampler *et al*., 2012). Specifically described are results of: (1) soil characterization experiments to provide semi-quantitative values for HIV content of the soil clay, so the relationship of Cs, Rb, and K contents to HIV content could be examined; (2) experiments on Cs-uptake kinetics and on the blocking of Cs uptake by silver thiourea (AgTU), to provide insight into the character of the cation exchange sites of HIV grains; (3) sequential extractions of both recently added Cs and naturally occurring Cs, to provide information on how these were distributed in soil materials; and (4) an analysis of published data, to show by isotope dilution the amount of natural Cs in sites accessible to added aqueous Cs.

MATERIALS AND METHODS

Materials

The five near-surface soil samples tested in the present study are from five soil series considered representative of soil groups that occupy about three-fourths of the SRS area (Rogers, 1990). The samples were collected from uncontaminated site areas in 1996 (Findley, 1998; for locations see Goto, 2001, figure 4-1) from depths that correspond (Looney *et al*., 1990) to the B horizons of the Fuquay, Orangeburg, and Vaucluse series; to the E horizon of the Blanton series; and to the C horizon of the Lakeland series. The soils are acidic and have small clay contents and correspondingly small CEC values (Table 1).

Soil characterization

Test portions of the soil samples were treated with Na acetate-acetic acid solution (pH 5) to remove any carbonate cementing agents; Fe oxides were removed by the citrate-bicarbonate-dithionate method (Kunze and Dixon, 1986). The remaining solids were then separated by timed sedimentation into sand (>50 μm), silt (2−50 μm), and clay (<2 μm) fractions on the basis of procedures and settling tables provided by Jackson (1969). The separated fractions were oven-dried at 50ºC and then weighed to determine the mass of each relative to the total. [The mass fraction of the clay only was reported by Goto *et al*. (2008).] Potassium was determined on portions of the bulk soil samples (3−5 decigrams, dg) and of the clay fractions (0.5−1.5 dg) by flame atomic absorption spectrophotometry of test solutions prepared after digestion of the silicates in a mixture of HF, HNO_3, and $HClO_4$. After excess acids had been evaporated from the digestates, each residue was taken up in a weighed amount of an acidic CsCl solution (0.1 mol kg^{-1} HNO_3, 0.01 mol kg^{-1} CsCl, both reagent grade). The Cs served as an ionization suppressant in the flame. Readings of absorbance at 766.5 nm for these test solutions were compared with those for reference solutions of known K concentration prepared from standard KCl (SRM 999, US National Institute of Standards and Technology).

A portion of each Na^+-saturated clay fraction was deposited from slurry onto a glass slide for X-ray diffraction (XRD) measurements after, successively, (1) air drying, (2) ethylene-glycol saturation for 24 h at room temperature, and (3) heating to 550ºC for 1 h. Another portion of each clay fraction was saturated with K^+ (KCl, 1 mol dm^{-3}) before deposition on a slide for XRD measurements after, successively, (1) air drying and (2) heating at 300ºC for 1 h. CuKα radiation (Philips Model 12045 generator) diffracted by the oriented clay was filtered with a graphite monochromator. A theta-compensating slit was used to maintain constant the area of clay irradiated by the X-ray beam. Diffraction data were recorded from 2 to 32º2θ in steps of 0.02º2θ for either 1.0 s or 2.0 s per step controlled by an MDI Databox (Materials Data, Inc., Livermore, California, USA).

Semi-quantitative values for the proportions of kaolinite, HIV, and quartz in the clay fractions of the

Table 1. Sample properties from previous studies.

Soil series	Sample number*	Depth* (cm)	pH*	Sand* (%)	Silt* (%)	Clay – (%) –		CEC (cmol kg^{-1})		Cs — (mg kg^{-1}) —		K‡ (g kg^{-1})	K in clay§ (g kg^{-1})
Fuquay	42	122–152	5.29	76	7	18*	17.8†	2.0*	2.2†	5.3*	4.5†	4.2‡	1.37	5.9
Orangeburg	46	56–81	5.60	76	8	16*	13.9†	1.7*		3.8*	3.1†	2.9‡	1.12	5.2
Lakeland	2	51–76	5.06	88	6	6*	8.0†	0.5*		1.5*	1.1†	1.2‡	0.74	5.6
Blanton	35	25–51	5.13	92	6	2*	1.8†	0.5*	0.5†	1.5*	1.5†	1.2‡	0.55	8.3
Vaucluse	12	66–91	5.18	96	3	1*	1.6†	0.3*	0.5†	0.5*	0.9†	0.5‡	0.29	6.6

* Findley (1998)
† Goto *et al.* (2008)
‡ Wampler *et al.* (2012)
§ Naumann *et al.* (2012)

SRS soils were calculated from XRD peak heights by solution of three equations for each clay fraction,

$$w_1 = 1.07 w_3 h_1 / h_3, \quad (1)$$

$$w_2 = 0.6 w_3 h_2 / h_3, \text{ and} \quad (2)$$

$$w_1 + w_2 + w_3 + w_4 = 1 \quad (3)$$

where w_i denotes the mass fraction of mineral i in the clay fraction; the subscripts 1, 2, 3, and 4 denote HIV, quartz, kaolinite, and gibbsite, respectively; and h_1, h_2, and h_3 are the heights above background of the XRD peaks at 1.4 nm, 0.425 nm, and 0.71 nm, respectively. Equations 1 and 2 are based on equations 10 and 11 of Karathanasis and Hajek (1982), but h_3 was measured at 0.71 nm rather than at 0.70 nm and a factor 0.6 has been added to the right-hand term of equation 2 to correct for the relatively larger area of clay irradiated at 20.9º2θ through the theta-compensating slit used in the present study than through the 1º divergence slit used by Karathanasis and Hajek. To solve the equations for the unknown mass fractions, w_1, w_2, and w_3 required a value for w_4, the mass fraction of gibbsite, for each clay fraction. The values used for gibbsite content were 15% for the Orangeburg clay fraction and 10% for the Blanton clay fraction, as reported by Kaplan *et al.* (1997) for clay fractions from corresponding horizons, and an assumed value of 10% for the clay fractions of the other samples.

Cs-137 uptake kinetics

The rate of ^{137}Cs uptake at room temperature by bulk-soil portions of the Fuquay and Vaucluse soil samples, added with varying concentrations of stable Cs (^{133}Cs), was determined by shaking 1 g portions of soil with 40 cm^3 of 0.005 mol dm^{-3} $NaNO_3$ solution in closed plastic centrifuge tubes. Each contacting solution initially contained ~180 Bq of ^{137}Cs tracer, and ^{133}Cs as the chloride salt in one of the following amounts: (1) 0.62 nmol (the carrier in the ^{137}Cs solution); (2) an amount equivalent to ~2% of the cation exchange sites of the soil test portion (0.4 μmol for the Fuquay sample and 0.08 μmol for the Vaucluse sample); or (3) an amount equivalent to ~10% of the cation exchange sites (2 μmol and 0.4 μmol, respectively). Shaking was interrupted after periods ranging from 1 h to 175 h to remove a 1 cm^3 aliquot from each solution. Each aliquot was replaced with an equal volume of 0.005 mol dm^{-3} $NaNO_3$ solution. The 0.661 MeV γ-ray activity of ^{137}Cs in each aliquot was measured with a Ge detector and spectrometer system (Canberra Industries, Inc., Meriden, Connecticut, USA), calibrated with standard solutions of ^{137}Cs.

Blocking cesium sorption with silver thiourea

To determine the degree to which Cs uptake is blocked by the presence of AgTU in the exchange complex (Cremers *et al*., 1988), 1 g bulk-soil portions of the five soil samples were first saturated with AgTU, each by contact for 4 days in the dark with 40 cm^3 of a

solution containing 0.01 mol dm^{-3} $AgNO_3$ and 0.1 mol dm^{-3} thiourea, $SC(NH_2)_2$. The solids were then separated by centrifuging, washed with deionized water, and shaken at room temperature in solutions that contained ^{137}Cs and ^{133}Cs at the concentrations used in parallel experiments without AgTU described by Goto *et al.* (2008). The solutions, 40 cm^3 each, also contained $NaNO_3$ (0.001 mol dm^{-3}), $AgNO_3$ (0.01 mol dm^{-3}), and thiourea (0.1 mol dm^{-3}). The amounts of ^{137}Cs associated with the solids after 4 days were calculated from the difference between the initial and final amounts in solution, determined by measuring the 0.661 MeV γ-ray activity of solution aliquots with the calibrated Ge detector and spectrometer.

Sequential extraction

The sequential extraction scheme developed by Miller *et al.* (1986), as applied in the present study, was described by Goto (2001). The reagents and extraction conditions are tabulated with the results, below. Extractions were performed on six 1 g test portions of the Fuquay and Vaucluse soil samples. One of each was untreated bulk soil, one of each had been contacted at room temperature for 4 days with added ^{133}Cs (2.0 μmol for Fuquay soil and 40 nmol for Vaucluse soil) in 40 cm^3 of 0.001 mol dm^{-3} $NaNO_3$ solution and then separated from the solution, and one of each had been contacted with added ^{133}Cs as just described except that the solutions also contained ^{137}Cs (351 Bq). The treated, separated solids were stored moist for ~2 months before extraction. For the soil portions with no sorbed ^{137}Cs, the concentration of ^{133}Cs in solution after the original 4 days of sorption, in solutions from each of the seven extraction steps, and in solution after total dissolution of the residual solids, was determined by inductively coupled plasma mass spectrometry (Perkin-Elmer ELAN 5000, Waltham, Massachusetts, USA) against CsCl reference solutions of known Cs content. Measurement relative standard deviation was ~10%. For the soil portions with sorbed ^{137}Cs, the activity of ^{137}Cs in the solutions from the extractions was determined by measuring the 0.661 MeV γ-ray activity of solution aliquots with the calibrated Ge detector and spectrometer.

Cesium accessible for isotope dilution

Data from the 4-day Cs sorption experiments of Goto *et al.* (2008) were analyzed to determine how much of the soil Cs (naturally occurring stable Cs in the soil samples) isotopically diluted the radioactive Cs added during those experiments. Considering only the sorption data from those experiments in which added ^{133}Cs was minimal (carrier in the radioactive Cs), the amount of soil Cs accessible for isotope dilution (n_a) was calculated from

$$n_a = n_f A_i / A_f - n_i \quad (4)$$

where the amount (amount of substance) of ^{133}Cs is represented by n and activity (radioactivity) of ^{137}Cs is represented by A. The subscripts i and f refer to Cs in solution initially (the added Cs, which was in solution before the soil was introduced) and Cs in solution at the end of the experiment, respectively.

Equation 4 is appropriate for soil that contains no ^{137}Cs initially if the added Cs mixes fully and exclusively with the accessible component of the soil Cs, if no Cs isotope fractionation occurs, and if the decrease in amount of ^{137}Cs over the course of the experiment is negligible. The accessible fraction of the soil Cs is n_a/n_s, where n_s is the amount of soil Cs. Conversion of n_a to a mass value and division by the mass of dry soil would give an E value, where E, as commonly defined, is the 'isotopically exchangeable' amount of an element in soil, expressed as a mass fraction. No term equivalent to n_i is shown in equation 1 of Smolders *et al.* (1999) because their added radiocadmium was carrier-free.

RESULTS

Soil characteristics and clay mineralogy

Textural analyses (Table 2) confirmed that the soil samples consist predominantly of sand (75–96% by mass), with more clay than silt except for the Blanton

Table 2. Characteristics of the soil samples determined in the present study.

Sample	Sand	Silt	Minerals in clay fraction*			K	K in clay
			kaolinite	HIV	quartz		
	(% by mass)		—— (% by mass) ——			– (g kg^{-1}) –	
Fuquay #42	75.5	6.7	65	25	1	1.36	6.8
Orangeburg #46	78.3	7.8	65	20	0	1.11	5.5
Lakeland #2	86.1	5.9	65	25	0	0.71	6.7
Blanton #35	91.6	6.6	40	45	5	0.57	7.9
Vaucluse #12	95.8	2.6	50	35	2	0.26	7.7

* Because of the semiquantitative nature of the analysis, mineral mass fractions are rounded to the nearest 5% except for the low quartz values, which are rounded to the nearest 1%. As explained in the text, amounts of gibbsite, a fourth mineral in the clay fractions, were estimated to allow calculation of the mass fractions of kaolinite, HIV, and quartz.

and Vaucluse samples. New values for K content (Table 2) confirmed that the clay fractions consistently have <1% K by mass, and that K contents of the quartz-sand-rich bulk-soil samples are even smaller.

The results of XRD analysis showed that the clay fractions of the soils contain kaolinite, HIV, gibbsite, and in some cases quartz. Each of the XRD patterns for oriented, air-dried clay from the soil samples (Figure 1) shows a 1.4 nm peak that indicates the presence of smectite, vermiculite, or chlorite. Peaks at 0.71 nm and 0.36 nm correspond to higher-order basal reflections from the 1.4 nm clay mineral as well as to first- and second-order basal reflections from kaolinite. The large 0.334 nm peak in the pattern for Blanton clay is attributed to quartz because a corresponding 0.425 nm peak is present. A 0.483 nm peak, partially overlapping the third-order peak from the 1.4 nm mineral, indicates the presence of gibbsite in all of the clays. Neither feldspar nor illite was detected.

The XRD patterns obtained after the several chemical treatments of the Orangeburg clay (Figure 2) are typical of the corresponding patterns from all the SRS soil samples. Saturation with ethylene glycol did not cause a noticeable shift in the 1.4 nm peak of any of the clays, eliminating smectite as a possible constituent. Disappearance of the 1.4 nm and 0.71 nm peaks upon heating of the clays to 550ºC eliminated chlorite as a possible constituent. Potassium saturation caused no decrease in the basal spacing of the 1.4 nm mineral until after heating at 300ºC, whereupon the basal-reflection peak broadened and shifted to a slightly larger angle to show that the 1.4 nm mineral is HIV (Barnhisel and Bertsch, 1989).

The relatively large 0.71 nm peaks in the XRD patterns of the air-dried clays from the Orangeburg, Lakeland, and Fuquay samples indicate that kaolinite is preponderant in the clay fractions of these samples. Semi-quantitative determinations based on XRD peak-height ratios indicate that HIV makes up ~20% of the Orangeburg clay, 25% of the Fuquay and Lakeland clays, 35% of the Vaucluse clay, and 45% of the Blanton clay (Table 2), provided that estimates of 10% gibbsite in each clay fraction (15% for Orangeburg) are about right. The amounts of kaolinite and HIV found in the Fuquay and Orangeburg clays agree with amounts of these minerals reported by Karathanasis *et al*. (1983) and Kaplan *et al*. (1997), respectively, for clay fractions of samples from the B horizons of these soil series. Kaplan *et al*. (1997) reported 35% HIV in clay from the E horizon of Blanton soil, compared to the 45% found in the present study.

Cesium-137 uptake kinetics

About half of the added ^{137}Cs was taken up by the Fuquay sample in the first hour (Figure 3) but only ~18% was taken up in that time by the Vaucluse sample, which has a much smaller CEC than the Fuquay. The amount of added ^{133}Cs had little effect on the fraction of ^{137}Cs

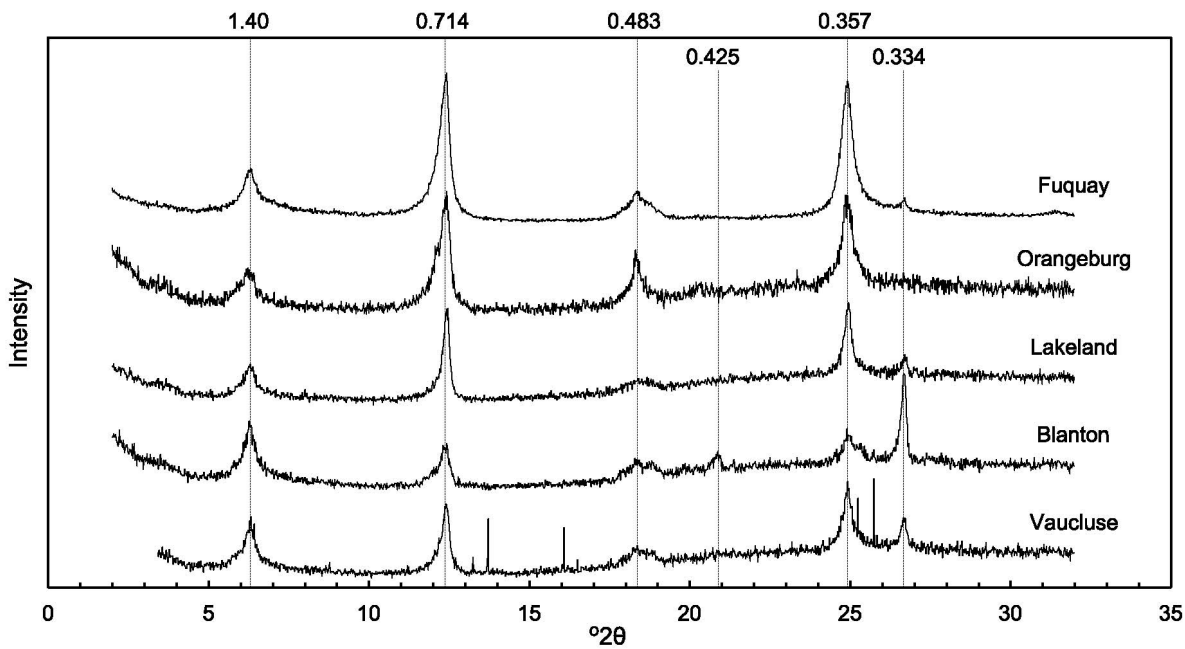

Figure 1. XRD patterns from oriented, air-dried portions of Na^+-saturated clay fractions of SRS soil samples. The vertical lines represent specific values of *d*/*n* from the Bragg equation, each labeled with its value in nanometers. Plotted values for the Fuquay clay are ¼ the measured intensities. The narrow spikes near 14º, 16º, and 26º2θ in the Vaucluse pattern are instrument artifacts probably caused by power surges.

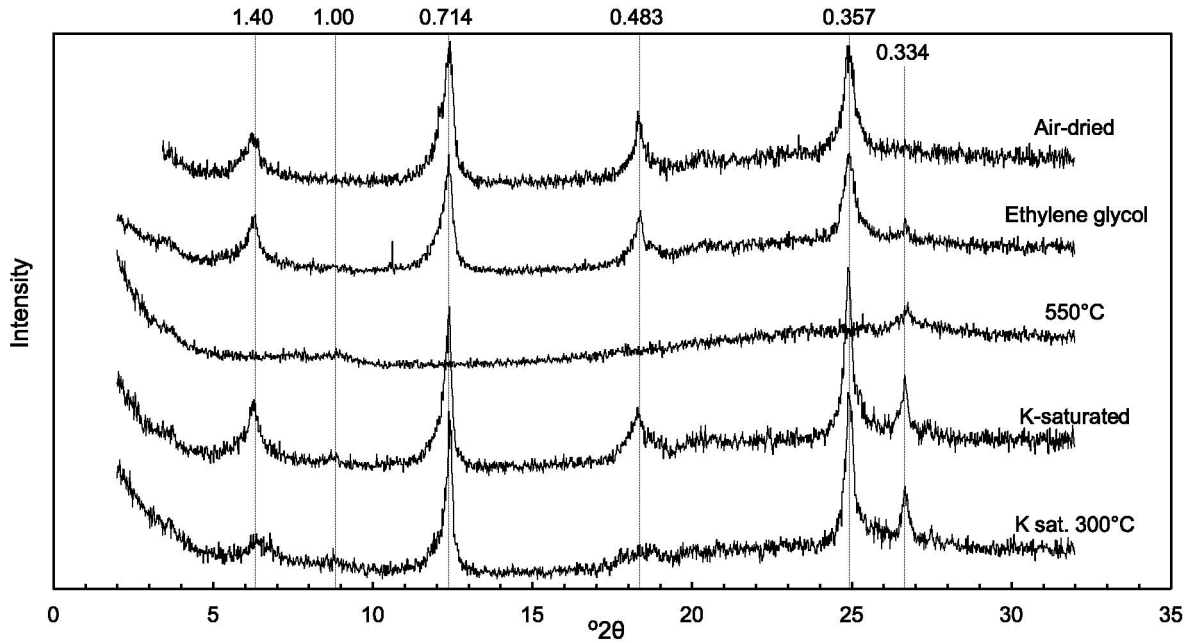

Figure 2. XRD patterns from oriented Orangeburg clay after various treatments. The vertical lines represent *d*/*n* with values in nanometers.

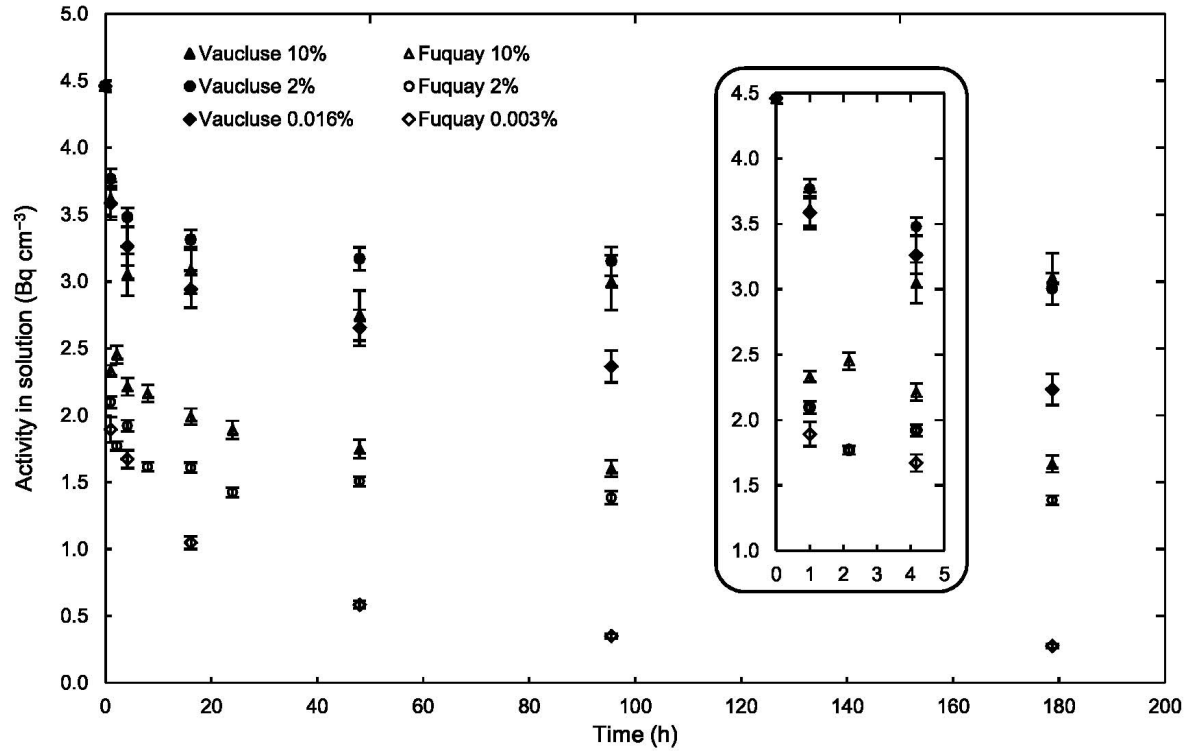

Figure 3. Time profile of ^{137}Cs uptake by 1 g portions of two SRS soils in 40 cm^3 0.005 mol dm^{-3} $NaNO_3$ solutions. Each solution initially contained ^{133}Cs in the equivalent ratio to the soil cation exchange sites shown in the legend as a percentage. The initial ^{137}Cs activity was the same, 4.45 Bq cm^{-3}, in all six experiments. Vertical bars represent the counting error as the standard deviation. The time scale is expanded in the inset portion to show more clearly the uptake during the first 4 h.

taken up in the first hour. Uptake continued much more slowly afterward. At the higher levels of added Cs, ^{137}Cs uptake was practically complete after 4 days. At the lowest level of added Cs (the very small amount of carrier in the ^{137}Cs solution), continued uptake of ^{137}Cs was evident throughout the 7-day period of the experiment.

Effects of silver thiourea on ^{137}Cs uptake

When added Cs was equivalent to ~0.03% of the cation exchange sites, the presence of AgTU reduced sorption of ^{137}Cs by only ~10% for the Fuquay, Orangeburg, and Lakeland samples and by 30% and 40% for the two other soil samples (Figure 4). At higher added Cs concentrations, the reduction of ^{137}Cs sorption in the presence of AgTU was much larger, except for the Blanton sample, averaging ~70% at the highest Cs level.

Sequential extractions

Less than 5% of the ^{133}Cs originally in the soils was removed in seven steps of sequential extraction of untreated portions of the Fuquay and Vaucluse soil samples (Table 3). Nearly all of the Cs remained with the solid phase until the final, total-dissolution step. In contrast, radioactive and stable Cs that had been sorbed by portions of these soil samples 2 months earlier were extracted readily, most appearing in the first two extraction steps. Much smaller, gradually decreasing, amounts were extracted in the subsequent extraction steps, until only ~3% of the recently sorbed Cs remained with the solids when they were dissolved in the final step.

Accessible original cesium

Isotope dilution of added radioactive Cs by the accessible natural Cs in soil, n_a, causes the specific activity, A/n, of Cs in the contacting solution to decrease, as shown by rearranging equation 4:

$$n_a = A_i(n_f/A_f - n_i/A_i) \quad (5)$$

where the right-hand expression must be positive if $n_a > 0$. In the work reported by Goto *et al*. (2008), the specific activity of Cs in solution decreased substantially over 4 days of contact of added Cs with portions of the Fuquay and Orangeburg samples (Table 4). The calculated amounts of accessible Cs for these samples are nearly 20% (on average) of the soil Cs. Little or no change in specific activity of Cs in solution for the other samples indicated little or no dilution of the added ^{137}Cs by soil Cs under acidic conditions. Under neutral conditions, the specific activity of Cs in solution decreased for all samples. The calculated amounts of accessible Cs range from near 10% of the soil Cs for the Blanton and Vaucluse soils to as much as 77% for the Fuquay soil.

DISCUSSION

Sorptive capacity of HIV in SRS soils

The XRD analyses showing HIV to be a substantial constituent of the clay fractions of the SRS soil samples are consistent with previous studies that show HIV to be widespread in highly weathered soils of the southeastern U.S. (Kirkland and Hajek, 1972; Harris *et al*., 1992a).

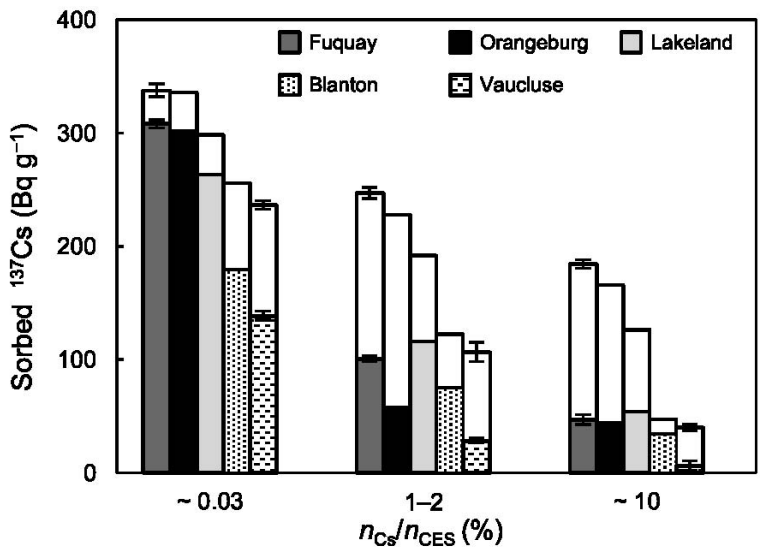

Figure 4. Cesium-137 sorbed by soil in the presence of AgTU (filled bars) compared to that sorbed in corresponding experiments without AgTU (larger values represented by the full height of each bar, filled plus open; from Goto *et al*., 2008) at three levels of ^{133}Cs, indicated as the equivalent ratio of ^{133}Cs (aqueous plus sorbed) to cation exchange sites, n_{Cs}/n_{CES}, in percent. Results for the Fuquay and Vaucluse samples are averages of results from duplicate portions. The ends of the 'error bars' represent the results for the individual portions.

Table 3. Stable Cs (^{133}Cs) and ^{137}Cs removed from untreated and Cs-treated soils by sequential extraction.

Step	Targeted form	Reagents	Time (h)	Fuquay sample			Vaucluse sample		
				Untreated	Treated		Untreated	Treated	
				^{133}Cs (mg kg^{-1})	^{133}Cs (mg kg^{-1})	^{137}Cs (Bq g^{-1})	^{133}Cs (mg kg^{-1})	^{133}Cs (mg kg^{-1})	^{137}Cs (Bq g^{-1})
1	Water soluble	Water	16	<0.01	36	56	<0.01	0.3	21
2	Exchangeable	0.5 M $Ca(NO_3)_2$	16	<0.01	56	87	<0.01	0.2	34
3	Acid soluble	0.44 M CH_3COOH 0.10 M $Ca(NO_3)_2$	8	0.1	9	19	<0.01	0.1	11
4	Manganese oxide occluded	0.01 M $NH_2OH.HCl$ 0.1 M HNO_3	0.5	<0.01	6	11	<0.01	<0.1	8
5	Organically bound	0.01 M $Na_4P_2O_7$	24	<0.01	4	8	<0.01	<0.1	8
6	Held by amorphous iron oxide	0.175 M $(NH_4)_2C_2O_4$ 0.1 M $H_2C_2O_4$	4	<0.01	3	5	<0.01	<0.01	1
7	Held by crystalline iron oxide	0.15 M $Na_3C_6H_5O_7$ 0.05 M $H_3C_6H_5O_7$	0.5 (50ºC)	<0.01	<1	2	<0.01	<0.01	1
8	Structurally bound	HF/HNO_3		4.3	8	4	0.8	0.9	2
			Sum	4.4	123	191	0.8	1.5	87
			Expected value	4.5*	174†	180‡	0.9*	2.7†	115‡

* Natural Cs from Goto *et al.* (2008)

† Sum of natural Cs determined by Goto *et al.* (2008) and sorbed added Cs determined in the present study from the difference between the amount added and the measured amount in solution at the end of the sorption period.

‡ Sorbed ^{137}Cs from Goto *et al.* (2008)

Table 4. Results of isotope dilution determination of accessible soil Cs.

Soil sample	$NaNO_3$ in solution (mol dm^{-3})	Solution mass (g)	Solution volume (cm^3)	^{133}Cs in solution* (nmol dm^{-3})	^{137}Cs in solution* (Bq cm^{-3})	– Accessible Cs† – (μmol kg^{-1})	(%)
Acidic mixtures							
Fuquay	0.001	1.030	40.1	5.7	0.227	7.4±0.9	22±3
		0.989	39.5	2.7	0.272	2.3±0.4	7±2
	0.005	0.981	40.2	10.4	0.342	9.6±1.1	28±4
		1.000	40.2	6.6	0.390	4.7±0.6	14±2
Orangeburg	0.001	1.010	40.0	4.5	0.291	4.2±0.6	18±3
	0.005	1.020	40.1	4.4	0.297	3.9±0.6	17±3
Lakeland	0.001	1.000	40.0	7.0	1.28	0.7±0.2	8±3
	0.005	1.000	40.1	4.7	1.51	−0.2±0.2	−2±2
Blanton	0.001	1.020	39.6	10.4	2.24	0.4±0.2	4±2
	0.005	1.000	40.1	9.5	2.39	0.2±0.2	1±2
Vaucluse	0.001	1.020	40.1	10.8	2.63	0.2±0.2	3±3
		1.010	40.0	11.2	2.91	0.1±0.2	2±3
	0.005	1.010	40.1	11.6	3.13	0.1±0.2	1±3
		1.010	40.2	10.6	3.25	−0.1±0.2	−1±3
Neutralized mixtures							
Fuquay	0.001	1.010	40.2	19.8	0.250	28±3	77±11
	0.005	1.010	40.2	27.5	0.576	16±2	45±7
Orangeburg	0.001	1.020	40.2	5.1	0.136	12.2±1.4	51±8
		1.050	40.1	4.9	0.169	9.0±1.1	37±6
	0.005	1.020	40.2	9.3	0.317	9.3±1.1	39±6
		1.040	40.2	10.7	0.311	10.9±1.3	45±7
Lakeland	0.001	1.020	40.1	3.4	0.314	2.7±0.4	31±6
	0.005	1.050	40.2	4.2	0.670	1.0±0.3	11±3
Blanton	0.001	1.030	40.0	3.4	0.533	1.0±0.3	9±2
	0.005	1.010	40.2	5.9	0.988	0.9±0.3	8±2
Vaucluse	0.001	1.020	39.9	5.4	0.831	1.1±0.3	15±4
		1.020	40.0	6.4	1.09	0.9±0.3	12±4
	0.005	1.000	40.2	8.9	1.77	0.6±0.2	8±3
		1.030	40.2	6.6	1.68	0.2±0.2	2±3

* From Goto *et al*. (2008); ^{133}Cs concentration and ^{137}Cs activity concentration are as determined at the end of the experiment. The measurement standard deviation was 10% for ^{133}Cs and 2% for ^{137}Cs. The activity of added ^{137}Cs was 351 Bq for acidic mixtures and 364 Bq for neutralized mixtures and the amounts of added ^{133}Cs were 1.28 nmol and 1.32 nmol, respectively. [Table footnotes of Goto *et al.* (2008) gave the unit for added ^{137}Cs as kBq by mistake, and the amounts of added ^{133}Cs were slightly more than the nominal 1.24 nmol listed in those tables.]

† Amounts of accessible Cs, expressed here as specific amounts in dry soil, were calculated as described in the 'Materials and Methods' section. In the last column, the calculated amount of accessible Cs is expressed as a percentage of the naturally occurring soil Cs. The error values are based on the measurement standard deviations for ^{133}Cs and ^{137}Cs.

The shift to a slightly larger angle and broadening of the HIV basal-reflection peak upon heating K-saturated clay at 300ºC suggest substantial filling of the HIV interlayer with hydroxy-Al polymers (Barnhisel and Bertsch, 1989) and are similar to behavior that Harris *et al*. (1992a) described as typical of HIV in Florida soils. The relatively large amount of HIV in the clay fraction of the shallowest sample (Blanton) is consistent with numerous observations that HIV is particularly abundant in near-surface horizons (Harris *et al*., 1992a). If the CEC of the HIV is ~50 cmol kg^{-1}, the mean of values reported by Kirkland and Hajek (1972) for HIV in Alabama, there is sufficient HIV in the clay fraction (Table 2) to account for most of the CEC (Table 1) of each SRS soil sample.

Large-ion alkali metals in HIV grains and mica

Amounts of the large-ion alkali metals, Cs, Rb, and K, found in the five soil samples are correlated with the mass fraction of clay-sized HIV (Figure 5), the latter calculated as the product of the mass fractions of HIV in the clay (Table 2) and of clay in the soil (the average of values in Table 1). The K content of the clay fraction, as a mass fraction relative to the mass of dry soil ('Clay K'

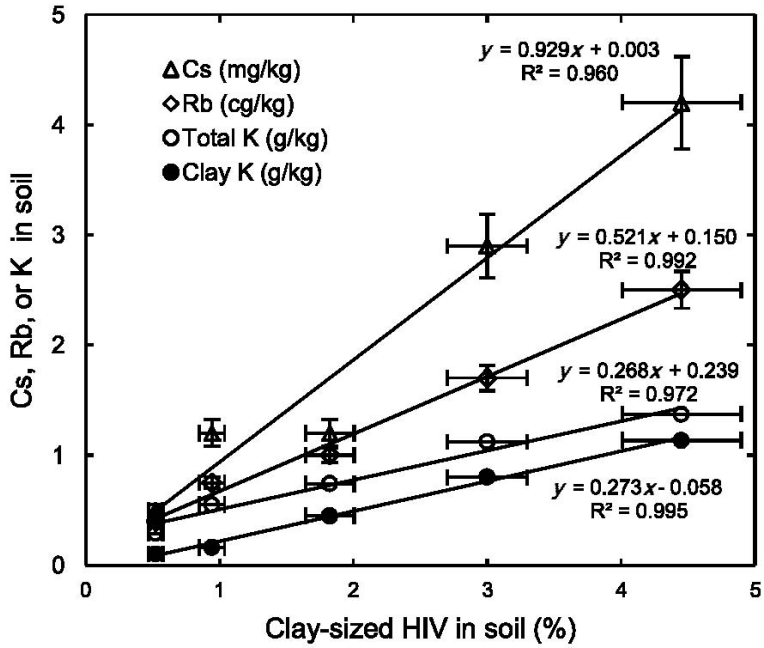

Figure 5. Correlations of mass fractions of Cs and Rb (from Wampler *et al.*, 2012) and K (averages of values in Tables 1 and 2) in SRS soil samples with the mass fraction of clay-sized HIV. The legend gives the units for element mass fractions. The 'Clay K' values are of the mass of K in the clay fraction relative to the mass of dry soil. Relative error in HIV content is estimated as ±10%. Error values for Cs and Rb content are from Wampler *et al*. (2012). Errors in K values are smaller than the symbols for the values.

in Figure 5), is closely proportional to the mass fraction of clay-sized HIV in the soil, indicating that the K in the soil clay is in HIV grains. The 'total K' includes any K in micaceous grains larger than clay (HIV or mica), so the values are greater than those for 'Clay K,' an effect greatest for the Blanton sample, which has a high ratio of silt to clay. For three of the five samples, Cs content is nearly proportional to the mass fraction of clay-sized HIV in the soil. The Blanton Cs value is elevated, probably because of Cs in silt-sized HIV grains. The distinctly low Cs value for the Lakeland sample may be due to a shorter time for Cs fixation in the relatively young Lakeland soil (an Entisol) than in the other soils studied (Ultisols). The relationship of Rb content to clay-sized HIV is consistent with the inference of Wampler *et al*. (2012) that Rb occurs in the HIV grains as a native constituent of mica (as does K) and also as a result of its selective sorption in interlayer wedge zones (as does Cs).

Cesium-137 uptake kinetics

The kinetics experiment was intended to find the time necessary for added Cs to reach exchange equilibrium with SRS soils, but the results have value beyond that original purpose. The continued, slow uptake of ^{137}Cs after the first day at the lowest level of added ^{133}Cs is reminiscent of uptake of ^{137}Cs by Fithian illite from solutions having similar initial ^{133}Cs concentration (~10^{-8} mol dm^{-3}; figure 1 of Comans *et al*., 1991). After relatively large ^{137}Cs uptake during the first few hours, the Fithian illite continued to sorb ^{137}Cs slowly during the next twelve days. The early ($\leqslant$4 h) ^{137}Cs uptake by illite was about twice as great as in a parallel experiment (Comans *et al*., 1991, figure 1) in which the initial ^{133}Cs concentration was 20 times greater, which indicates that Cs ions had prompt access to sites on illite that are highly Cs-selective but low in abundance, consistent with the view that these sites are at the particle edges.

In contrast, wide variation of initial ^{133}Cs concentration had relatively little effect on ^{137}Cs uptake by the two SRS soils during the first 4 h of contact, which indicates that sites highly selective for Cs but low in abundance played only a minor role in the short-term uptake. The effects of the different amounts of ^{133}Cs added became apparent over longer times. At the lowest ^{133}Cs level, sorption increased gradually over the entire week of the experiment until amounts of sorbed ^{137}Cs were distinctly greater than in corresponding experiments with more added ^{133}Cs. These results are evidence that SRS soil has low concentrations of highly Cs-selective sites and that added Cs cannot reach most such sites quickly.

These observations are consistent with the inference that uptake of Cs by SRS soils is primarily by HIV grains that have abundant sites on planar surfaces and relatively few highly Cs-selective interlayer wedge sites (Goto *et al*., 2008). Furthermore, the results support the structural model of Rich and Black (1964) in which the interlayer wedge zones are well within interlayers

partially filled by hydroxy-Al polymers, which would cause the pathways for interlayer diffusion to be narrow and tortuous (Harris *et al*., 1992b).

Blocking cesium uptake with silver thiourea

At the lowest level of added ^{133}Cs, most sorbed Cs should have reached highly Cs-selective sites after 4 days. That such sites are not blocked by AgTU effectively explains the small influence of AgTU on ^{137}Cs sorption at that level. The results do not allow quantitative calculation of the fraction of sites blocked by AgTU, because the acidity of thiourea caused enhanced competition by H ions for exchange sites that would take up Cs^+.

At the higher ^{133}Cs concentrations, in the absence of AgTU most of the Cs sorption should have been on planar surfaces of HIV. The observed large reductions in ^{137}Cs uptake in the presence of AgTU at these ^{133}Cs concentrations, except for the Blanton sample, indicate that AgTU blocked large fractions of the planar-surface sites that otherwise would have held Cs^+. The anomalous response of the Blanton sample to the presence of AgTU may have arisen from the relatively large size of the HIV grains in that E-horizon sample. This issue cannot be resolved with the data available now, but it points to a need for study of HIV grains from different size fractions.

Sequential extraction

The sequential extraction results are consistent with the expectation that the uptake of recently sorbed ^{137}Cs and ^{133}Cs was predominantly by ion exchange. The generally decreasing amounts of ^{133}Cs and ^{137}Cs removed in steps 3 to 7 can be attributed to continued, progressively more complete, replacement of sorbed Cs^+ by Na^+ rather than to responses by the specific solid phases targeted in these steps. The relative amounts of recently sorbed ^{133}Cs and ^{137}Cs extracted in each step are broadly consistent with one another, even though the totals indicate losses that may be due to loss of clay during repeated phase separations by centrifugation and decantation (Goto, 2001).

The results for the untreated soil portions confirm earlier work by Findley (1998) and show that very little of the Cs originally in the soils is at ordinary ion-exchange sites or is bound in organic matter or Fe and Mn oxides. The much greater extractability of the recently added Cs in comparison to the natural Cs is consistent with the observation by Clark *et al*. (1996) that ^{137}Cs recently introduced to the environment at the SRS is much more labile than the ^{133}Cs originally present.

Accessible original cesium

Experiments with carrier-free ^{137}Cs can mislead if the amount of accessible natural Cs in soil is not known (Grütter *et al*., 1990). Very little of the natural Cs in SRS soils is inaccessible because it remains in residual primary minerals (Wampler *et al*., 2012). The rest of the Cs in soil has participated in mineral–water reactions as pre-existing materials have been converted into the soils existing today. In concept, one might divide such Cs into: (1) Cs that has become 'fixed' in some way and is no longer accessible for isotope dilution and (2) Cs that is accessible for isotope dilution as exchangeable cations or in a soluble form. Slow fixation of small amounts of radiocesium by illite and illitic sediments, over periods of weeks to months, has been reported by a number of investigators (Comans and Hockley, 1992). The relatively small amounts of natural Cs found in the present study to be accessible for isotope dilution under acidic conditions, 20% or less of the soil Cs, indicate that most of the natural Cs in the upland SRS soils is effectively fixed. The ~20% of soil Cs found to be accessible in the Fuquay and Orangeburg samples was probably in cation exchange sites highly selective for Cs, because only a few percent of the soil Cs was removed by sequential extractions.

After neutralization of the soil suspensions, substantially more of the soil Cs was found to be accessible in all five of the samples. Under the assumptions used in calculation, these greater amounts of accessible Cs would require that neutralization converted some previously inaccessible Cs into accessible Cs. An alternative view, based on the common observation that E values increase with increasing contact time owing to kinetically limited dilution of an added radioisotope by the natural element in some soil compartments (Diesing *et al*., 2008), is that the isotope dilution process was not complete in either case but was more rapid and thus more extensive in the neutralized soils. If most of the natural Cs in the SRS soils is effectively fixed in the narrower parts of interlayer wedge zones, where steric hindrance to cation exchange is to be expected (Wampler *et al*., 2012), the effect of neutralization on the conformation of the interlayer wedges zones may have influenced the rate of isotope dilution. Interlayer hydroxy-Al polymeric cations prevent expansion of HIV (Meunier, 2007), but neutralization of these polymeric ions would have eliminated their electrostatic attraction to the clay layers and may thus have allowed some interlayer expansion. Such expansion may have widened interlayer wedge zones enough that the rate of isotope dilution of added Cs by natural Cs that was in the narrower parts of the wedge zones could increase substantially.

Synthesis

The findings reported above point clearly to HIV grains as the hosts of the naturally occurring Cs, Rb, and K in the upland soils of the SRS. The XRD analyses show that HIV is a major constituent of the soil clay, second only to kaolinite. The recalcitrance of nearly all of the soil Cs to the sequential extractions shows that

most such Cs is either fixed or is in cation exchange sites that are extremely selective for Cs ions relative to Na and H ions. In contrast to HIV, kaolinite has little CEC (Lim *et al*., 1980) and no highly Cs-selective sites (Nakao *et al*., 2008), and the same is true of quartz and gibbsite. Elimination of soil materials other than HIV grains as hosts is consistent with the observation that the Cs, Rb, and K contents of these soils are closely related to their HIV content.

By similar reasoning, the experiments in the present study on Cs sorption by SRS soil samples were effectively tests of Cs sorption by the HIV grains. The distinct differences in sorption kinetics and in the effects of AgTU at different levels of added ^{133}Cs support the hypothesis of Goto *et al*. (2008) that HIV grains have different kinds of sites for Cs sorption. By this hypothesis, when only traces of ^{133}Cs were present, Cs sorption occurred mostly on the relatively few sites highly selective for Cs. That AgTU did not block these sites and that added Cs did not promptly reach most of these sites supports the idea that they are stereoselective sites mostly well inside HIV grains (Rich and Black, 1964). In contrast to its behavior at trace levels, Cs in larger concentrations was sorbed mostly on abundant planar-surface sites that are not especially selective for Cs, accounting for the ready extraction of most of the recently sorbed Cs and for the extensive reduction of Cs sorption in the presence of AgTU. The distinction between these two site types allows prediction that ^{137}Cs retention from aqueous discharges onto HIV-containing soil will be most effective when stable cesium concentration in solution is lowest.

The evidence presented by Goto *et al*. (2008) and in this study for the presence of highly Cs-selective sites in HIV grains is contrary to an inference by Maes *et al*. (1998) and Nakao *et al*. (2009) that the hydroxy-Al polymers in such particles block radiocesium access to the Cs-specific sites and to a finding by Dion *et al*. (2005) of very low Cs selectivity for HIV-bearing sandy sediment from the SRS. More-detailed study of soil clays in which HIV grains are the sole host for sorbed Cs is needed to resolve the conflict.

The much greater chemical extractability of recently added radiocesium than natural, stable Cs emphasizes important differences between the interaction of SRS soils with Cs in large amounts over short times and their interaction with trace amounts of Cs over long times. That the natural Cs does not occupy ordinary cation exchange sites is shown by its observed resistance to chemical extraction (Findley, 1998; this study). Most of the soil Cs did not isotopically dilute the added ^{137}Cs under acidic conditions, indicating effective fixation of most of the soil Cs in sites where Cs atoms either were inaccessible or were accessible only very slowly. These observations support the mechanistic interpretation that most of the Cs in these soils has become effectively fixed in the narrower parts of interlayer wedge zones where steric hindrance to exchange of large cations is great. The predicted gradual shift of sorbed ^{137}Cs inward within such zones may be a key factor in the soil's ability to hold radiocesium.

CONCLUSIONS

Findings in the experiments described and information from the cited references were synthesized to conclude the following:

In the upland soils that cover most of the SRS, HIV is a major constituent of the clay, second only to kaolinite, and is the major ion-exchange medium. The HIV grains host the naturally occurring Cs, Rb, and K in these soils.

The HIV grains hold Cs at three types of sites: (1) numerous ion-exchange sites that do not discriminate strongly among ions in favor of Cs; (2) a small fraction of ion-exchange sites that hold Cs strongly during exchange with other ions in solution; and (3) sites that hold Cs and do not exchange it readily with ions in solution, be they Cs or other ions.

A physical mechanistic model is proposed that associates sites of the first type with planar surfaces and sites of the second and third types with interlayer wedge zones. Sites of the third type are deep within interlayer wedge zones where Cs ions are effectively inaccessible for cation exchange. The first and second site types are analogous to the regular exchange sites and frayed-edge sites, respectively, of illite. Most of the natural Cs in SRS soils is effectively fixed in sites of the third type.

ACKNOWLEDGMENTS

This research was supported in part by ERDA Project GA 00-64 of the Westinghouse Savannah River Company. D. Kaplan of the Savannah River National Laboratory provided valuable support and advice. Helpful comments by P. Ryan and other reviewers, by the editors, and by A. Meunier and others who reviewed earlier manuscripts about this work are gratefully acknowledged.

REFERENCES

Barnhisel, R.I. and Bertsch, P.M. (1989) Chlorites and hydroxy-interlayered vermiculite and smectite. Pp. 729–788 in: *Minerals in Soil Environments*, 2nd edition (J.B. Dixon and S.B. Weed, editors). Soil Science Society of America, Madison, Wisconsin, USA.

Clark, S.B., Johnson, W.H., Malek, M.A., Serkiz, S.M., and Hinton, T.G. (1996) A comparison of sequential extraction techniques to estimate geochemical controls on the mobility of fission product, actinide, and heavy metal contaminants in soils. *Radiochimica Acta*, **74**, 173–179.

Comans, R.N.J. and Hockley, D.E. (1992) Kinetics of cesium sorption on illite. *Geochimica et Cosmochimica Acta*, **56**, 1157–1164.

Comans, R.N.J., Haller, M., and De Preter, P. (1991) Sorption of cesium on illite: Non-equilibrium behaviour and reversibility. *Geochimica et Cosmochimica Acta*, **55**, 433–440.

Cremers, A., Elsen, A., De Preter. P., and Maes, A. (1988) Quantitative analysis of radiocaesium retention in soils.

Nature, **335**, 247–249.

Diesing, W.E., Sinaj, S., Sarret, G., Manceau, A., Flura, T., Demaria, P., Siegenthaler, A., Sappin-Didier, V., and Frossard, E. (2008) Zinc speciation and isotopic exchangeability in soils polluted with heavy metals. *European Journal of Soil Science*, **59**, 716–729.

Dion, H.M., Romanek, C.S., Hinton, T.G., and Bertsch, P.M. (2005) Cesium-137 in floodplain sediments of the Lower Three Runs Creek on the DOE Savannah River Site. *Journal of Radioanalytical and Nuclear Chemistry*, **264**, 481–488.

Elprince, A.M., Rich, C.I., and Martens, D.C. (1977) Effect of temperature and hydroxy aluminum interlayers on the adsorption of trace radioactive cesium by sediments near water-cooled nuclear reactors. *Water Resources Research*, **13**, 375–380.

Findley, M. (1998) Characterizing the environmental availability of trace metals in soils at the Savannah River Site. M.S. thesis, Clemson University, Clemson, South Carolina, USA.

Goto, M. (2001) Development of a quantitative model for binding cesium to SRS soils. M.S. thesis, Georgia Institute of Technology, Atlanta, Georgia, USA.

Goto, M., Rosson, R., Wampler, J.M., Elliott, W.C., Serkiz, S., and Kahn, B. (2008) Freundlich and dual Langmuir isotherm models for predicting ^{137}Cs binding on Savannah River Site soils. *Health Physics*, **94**, 18–32.

Grütter, A., von Gunten, H.R., Kohler, M., and Rössler, E. (1990) Sorption, desorption and exchange of cesium on glaciofluvial deposits. *Radiochimica Acta*, **50**, 177–184.

Harris, W.G., Morrone, A.A., and Coleman, S.E. (1992a) Occluded mica in hydroxy-interlayered vermiculite grains from a highly-weathered soil. *Clays and Clay Minerals*, **40**, 32–39.

Harris, W.G., Hollien, K.A., Bates, S.R., and Acree, W.A. (1992b) Dehydration of hydroxy-interlayered vermiculite as a function of time and temperature. *Clays and Clay Minerals*, **40**, 335–340.

Jackson, M.L. (1969) *Soil Chemical Analysis Advanced Course* (2nd edition). University of Wisconsin, Madison, USA.

Kaplan, D.I., Sumner, M.E., Bertsch, P.M., and Adriano, D.C. (1996) Chemical conditions conducive to the release of mobile colloids from ultisol profiles. *Soil Science Society of America Journal*, **60**, 269–274.

Kaplan, D.I., Bertsch, P.M., and Adriano, D.C. (1997) Mineralogical and physicochemical differences between mobile and nonmobile colloidal phases in reconstructed pedons. *Soil Science Society of America Journal*, **61**, 641–649.

Karathanasis, A.D. and Hajek, B.F. (1982) Revised methods for rapid quantitative determination of minerals in soil clays. *Soil Science Society of America Journal*, **46**, 419–425.

Karathanasis, A.D., Adams, F., and Hajek, B.F. (1983) Stability relationships in kaolinite, gibbsite, and Al-hydroxy interlayered vermiculite soil systems. *Soil Science Society of America Journal*, **47**, 1247–1251.

Kirkland, D.L. and Hajek, B.F. (1972) Formula derivation of Al-interlayered vermiculite in selected soil clays. *Soil Science*, **114**, 317–322.

Kunze, G.W. and Dixon, J.B. (1986) Pretreatment for mineralogical analysis. Pp. 91–99 in: *Methods of Soil Analysis* (2nd edition), *Part 1 – Physical and Mineralogical Methods*. American Society of Agronomy, Madison, Wisconsin, USA.

Lim, C.H., Jackson, M.L., Koons, R.D., and Helmke, P.A. (1980) Kaolins: Sources of differences in cation-exchange capacities and cesium retention. *Clays and Clay Minerals*, **28**, 223–229.

Looney, B.B., Eddy, C.A., Ramsdeen, M., Pickett, J., Rogers, V., Scott, M.T., and Shirley, P.A. (1990) Geochemical and physical properties of soils and shallow sediments at the Savannah River Site. WSRC-RP-90-1031, Westinghouse Savannah River Company. Aiken, South Carolina, USA.

Maes, E., Delvaux, B., and Thiry, Y. (1998) Fixation of radiocaesium in an acid brown forest soil. *European Journal of Soil Science*, **49**, 133–140.

Meunier, A. (2007) Soil hydroxy-interlayered minerals: A reinterpretation of their crystallochemical properties. *Clays and Clay Minerals*, **55**, 380–388.

Miller, W.P., Martens, D.C., and Zelazny, L.W. (1986) Effect of sequence in extraction of trace metal from soils. *Soil Science Society of America Journal*, **50**, 598–601.

Nakao, A., Thiry, Y., Funakawa, S., and Kosaki, T. (2008) Characterization of the frayed edge site of micaceous minerals in soil clays influenced by different pedogenetic conditions in Japan and northern Thailand. *Soil Science and Plant Nutrition*, **54**, 479–489.

Nakao, A., Funakawa, S., and Kosaki, T. (2009) Hydroxy-Al polymers block the frayed edge sites of illitic minerals in acid soils: studies in southwestern Japan at various weathering stages. *European Journal of Soil Science*, **60**, 127–138.

Naumann, T.E., Elliott, W.C., and Wampler, J.M. (2012) K-Ar age constraints on the origin of micaceous minerals in Savannah River Site soils, South Carolina, USA. *Clays and Clay Minerals*, **60**, 496–506.

NCRP (2006) Cesium-137 in the environment: radioecology and approaches to assessment and management. Bethesda, MD, National Council on Radiation Protection and Measurements; NCRP Report 154.

Prout, W.E. (1958) Adsorption of radioactive waste by Savannah River Plant soil. *Soil Science*, **86**, 13–17.

Rich, C.I. and Black, W.R. (1964) Potassium exchange as affected by cation size, pH, and mineral structure. *Soil Science*, **97**, 384–390.

Rogers, V.A. (1990) Soil survey of Savannah River Plant area, parts of Aiken, Barnwell, and Allendale counties, South Carolina. USDA Soil Conservation Service, Washington, DC.

Ruhe, R.V. and Matney, E.A. (1980) Clay mineralogy of selected sediments and soils at the Savannah River Plant, Aiken, South Carolina. DP-MS-80-119, Indiana University, Bloomington, Indiana, USA.

Segall, M.P., Siron, D.L., and Colquhoun, D.J. (2000) Depositional and diagenetic signatures of Late Eocene–Oligocene sediments, South Carolina. *Sedimentary Geology*, **134**, 27–47.

Smolders, E., Brans, K, Földi, A., and Merckx, R. (1999) Cadmium fixation in soils measured by isotopic dilution. *Soil Science Society of America Journal*, **63**, 78–85.

Wampler, J.M., Krogstad, E.J., Elliott, W.C., Kahn, B., and Kaplan, D.I. (2012) Long-term selective retention of natural Cs and Rb by highly weathered coastal plain soils. *Environmental Science & Technology*, **46**, 3837–3843.

(*Received 30 June 2013; revised 6 June 2014; Ms. 784; AE: J.W. Stucki*)

Clays and Clay Minerals, Vol. 62, No. 3, 174–187, 2014.

THE PORE STRUCTURE OF COMPACTED AND PARTLY SATURATED MX-80 BENTONITE AT DIFFERENT DRY DENSITIES

LUKAS M. KELLER[1,*], ALI SEIPHOORI[2], PHILIPPE GASSER[3], FALK LUCAS[3], LORENZ HOLZER[1], AND ALESSIO FERRARI[2]

[1] Zürich University of Applied Sciences, Winterthur, Switzerland
[2] Ecole Polytechnique Fédérale de Lausanne (EPFL), School of Architecture, Civil and Environmental Engineering (ENAC), Laboratory for Soil Mechanics (LMS), Switzerland
[3] Swiss Federal Institute of Technology, Centre for Imaging Science and Technology, Zürich, Switzerland

Abstract—Compacted MX-80 bentonite is a potential backfill material in radioactive-waste repositories. Pore space in MX-80 has been the subject of considerable debate. 3D reconstructions of the pore space based on tomographic methods could provide new insights into the nature of the pore space of compacted bentonites. To date, few such reconstructions have been done because of problems with the preparation of bentonite samples for electron microscopy. The nanoscale intergranular pore space was investigated here by cryo-Focused Ion Beam nanotomography (FIB-nt) applied to previously high-pressure frozen MX-80 bentonite samples. This approach allowed a tomographic investigation of the *in situ* microstructure related to different dry densities (1.24, 1.46, and 1.67 g/cm^3). The FIB-nt technique is able to resolve intergranular pores with radii >10 nm. With increasing dry density (1.24−1.67 g/cm^3) the intergranular porosity (>10 nm) decreased from ~5 vol.% to 0.1 vol.%. At dry densities of 1.24 and 1.46 g/cm^3, intergranular pores were filled with clay aggregates, which formed a mesh-like structure, similar to the honeycomb structure observed in diagenetic smectite. Unlike 'typical' clay gels, the cores of the honeycomb structure were not filled with pure water, but instead were filled with a less dense material which presumably consists of very fine clay similar to a colloid. In the low-density sample this honeycomb-structured material partly filled the intergranular pore space but some open pores were also present. In the 1.46 g/cm^3 sample, the material filled the intergranular pores almost completely. At the highest densities investigated (1.67 g/cm^3), the honeycomb-structured material was not present, probably because of the lack of intergranular pores which suppressed the formation of the honeycomb framework or skeleton consisting of clay aggregates.

Key Words—Clay Gels, Cryo-sample Preparation, MX-80 Bentonite, Nanotomography.

INTRODUCTION

The engineering concepts for radioactive-waste repositories include a barrier system which consists of a sealing material that surrounds the waste canisters and fills (*i.e.* backfill) the cavities between the canisters and the borehole in the host rock. Bentonite is considered a potential backfill material (*e.g.* Bucher and Müller-Vonmoos, 1989; Gens, 2010). An advantage of bentonite is its large swelling capacity; under confined conditions, the compaction results in consolidation into a dense material. A final assessment of its suitability as a backfill material requires an understanding of the microstructure response to compaction. In particular, understanding reduction of porosity and pore connectivity due to compaction and associated increase in density is critical when evaluating the sealing property of the material (*e.g.* Saiyouri *et al.*, 2000; Delage and Cui, 2007; Monroy *et al.*, 2010). To date, insight into the chemical and physical properties of bentonite has been achieved by analytical and experimental work (*e.g.* Herbert *et al.*, 2004; Lloret and Villar, 2007). Detailed knowledge of the microstructural properties corresponding to variable bulk physical properties is still lacking. In the context of its application as a backfill material and corresponding sealing behavior, microstructural investigations of the nanoscale pore space in bentonites using high-resolution imaging techniques are scarce, the work of Pusch (2001) and Holzer *et al.* (2010) being exceptions. At larger length scales, other studies used X-ray computed microtomography to study the microstructure of bentonites (*e.g.* Tomioka *et al.*, 2010).

Bentonite is also employed in other engineering applications such as drilling fluids where it is used in the form of suspensions where the flow behavior is of major concern (*e.g.* Luckham and Rossi, 1999). Bentonite suspensions have much lower concentrations of clay (solid loading) in comparison to bentonite used as a sealing material. Regardless of the clay concentration, the main challenge to the study of bentonite microstructures is sample preparation. For electron-beam imaging the samples must be stable under high vacuum. Drying may induce significant artifacts associated with shrinking, however. In addition, the softness of the material also posed a challenge as bentonite and its

* E-mail address of corresponding author:
kelu@zhaw.ch
DOI: 10.1346/CCMN.2014.0620302

microstructure are prone to undesirable mechanical modifications that can occur during sample preparation. Hence, for quantitative microscopic investigations of compacted and hydrated bentonite, the development of methods that enable the stabilization and preservation of the original pore structure is crucial. To overcome these problems, several methods have been applied to prepare bentonite samples for electron-beam imaging. The methodological developments in bentonite-sample preparation over the last five decades along with the difficulties encountered were summarized by Bhuiyan (2013). Regarding bentonite suspensions, the rearrangement of clay particles during sample preparation was of major concern. Cryofixation techniques in combination with cryo-SEM/TEM prevented rearrangement of particles and over the years these methods began to offer promise in terms of the investigation of the microstructures of bentonite suspensions (Vali and Hesse, 1992; Gu and Doner, 1993; Bhuiyan, 2013). The most critical aspect of these cryofixation techniques was the cooling rate. If the cooling rate is too slow, the formation of ice crystals and phase separation can affect the original bentonite microstructure (Vali and Hesse, 1992). To achieve the necessary cooling rates that allow vitrification of the pore water, the sample thickness must be minimized. The present study used a state-of-the-art, high-pressure freezing instrument that was able to freeze samples with a thickness of 200 μm within milliseconds so that they were completely vitrified. This method was first used by Velbel and Barker (2008) and Holzer *et al.* (2010), among others, who applied this method in combination with cryo-SEM in the investigation of wet geological clayey samples. For conventional high-pressure freezing, the samples must be transferred into small sample holders. The degree of compaction could not be controlled during the transfer into the sample holder.

For the present study a new procedure for high-pressure freezing of compacted bentonite samples was developed. In order to study pore-space evolution as function of dry density, re-hydrated bentonite samples with well defined properties (*e.g.* dry densities, water content, total porosity) were produced directly in the sample holders of the high-pressure freezing instrument. This approach required the fabrication of light bentonite samples, so that the volume of compacted material was equivalent to the volume of the small sample holders. This procedure required an exceptionally precise balance. After weighing the correct amount of material to match the target density, the bentonite material was placed directly into the sample holder of the high-pressure freezing system and compacted there. Then the samples were analyzed in a frozen state using cryo-FIB-nt. This approach avoided the artifacts which emerge if the samples are dried prior to microscopic investigation. In addition, the approach also avoided effects arising from mechanical preparation, ice-crystal formation, and phase separation due to conventional freezing. Thus, everything that is technically feasible was done to preserve the original microstructure from partially hydrated bentonite samples with different bulk densities.

A major constituent of bentonites is montmorillonite, which is a member of the smectite family. Diffusive solute transport in such a system is complicated by the fact that mineral layer surfaces are negatively charged, which is compensated by exchangeable cations located between the mineral layers. Diffusion models often assume that transport of chemical species occurs along two different types of pathways, one of which is the charged surfaces of mineral layers (*i.e.* interlayer region), while the other corresponds to larger water-filled pores where transport occurs largely unaffected by surface charging (*e.g.* Appelo, 2013). The actual contribution of the two pathways to solute transport is subject to discussion (*e.g.* Glaus *et al.*, 2013). Experimental data on cation diffusion were explained by simultaneous transport along the two different pathways (*e.g.* Bourg *et al.*, 2007). In contrast, tracer diffusion experiments suggested that surface diffusion dominates cation diffusion (Glaus *et al.*, 2007). Anion diffusion is often modeled using the assumption that these species are strongly repelled from the clay-mineral surfaces and thus the predominant diffusion path for anionic species are larger, water-filled pores (Pusch *et al.*, 1990). On the basis of experimental diffusion data, this assumption allowed the determination of diffusion-accessible porosity, which was interpreted as the water-filled porosity or intergranular porosity. The calculated diffusion-accessible porosities are inconsistent, however, and depend on the diffusion models used (Tournassat and Appelo, 2011), which led to the suggestion that porosities calculated from diffusion data lack physical meaning. FIB-nt is able to resolve intergranular pores with radii >~10 nm, but is unable to resolve the nanopores between mineral layers of smectite minerals. From a microstructural point of view, the approach used was a first attempt to shed light on the nature of the pore space in dense compacted bentonites. The microstructural data acquired correspond to well defined bentonite samples and conclusions were reached on the nature of the disputed diffusion pathways (*i.e.* intergranular pores).

SAMPLE PREPARATION

MX-80 bentonite was first sieved to a grain size of <90 μm (powder form) in order to achieve maximum homogeneity. In order to saturate the dry material, the powder was vapor-phase hydrated. The powder was placed in a humid chamber that was set to 100% relative humidity. After ~4–5 weeks the bentonite powder reached the target water content. Liquid-water saturation was found to be unsuitable due to aggregation of the powder which resulted in inhomogeneous distribution of

Table 1. Properties of the samples prepared for the FIB analysis.

Sample name	Holder		Compacted powder		Target values			Final sample properties			
	Weight of top cap (g)	Weight of bottom cap (g)	Water content, w* (-)	Ψ** (MPa)	ρ_d, target (g/cm^3)	Target dry mass (g)	Target wet mass (g)	Mass of compacted wet soil + holders (g)	Mass of compacted wet soil (g)	ρ_d (g/cm^3) (dry)	ρ_{bulk} (g/cm^3) (wet)	Porosity, n(-)	Degree of saturation, S_r(-)
7,W.1.3	0.0226	0.0264	0.313	3.85	1.3	0.0051	0.0067	0.0553	0.0063	1.23	1.62	0.55	0.70
3,W.1.5	0.0226	0.0258	0.226	13.86	1.5	0.0059	0.0072	0.0554	0.0070	1.46	1.80	0.46	0.71
4,W,1.7	0.0225	0.0254	0.226	13.86	1.7	0.0067	0.0082	0.0559	0.0080	1.67	2.05	0.39	0.97

* Target water content was achieved by hydration in the vapor phase.
** Values measured by a dewpoint potentiometer system (WP4C device, Decagon, 2002).

the water within the bentonite samples. Homogenization of water was better achieved in the vapor form. Water contents of 22.6 wt.% and 31.3 wt.% were obtained in this way, corresponding to 13.86 and 3.85 MPa of total suctions, respectively (Table 1). Total suction was measured using a dewpoint potentiometer system (WP4C device; Decagon, 2002).

By considering the water content of the hydrated powder and the volume of the sample holder, a calculated amount of the hydrated material was balanced and compacted between two holders of the high-pressure freezing apparatus to make a sample with a target thickness of 200 μm and a diameter of 5 mm. This cylindrical dimension resulted in a target volume of 3.9270 mm^3. The target dry bulk densities of 1.3, 1.5, and 1.7 g/cm^3 and high degrees of saturation were considered for the final state of the compacted material. The sample properties in terms of degree of saturation and porosity after preparation and back analyses are listed in Table 1. Compaction of the material was achieved using a special compaction mold within the sample holder of the high-pressure freezing apparatus. Then the sample holders were sealed in small clamps and, in order to preserve the water contents of the samples, the clamps were sealed using paraffin films.

Electron microscopy (FIB/scanning electron microscopy – SEM/transmission electron microscopy – TEM) requires drying of the samples prior to analysis. In order to prevent artifacts, the following procedure was applied (Figure 1). After compaction, the two aluminum half shells including the bentonite slabs were frozen under high pressure (2100 bar) and within milliseconds using the HPM 100 (Leica) high-pressure freezing system. Freezing at high pressure occurs by the injection of pressurized liquid nitrogen. This treatment prevented the formation of ice crystals which otherwise would have affected the delicate framework of the pore space. Using a freeze-fracture system (BAF 060, Baltec), the samples were coated with metal in the frozen state in order to prevent surface charging during FIB-nt. A cryo-transfer device was then used to transport the frozen material to a FIB/SEM instrument (Helios Nanolab 600i from FEI) equipped with an integrated cryo-stage. In this instrument, Focused Ion Beam nanotomography (FIB-nt) was applied to the material in the frozen state.

ANALYTICAL METHODS

Cryo-Focused Ion Beam nanotomography (FIB-nt)

Cryo-Focused Ion Beam nanotomography is done with dual-beam FIB-SEM instruments in which the ion and electron beams intersect under an angle of 52º at a focal point on the sample surface. In order to analyze frozen samples, the instrument is equipped with a cryo-stage, which allows a cooling of the sample down to −125ºC. Before FIB-nt the samples were coated with metal in the freeze-fracturing instrument. The transfer of

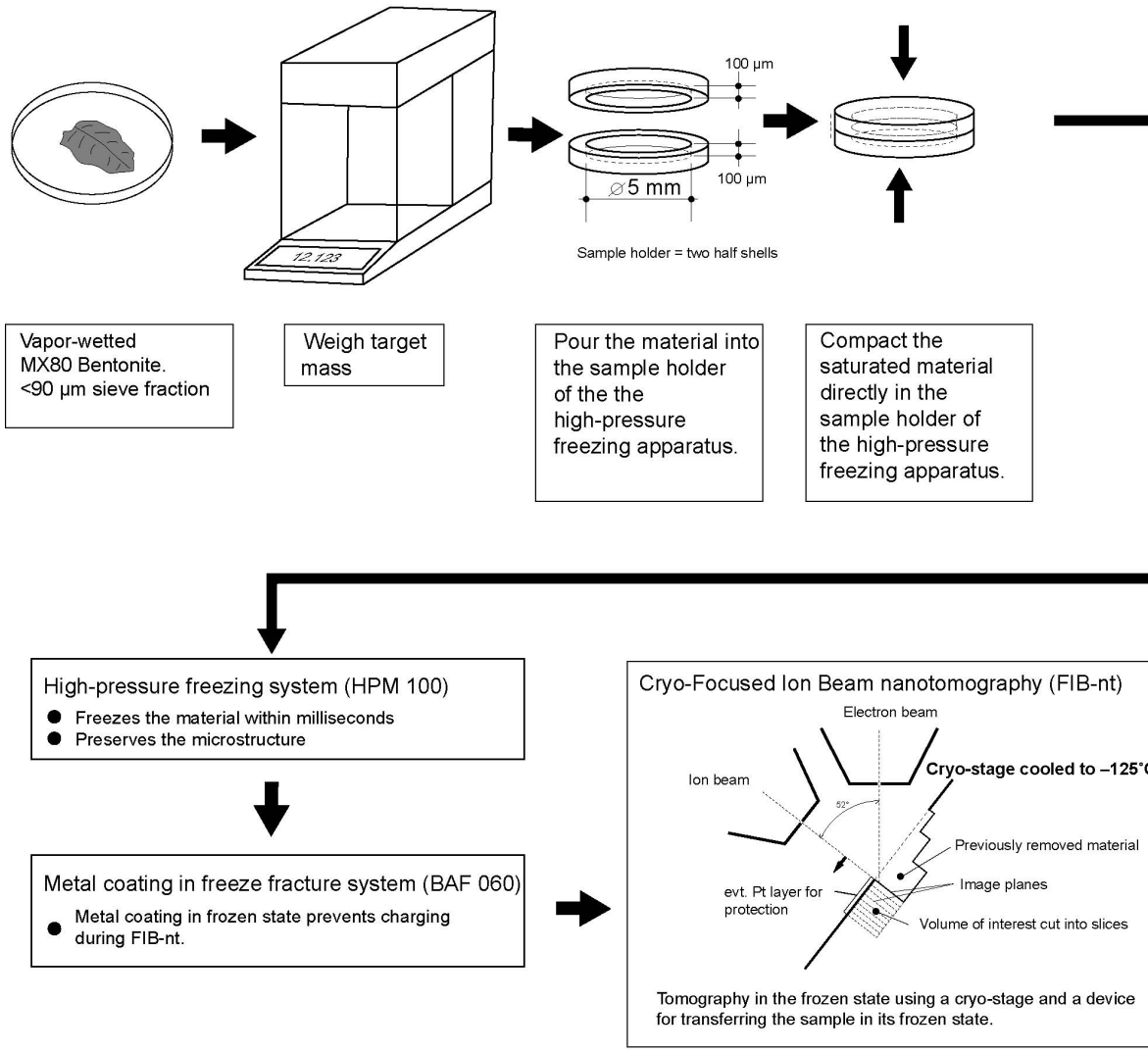

Figure 1. Overview of the methodological approach applied. A calculated amount of vapour-wetted bentonite is compacted in the sample holder of the high-pressure freezing instrument to the required density (see Table 1 and text). The sample is then frozen and analyzed by Focused Ion Beam nanotomography (FIB-nt).

the frozen samples between different instruments (freeze-fracturing instrument to the FIB-SEM) was achieved using a vacuum cryo-transfer system. The 3D information was obtained by acquiring a sequence of cross-sectional images by alternating FIB-slicing and SEM-imaging. The acquired series of images was spaced evenly through a region of the bulk specimen. A stack of these two-dimensional images was then transformed into a three-dimensional representation of the microstructure in the sample. The serial sectioning process began by the milling of a wedge-shaped trench in the sample. The current for ion milling was set at 700 pA. The 'front wall' of the trench was chosen as the initial cross section, which was imaged by the electron beam. After imaging, the ion beam was used to remove a layer of uniform thickness from the front wall, and thus the cross-sectional plane advanced over a predetermined distance through the sample volume. The next electron image was collected from the fresh cross-section. By repeating this alternating milling/imaging process, the cross section advanced through the targeted volume, which resulted in a stack of 2D images.

For the present study, a FEI Helios Nanolab 600i FIB/SEM instrument was used and important instrument setup parameters are listed below. A problem with Cryo-FIB-nt is image-surface charging; this affects the image quality. In order to suppress the effects of surface charging, BSE image stacks only were collected. Backscattered electrons have higher energies when compared to secondary electrons and are therefore less deflected by charged surfaces. For BSE imaging and to prevent charging effects, a low-acceleration voltage of

Table 2. Properties of FIB-nt data sets.

Sample	Volume of image stack (μm)	Porosity (vol.%)	Smallest pore radii (nm)	Figures
7,W.1.3	$17.1 \times 11.2 \times 5.8$	5.6	10	2a, 3, 5, 6
3,W.1.5	$14.7 \times 8.5 \times 1.7$	(no quantification, low quality)	–	7, 8, 9
4,W.1.7	$7.6 \times 12.0 \times 3.0$	0.1	10	2b, 10

1.0 kV and a beam current of 0.34 nA was used. An advantage of BSE images is the notable image contrast between pores and surrounding material which facilitates the image segmentation. The absolute size of the volumes analyzed, resolved pore radii and bulk porosity are listed in Table 2. The quality of the image stack of the sample with a density of ~1.5 g/cm^3 was poor and only allowed a segmentation of the gel-like material. The poor image quality was related to the unloading problems of electric charges from the thermally isolated cryo-stage during acquisition of the image stack. This problem did not appear during the acquisition of the other two image stacks. For the 1.5 g/cm^3 sample, single high-quality 2D BSE images of FIB-prepared cross-sections were acquired.

Image analysis

The position of single BSE images was aligned (in x and y coordinates) relative to the next successive image in the sequence (z direction) using a difference-minimization algorithm that is implemented in the freely available image-processing software, *Fiji* (http://fiji.sc/Fiji). The maximum overlapping area of an orthogonal cube was cropped from the aligned BSE image stack. Noise in the BSE images was reduced by application of an edge-preserving 3D median filter available in the *Avizo* software (http://www.vsg3d.com/avizo/overview). The reconstruction of a 3D microstructure required the segmentation of solid and pore phases in the images, *i.e.* the voxels representing either particles or pores have to be identified in the images and labeled accordingly. In addition, attempts were made to segment the honeycomb structure (see below) of the 'gel-like' material. Segmentation was done by means of tools for pore segmentation provided in the *Avizo* software. The procedure starts with a so-called range calibration of the image stack, which involves the calculation of a gray-level histogram showing number of voxels *vs.* gray values. In this histogram the peak, which corresponds to pore voxels, was identified and the range of gray values corresponding to pore voxels was determined by the position of the minima separating the pore-voxel peak from peaks of other phases. The application of an edge-preserving 3D media filter to the image stack reduced the noise. The pore voxels were then segmented from the images by intensity thresholding, which is applied according to the preset range calibration and can be adjusted interactively based on visual inspection. The information from segmentation was then combined into a single 3D volume. For 3D visualization, the *Avizo* software was used.

RESULTS

The porosity resolved and comparison based on qualitative observations

Here, the focus was on the intergranular porosity (*i.e.* radii >10 nm) that could be resolved by FIB-nt. Porosity was determined on the basis of the segmented image stacks and corresponds to the ratio between void volume and the analyzed volume.

All microstructures contained open and air-filled pores but to very different extents (Figure 2). At dry densities of ~1.7 g/cm^3 only very few isolated pore objects were observed (Figure 2b). The appearance was dense and the material lacked a clay gel. At lower densities (1.24 and 1.46 g/cm^3) the material contained clay aggregates, which formed a mesh-like framework or skeleton similar to the honeycomb structure observed in diagenetic smectites (*e.g.* Tompkins, 1981). This mesh-like material was found to be structurally distinct from clay gels which form from clay suspensions (see below). A greater fraction of pores was only observed at the lowest dry densities (1.24 g/cm^3) (Figure 2a).

FIB/SEM analysis: dry density $\approx$ 1.2 g/cm^3

A 3D reconstruction of the pore space in bentonite with a dry density of 1.2 g/cm^3 is shown in Figure 3 which is based on the BSE-stack from FIB-nt. At this density, bentonite contained a significant number of intergranular pores with radii >10 nm which formed due to geometric incompatibilities between clay grains with a grain size of a few microns (Figure 3). The image volume analyzed contained a relatively large non-clayey mineral grain, which occupied a large portion of the volume. Note that pores were mainly found in the fine-grained clay matrix. Hence, the segmented pore volume was related to the volume of the fine-grained matrix, which yielded a porosity of ~5.5 vol.% of the clay matrix. Continuous pore-size distributions (Münch and Holzer, 2008) were then determined for the observed intergranular porosity. The cumulative size distributions are shown in Figure 4a. The dashed curve represents the pore-size distribution of bentonite with a dry density of 1.2 g/cm^3. The corre-

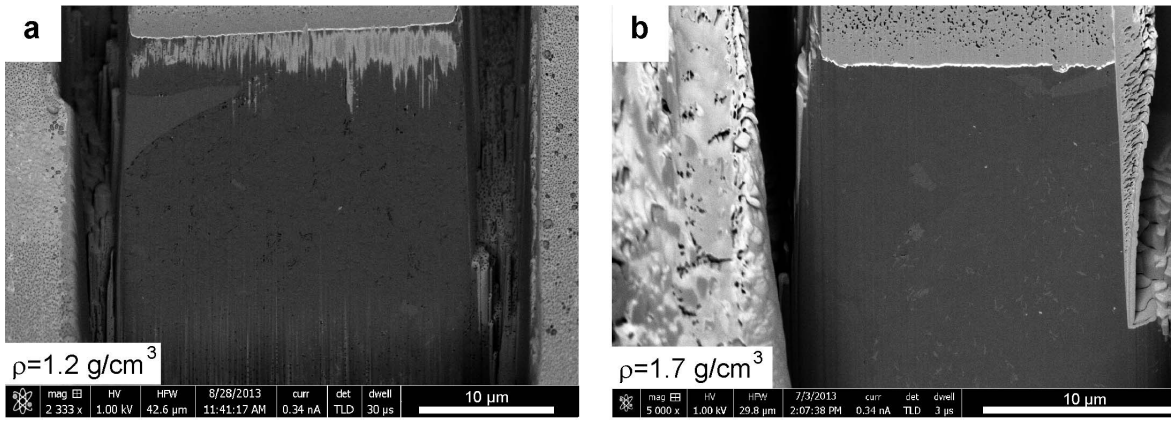

Figure 2. (a,b) BSE images showing the material analyzed by cryo FIB-nt. Note the difference in intergranular porosity between the two samples. The resolved pores are filled with air indicating that the water is mainly stored in the interlayer region.

sponding pore radii ranged between 10 and 250 nm with the majority of pores having radii of ~50 nm. The resolved pore space consisted of large numbers of predominantly unconnected pore objects. In Figure 3b each pore object was labeled with a different color. Based on visual inspection, greater connectivity was observed in the vicinity of the large non-clayey grain (Figure 3). One might argue that this is an artifact related to sample preparation. Close inspection, however, showed that these pores are bridged by delicate clay aggregates (Figure 3c). In the case of an artifact, these bridges should have broken, which was not the case. Larger pores around the non-clayey grain were considered as an original microstructural property of the material at the given bulk properties (*i.e.* lower densities).

At the density under consideration, bentonite contained porous domains which consisted of a mesh-like framework of clay aggregates, which are arranged in a manner similar to the honeycomb structure observed in diagenetic smectites (Figures 5, 6). The cells in this honeycomb framework are partly filled with a colloidal material (Figure 5c). To a certain extent, this material resembled a clay gel, which was also observed in clay suspensions (see below and Luckham and Rossi, 1999 for a review). For the cell cores in the framework, a volume fraction of ~26 vol.% was determined (Figure 6c). The thickness of the clay aggregates making up the framework ranged between ~20 and 50 nm (Figure 5), suggesting that the walls consisted of several parallel clay platelets. Pore radii related to this clay skeleton were in the 10–100 nm range (Figure 6c and dotted curve in Figure 4b). In addition, a 3D reconstruction of the mesh-like framework revealed an anisotropic structure (Figure 6c).

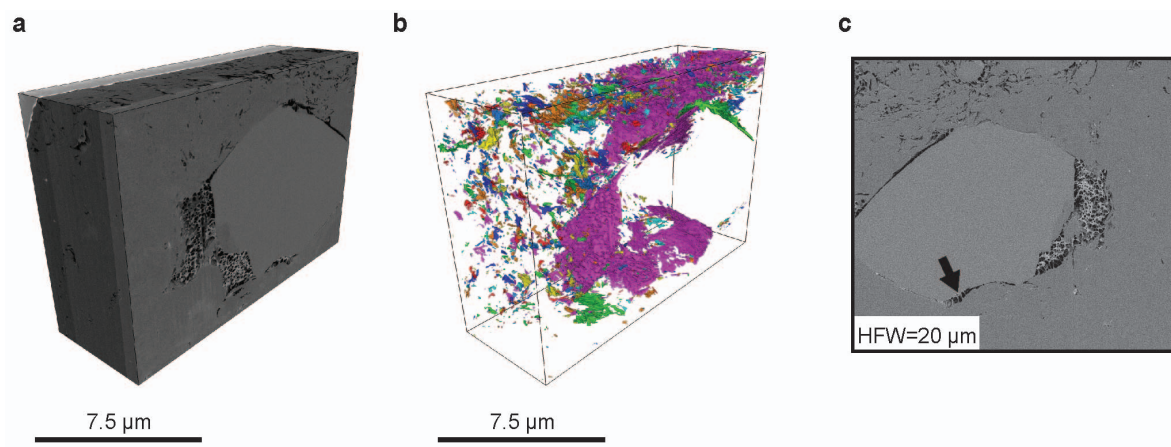

Figure 3. Visualization of FIB-nt data from bentonite using a density of 1.2 g/cm^3. (a) Reconstruction of the volume of material analyzed based on BSE images. Note, the large non-clayey mineral grain and the mesh-like framework or skeleton along its boundary (see discussion). (b) 3D reconstruction of the pore space. The colors indicate individual pore objects. (c) BSE image showing that pores between the non-clayey grain and the clay matrix are bridged by filigree clay aggregates (black arrow). This indicates that the larger intergranular pores are not an artifact from sample preparation but a genuine part of the microstructure.

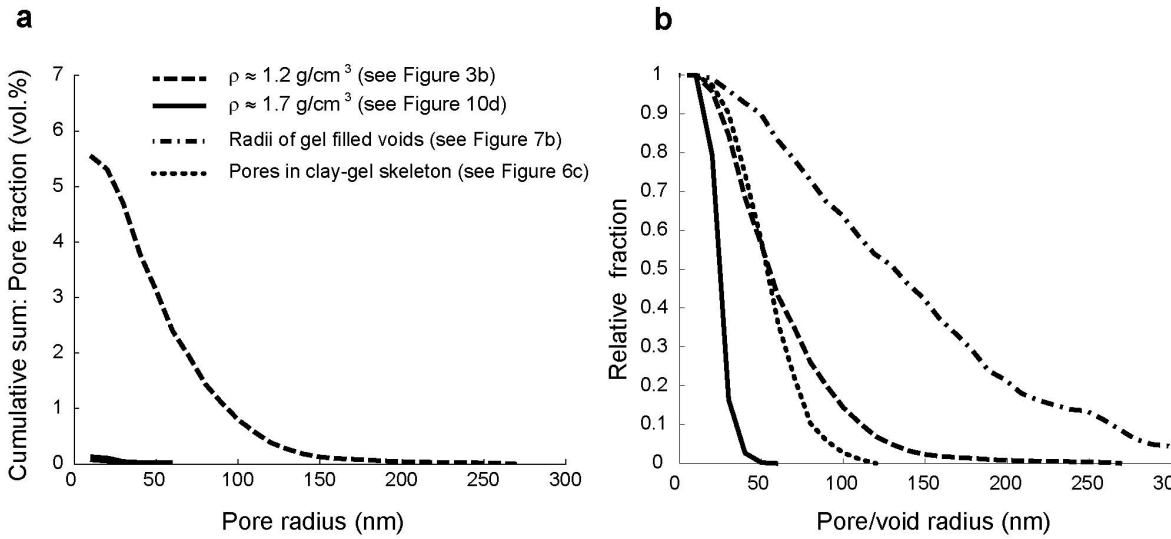

Figure 4. (a) Continuous pore-size distributions relative to dry bulk densities of 1.2 and 1.7 g/cm^3 obtained by analysis of image stacks from FIB-nt. (b) Plot shows the relative distributions of pore/void sizes (*i.e.* total pore volume normalized to 1), which allows comparison between different materials or different domains within one material. The dashed line corresponds to the pore space depicted in Figure 3b (bentonite with density 1.2 g/cm^3). The solid line corresponds to the pore space depicted in Figure 10b (1.7 g/cm^3). The dotted/dashed line corresponds to the gel-filled voids = Figure 7b (1.5 g/cm^3). The dotted line corresponds to an open pore of the clay-gel skeleton (Figure 6c).

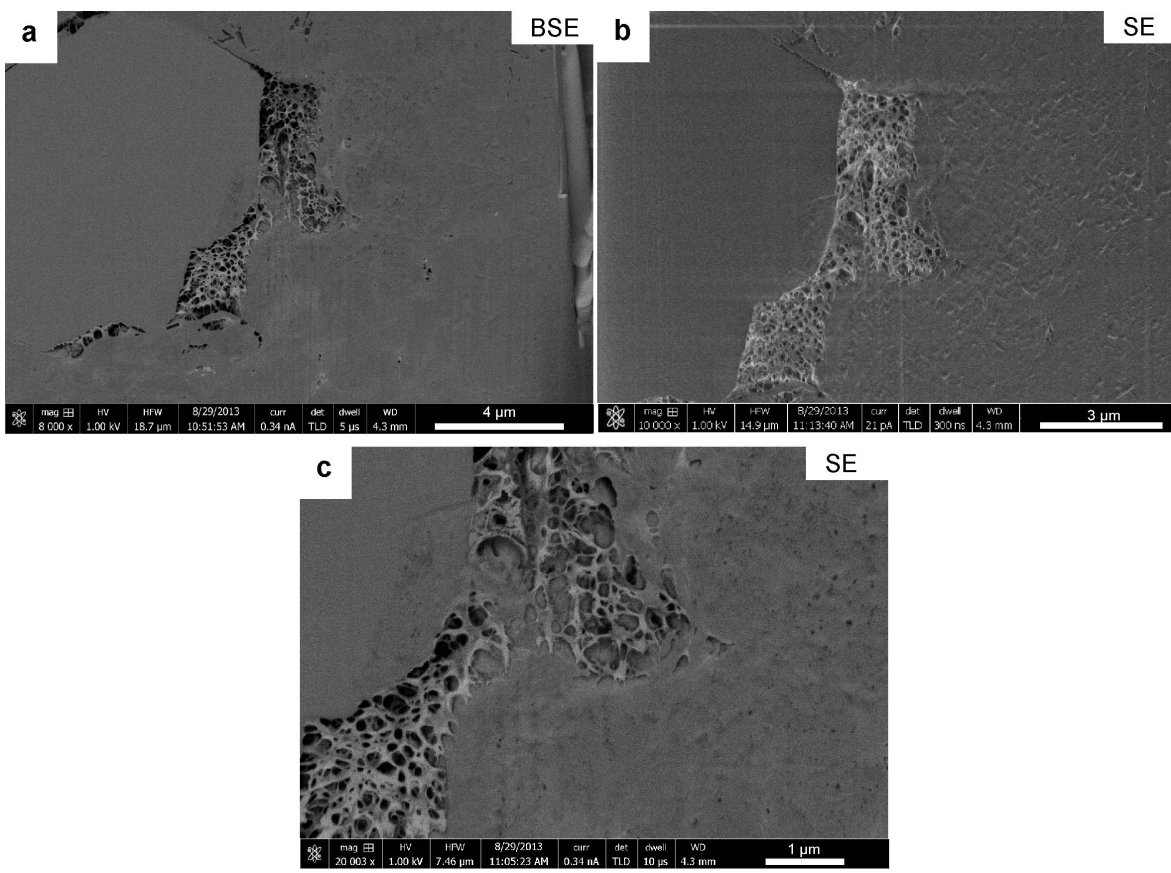

Figure 5. BSE and SE images of bentonite with a density of 1.2 g/cm^3, showing the mesh-like framework. (a) Overview showing that the framework is formed along the boundary of non-clayey grains. (b) SE image of the framework. (c) BSE image at higher magnification reveals that the network is partly filled with some other material (*i.e.* a colloidal gel).

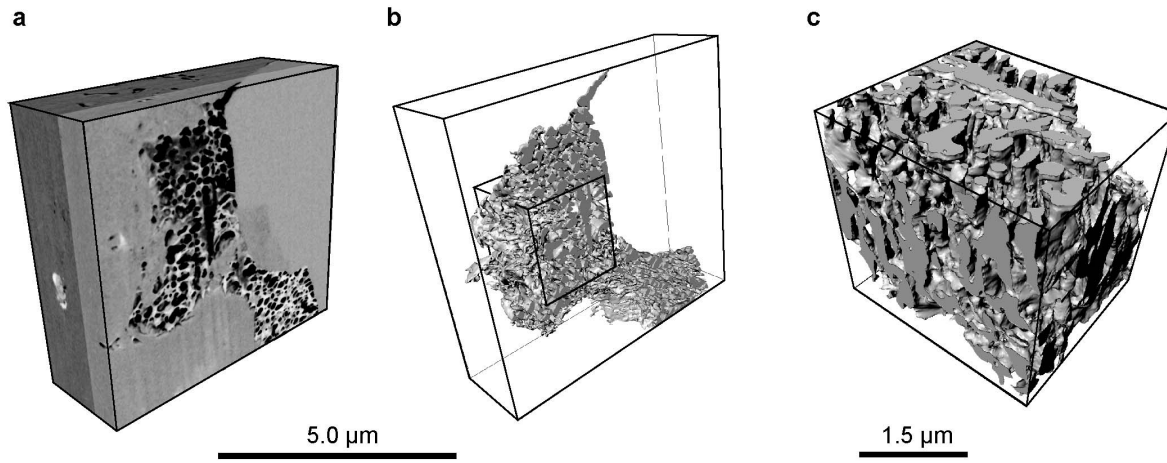

Figure 6. 3D visualizations of the mesh-like framework of the clay gel (in bentonite with a density of 1.2 g/cm^3). (a) 3D reconstruction of the material analyzed based on BSE images (the sub-volume was cropped from the volume of material depicted in Figure 3a). (b) 3D reconstruction of the open pore space in framework. The black cube indicates the sub-volume shown in Figure 6c. (c) Detail showing the geometry of the open pore space in the mesh-like framework. The image shows that the pore space is anisotropic.

FIB/SEM analysis: density ≈ 1.5 g/cm^3

Problems related to surface charging affected the image quality significantly but a segmentation of the image stack into a clay matrix and a honeycomb structural material was possible with reasonable accuracy (Figures 7, 8, 9). A 3D reconstruction of the void space filled with a honeycomb-structured material is given in Figure 7b. The clay gel fills the voids between clay grains. The radii of these filled voids ranged between 10 and 300 nm (Figure 4b, dashed/dotted curve). Based on high-quality BSE images, which were acquired after FIB-nt, no open pores were detected in the bentonite sample (Figure 8).

After imaging in the frozen state, the sample was heated slowly under high vacuum in order to sublimate the free water (*i.e.* amorphous ice) that presumably fills the pores. Under the high vacuum of ~10^{-4} Pa, sublimation began at temperatures of ~−110ºC. BSE images at −125ºC, −90ºC, and a SE image at room temperature are shown in Figure 9. Note that the cores of the honeycomb structure were still filled with some low-density material even at room temperature, very unlike the behavior in sublimation experiments performed with frozen bentonite suspensions (*e.g.* Bhuiyan, 2013). In the latter case the clay aggregates were embedded in vitrified water (*e.g.* Bhuiyan, 2013) and sublimation allowed etching of ice in order to reveal the structure. In contrast, the filling of the honeycomb structure in the investigated bentonite could not be removed by sublimation, which was a clear indication that this filling was not pore water. In addition, the honeycomb structure in Figure 9 did not deform plastically under the force of gravity, which implied that the structure has yield-strength characteristics. The BSE images showed that the cores of the honeycomb structure are darker when compared to the clayey framework and surrounding clay minerals (Figure 8). This suggested that the cores are filled with a material with relatively low density. Local observations of small open pores on the sample surface indicated the presence of small water-filled pores. The presence of free water in the bentonite sample was confirmed by the breakdown of the vacuum upon heating, which indicates degassing of frozen water.

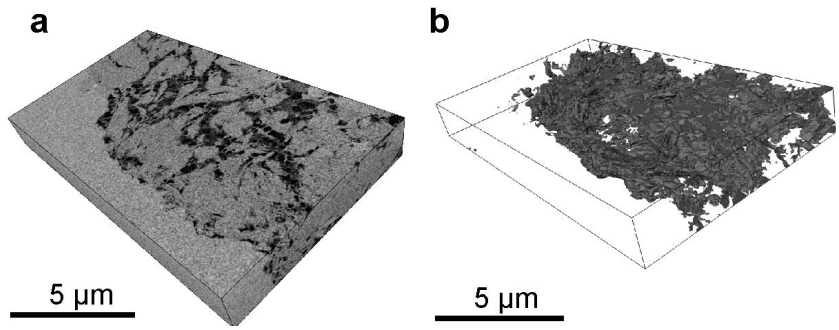

Figure 7. Visualization of FIB-nt data acquired from a bentonite with 1.5 g/cm^3 density (Table 1). (a) Reconstruction of the volume analyzed based on BSE images. (b) 3D reconstruction of the intergranular pore space which is filled with clay gel.

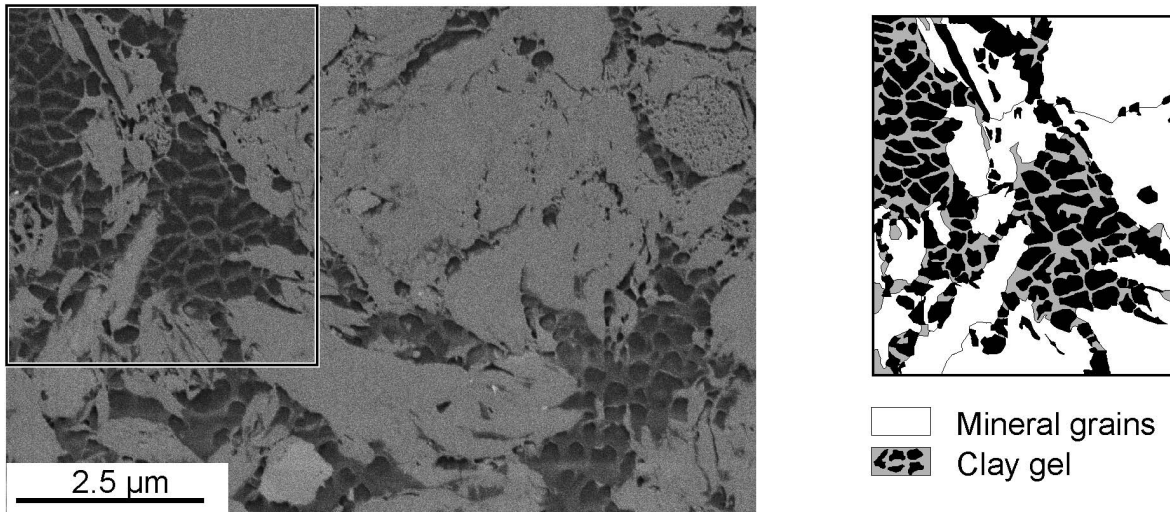

Figure 8. BSE image with marked area corresponding to the sketch (right) showing a domain with abundant large intergranular voids which are filled with a clay gel.

Furthermore, the *in situ* sublimation experiment showed the kinds of microstructural artifacts that can be expected during freeze-drying of the clay samples. The arrows in Figure 9c indicate the cracks which formed during sublimation. Such cracks developed preferentially around larger grains and were probably formed during drying of the fine-grained matrix, which led to delamination cracks between rigid grains and shrinkage of the clay matrix.

FIB/SEM analysis: density ≈ 1.7 g/cm^3

A collection of images and a 3D reconstruction of the pore space, all corresponding to the sample with the highest density, are shown in Figure 10. Note that this

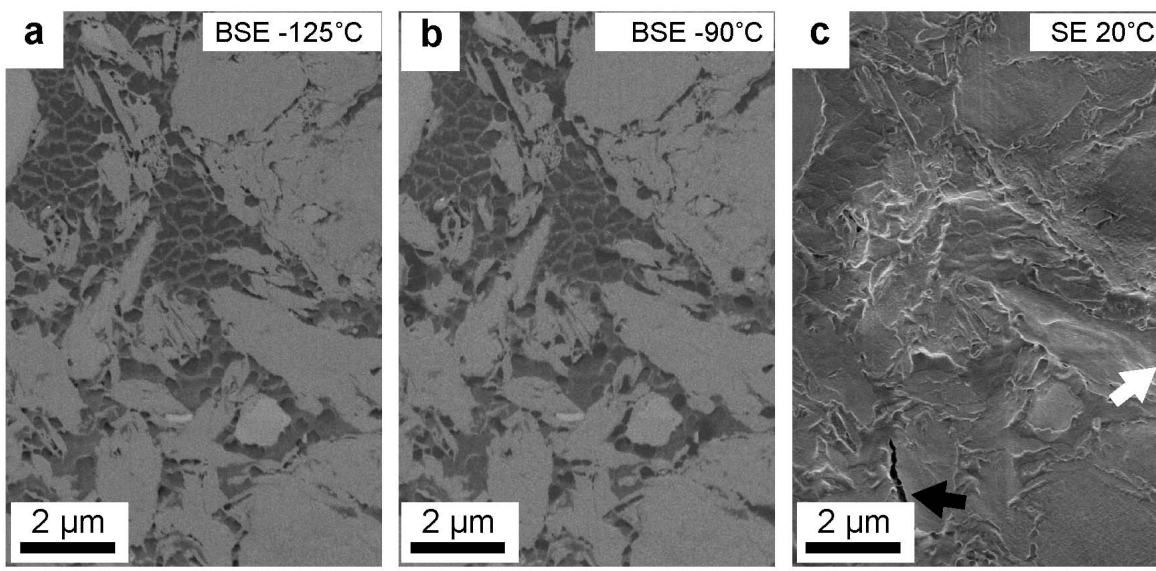

Figure 9. Images showing effects of defreezing, under high vacuum, on the sample with a density of 1.5 g/cm^3, which leads to the sublimation of the amorphous ice in the sample. (a) BSE image showing the material in frozen state (−125ºC). (b) BSE image showing the material at −90ºC and after the start of sublimation. (c) SE image showing the material at room temperatures. The SE image indicates that the majority of the low-density regions observed in the BSE image are filled with a material other than water. The honeycomb structural material does not collapse under the force of gravity, which suggests that the yield strength that may be associated with the low-density filling within the honeycomb cells. Only small numbers of water-filled pores were observed. The white arrow indicates an example of a small empty pore, from which water was removed upon sublimation. The black arrow indicates a crack which formed as a consequence of shrinkage during drying.

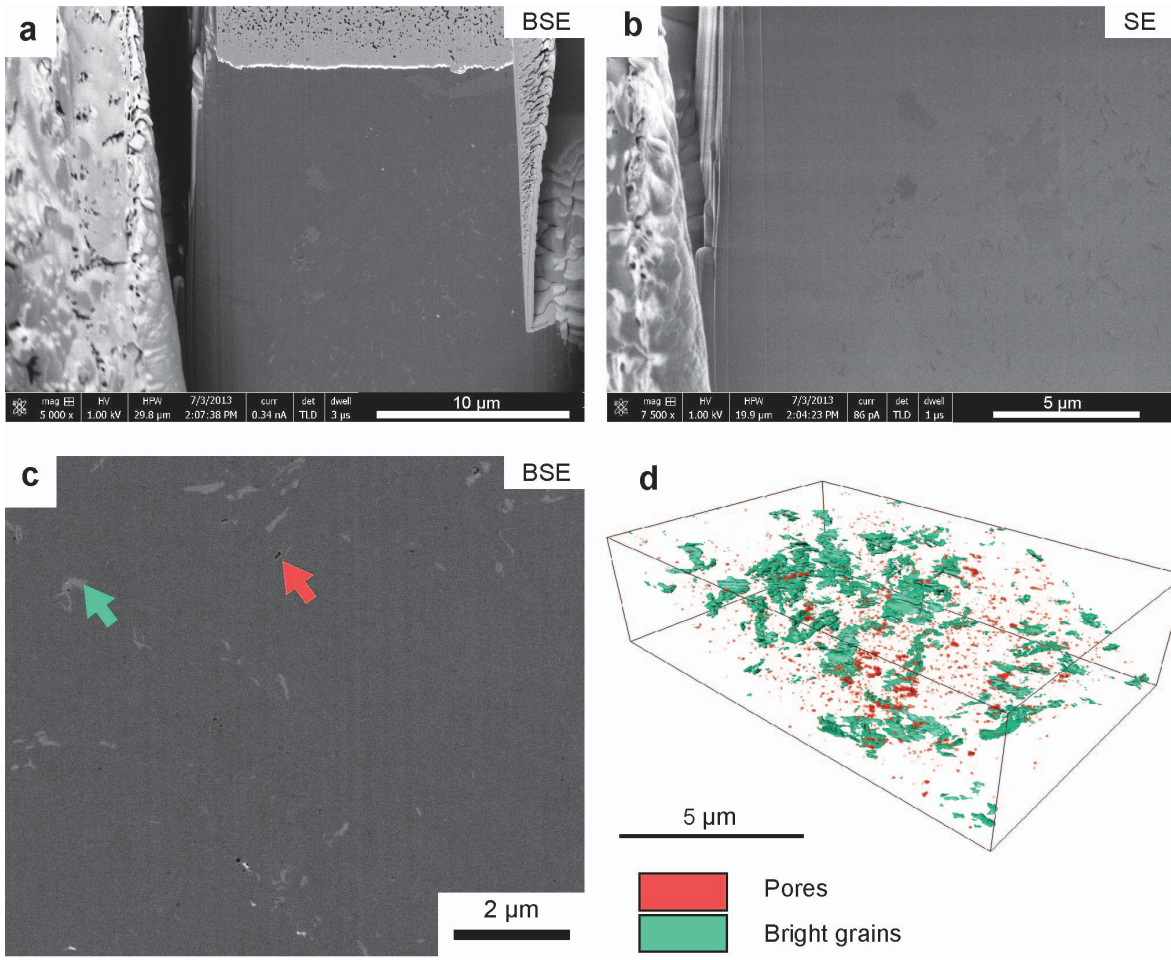

Figure 10. Visualization of the microstructure in bentonite (density of 1.7 g/cm^3) based on data from FIB-nt. (a, b) BSE images of the material analyzed indicating the high density of the material. Clay-gel and larger intergranular pores are absent. (c) A few small intergranular pores can be observed (red arrow). The green arrow indicates a bight mineral present. (d) 3D reconstruction of the pore space (0.1 vol.%) and the bright mineral grains.

sample was more compacted and more water-saturated than the samples at lower densities (Table 1). The microstructure appeared dense (Figure 10a,b,c) and contained numerous bright mineral grains that were dispersed in the clay matrix. These grains are probably impurities (*i.e.* feldspar, calcite). Unlike the low-density samples, clay gel was absent from the sample under consideration. At this higher density, the sample contained only a very small fraction (0.1 vol.%) of open pores. The majority of these rare pores had radii in the 20–30 nm range (Figure 4a). The pore space resolved consisted of isolated pore objects which did not form a connected pore network (Figure 10d).

DISCUSSION

Evolution of intergranular porosity during swelling

Several types of pores have been described in swelling clays. The sizes of pores between mineral layers are in the range of ~1 nm and discontinuities between face-to-face oriented stacks of mineral layers are in the range of 3–4 nm (Tessier, 1990). This pore-size range could not be resolved by FIB-nt. Given the 10 nm resolution (*i.e.* voxel size of FIB-nt), however, the resolved pores with radii >~10 nm were related to the intergranular pore space. Regarding the irregular shape of the clay grains (Figures 2, 3, 8), the resolved pores are obviously linked to geometric incompatibilities between grains or to discontinuities between aggregates of mineral layers, and compaction led to a decrease in the number of these pores and their sizes (Figure 2). The sample material was re-hydrated under unconfined conditions and was subsequently compacted for reasons relating to sample preparation. If re-hydration of compacted dry material occurs under confined (*i.e.* constant volume) conditions, intergranular pore volume accommodates the swelling of the clay minerals. At dry densities of >~1.6 g/cm^3 the initial porosity was interpreted to be too small to accommodate all the swelling, which was supported by a marked increase in swelling

pressure with increasing dry density (Bradbury and Baeyens, 2002). In the present study, reduction in porosity occurred during compaction of re-hydrated material with well defined properties and known dry densities. One might argue that the approach taken led to different microstructures as though swelling occurred under constant-volume conditions. At least in terms of porosity this was obviously not the case because the results obtained were in good agreement with the porosity-reduction process inferred from swelling-pressure curves for materials with different dry densities. The study showed that the intergranular porosity resolved at a dry density of ~1.2 g/cm^3 (water saturation ~70%) is ~5 vol.% and substantially reduced to ~0.1 vol.% if dry densities increase to ~1.7 g/cm^3 (water saturation ~97%). At dry densities of ~1.2 g/cm^3 re-hydrated bentonite still contained air-filled pores, which indicated that most of the water content was in the interlayer region. The breakdown in the vacuum during sublimation inside the SEM sample chamber suggested, however, that some free pore water was present, which was probably stored as external water in pores that were not resolved by FIB-nt.

In terms of the relevance of the approach used to a nuclear-waste repository, where large volumes are to be filled with bentonite backfill material, note that variations in dry densities related to the installation of the backfill could still be observed after 8 years of natural wetting (see Jaremalm *et al.*, 2013). Another cause of density variations was upward swelling which resulted in lower densities in the upper part of the deposition holes. Finally, variations in the water ratio and dry density were observed in different parts of deposition holes (see Jaremalm *et al.*, 2013). Density variations, caused by inhomogeneous swelling and variations in water ratios, suggest that compaction of partially saturated bentonite material requires attention during the safety assessment of bentonite to be used as a backfill material. Hence, the pore microstructure present should be regarded as a potential property of the material to be characterized under application conditions.

For solute transport in dense bentonite, a multi-porosity model with larger intergranular pores and interlayer pores was proposed (*e.g.* Bradbury and Baeyens, 2002). Due to negative surface charging of mineral layers, anions were assumed to be expelled when passing through the interlayer region; water-filled intergranular pores were assumed to represent preferred pathways for anion diffusion. If this is indeed true the connected intergranular porosity (*i.e.* diffusion-accessible porosity) can be estimated on the basis of anion-diffusion experiments. A comparison between the porosity data observed and values calculated for the diffusion-accessible porosity yielded an inconsistent picture. Accounting for the dependence of the accessible porosity on the ionic strength of the pore water, Van Loon *et al.* (2007) calculated the intergranular porosity on the basis of Cl^- diffusion experiments. At a dry density of 1.2 g/cm^3 an intergranular porosity of ~25 vol.% was calculated which is about five times greater than the measured intergranular porosity in the present study (5.5 vol.%). At a dry density of 1.7 g/cm^3 an intergranular porosity of 8 vol.% was calculated, which is about two orders of magnitude greater than that observed for the same dry density at almost full water saturation (0.1 vol.%). At greater densities in particular, the discrepancy might be related to the fact that FIB-nt only resolved pores with radii $\geqslant$10 nm and therefore provided no data for smaller pores. Theoretical calculations of the pore sizes in dense bentonite, ignoring the presence of larger pores, suggested that the pore diameter is <10 nm for dry densities >1.2 g/cm^3 and smaller than the interlayer width (*i.e.* three layers of water) for densities >~1.6 g/cm^3 (Tournassat and Appelo, 2011). The present study has documented the presence of a significant proportion of larger pores at lower dry densities, which, in combination with smaller pores, probably form the connected pore network for anion transport. At greater dry densities, larger pores were not present and theoretical calculations showed that the intergranular pore size approaches the value of the width of the interlayer. Regarding the concept of anion exclusion this poses a problem and one must either assume that anions have access to the interlayer regions or the presence of larger pores that are formed as a result of structural modifications at high dry densities. The present study has documented the formation of a clay gel, which is characterized with lower densities (see below) than the surrounding high-density clay grains. Such a bentonite microstructure with an inhomogeneous density distribution could explain anion diffusion at large dry bulk density values.

The nature of 'clay-gel' in bentonite

Regarding the application of bentonite as backfill material, the following scheme of intergranular pore evolution upon water uptake is widely accepted. In the course of water saturation clay aggregates expand and after a sufficiently long time the intergranular pores will be filled by clay gel, which emerges from expanding aggregates. The intergranular pore space is expected to be partly or entirely filled by the clay gel (Liu *et al.*, 2006; Pusch, 2001; Pusch *et al.*, 1990). The formation of clay gels is related to the expansion or swelling of clays. If dry clay is placed in a moist atmosphere, the clay minerals adsorb water vapor in the interlayer region which causes the clay particles to separate or disjoin. This process is referred to as swelling and it proceeds until the separation reaches equilibrium at a given pressure (*e.g.* Luckham and Rossi, 1999). If the concentration of small clay particles is large enough, flocculation will lead to the formation of a continuous gel structure instead of individual flocs (*e.g.* Luckham and Rossi, 1999). The gel structures build up slowly with time, as the particles orient themselves

toward the position of minimum free energy under the influence of the Brownian motion. The concentrations of clay and salt are decisive factors in the length of time required to attain maximum strength (Darley and Gray, 1988). For Na-montmorillonite this concentration is usually >3% (w/w).

The clay content in the material analyzed in the present study was very much greater than that of a typical bentonite suspension which suggests that the 'clay-gel' that is supposed to form in intergranular pores has different properties. This notion is supported by the observation that the thickness of network walls built by face-to-face aggregated sheets depends on the clay concentration (Vali and Bachmann, 1988). Imaging by FIB-nt and SEM revealed that honeycomb-structured clayey material fills the intergranular space between larger clay grains. This material has a mesh-like structure which is similar to the honeycomb structure observed for diagenetic or authigenic smectites. Based on visual comparison, the honeycomb structure observed is better organized when compared to the networks formed in bentonite suspensions (*i.e.* the material is characterized by a better mechanical stability). The volume fraction of clay corresponding to this structure is >~30 vol.% and the thickness of the 'walls' is tens of nanometers. The latter suggest that the walls are built up by more than ten face-to-face mineral layers (Figure 11). Interestingly, the cores or cells of the honeycomb structure are not filled with free water. The BSE images indicate that the core fill has a lower density than the surrounding clayey material leading to the hypothesis that the core fill consists of a clayey material that is structurally different from the surrounding face-to-face aggregates of the honeycomb structure. The lower density might be related to the presence of more water layers between mineral layers (Lagaly and Dékány, 2006) as well as an irregular organization of mineral layers or stacks of layers, similar to a colloidal gel (Figure 11).

At low dry bulk densities (1.2 g/cm^3), the honeycomb structural material partly fills the intergranular pore space. At intermediate densities (1.5 g/cm^3), this material fills the pores between larger clay grains entirely. At high densities (*i.e.* 1.7 g/cm^3), the clay gel was no longer present. The BSE images of the 1.5 g/cm^3 sample suggested that the clay fraction corresponding to the honeycomb framework is at least 30 vol.%. At such high clay concentrations the paste-like material has yield characteristics and flow resistance under the force of gravity was confirmed *via* 'sublimation' in the SEM.

Saturation occurred under non-confined conditions over an extended period of time and thus it was very likely that the honeycomb-structured material formed during saturation. In such a case, subsequent compaction is expected to modify the delicate structure. This material was only observed at lower dry densities, however, when intergranular pores were still present. The presence of intergranular pores in combination with the evident mechanical strength of the material is probably the reason why the material was largely preserved during compaction after re-hydration. For lower dry densities no reasons were found to exclude the formation of such a honeycomb-structured material in cases where re-hydration occurs under constant volume (*i.e.* under confined conditions). At greater bulk densities (*i.e.* 2.0 g/cm^3) a honeycomb-structured material was not observed and might have been modified beyond recognition during compaction. At such high densities, however, intergranular pores are largely absent and if present the pore radii are on the order of tens of nm. In contrast, the mesh-size corresponding to the clay-gel framework is on the order of 100s of nm long and is thus larger than the pores at high bulk densities. This

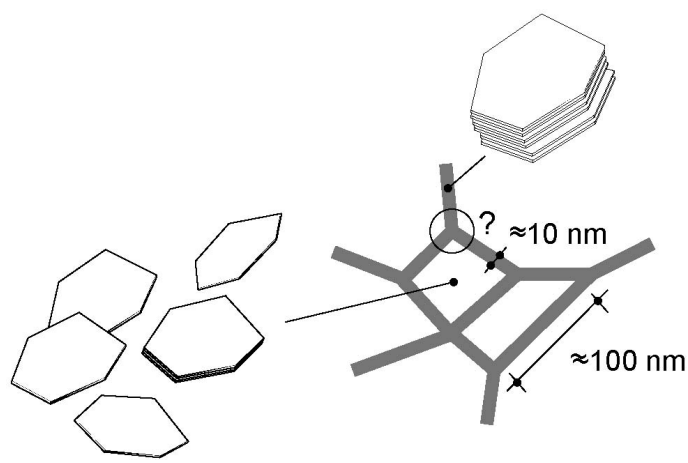

Figure 11. Possible clay-mineral layer associations in the honeycomb-structured material observed. The walls are probably composed of face-to-face-arranged mineral layers. In the cores of the cellular structure, very fine mineral layers are randomly organized and the packing is less dense (similar to colloids with relatively low solid loadings). The low density in the core fillings may also be due to an increased number of water layers between the single mineral layers or between the stacks of mineral layers.

size relation suggests that honeycomb-structured material in intergranular pores can only be formed at comparatively low densities (*i.e.* lower pressures) and in the associated larger intergranular pores. At higher pressures, gelation is obviously suppressed because clay platelets cannot arrange themselves into an energetically stable structure simply due to the lack of space between the larger clay grains.

CONCLUSIONS

A new method was presented, which allowed artifact-free investigation of the microstructures in bentonite samples with different degrees of compaction and associated bulk properties. The method provided systematic results related to MX-80 bentonite microstructures and gave insight into the nature of transport pathways in compacted bentonite.

The generalized picture of an MX-80 bentonite microstructure where a 'clay gel' fills the intergranular pore space can be confirmed. The possibility of deviations from this general picture should be considered, however.

At low densities (*i.e.* dry density of 1.2 g/cm^3) and a water saturation of ~70%, the intergranular pore space was partly filled with a clay gel. At intermediate densities (1.5 g/cm^3), the intergranular pore space was clogged by a clay gel. Further compaction (*i.e.* pressure) apparently suppresses the formation of clay gel because intergranular pores are too small for the formation of the clay framework, which builds the gel. At high densities (1.7 g/cm^3), a percolating network of intergranular pores was not observed.

Microstructural observations suggest that clay gels are preferentially formed in the pressure shadow of larger non-clayey grains. Therefore, the same methods should be applied to a bentonite/sand mixture in order to systematically explore the effects of non-clayey grains on bentonite microstructures.

In addition, the method should be applied more extensively to pure bentonite samples in order to establish crucial relations such as the porosity/density relation, which would shed more light on the systematics of bentonite microstructures for different degrees of compaction and saturation.

ACKNOWLEDGMENTS

The present work was funded by the Swiss National Cooperative for the Disposal of Radioactive Waste (NAGRA).

REFERENCES

Appelo, C.A.J. (2013) A review of porosity and diffusion in bentonite. *Working report 2013-29*, Posiva, Finland.

Bhuiyan, I. (2013) Microstructural characterization of iron ore green pellets. PhD thesis, Department of Civil, Environmental, and Natural Resources Engineering, Lulea University of Technology, Sweden.

Bourg, I.C., Sposito, G., and Bourg, A.C.M. (2007) Modeling cation diffusion in compacted water-saturated sodium bentonite at low ionic strength. *Environmental Science & Technology*, **41**, 8118–8122.

Bradbury, M.H. and Baeyens, B. (2002) Porewater chemistry in compacted re-saturated MX-80 bentonite – physico-chemical characterization and geochemical modeling. *PSI Bericht 02-10, Paul Scherrer Institut*, Villigen, Switzerland.

Bucher, F. and Müller-Vonmoos, M. (1989) Bentonite as a containment barrier for the disposal of highly radioactive waste. *Applied Clay Science*, **4**, 157–177.

Darley, H.C.H. and Gray, G.R. (1988) *Composition and Properties of Drilling and Completion Fluids*, 5th edition. Gulf Publishing Co., Texas, USA, 643 pp.

Decagon Device Inc. (2002) Dewpoint PotentiaMeter: Operators Manual Version 2.1.

Delage, P. and Cui, Y.J. (2007) Microstructure effects on the hydration and water transport in compacted bentonites used for radiactive waste disposal. Pp. 85–96 in: *Proceedings of 3rd Asian Conference on Unsaturated Soils* (Z. Yin, J. Yuan, and A.C.F. Chiu, editors). Science Press, Beijing, China.

Gens, A. (2010) Mechanics of unsaturated geomaterials applied to nuclear waste storage. Pp. 279–301 in: *Mechanics of Unsaturated Geomaterials* (L. Laloui, editor). John Wiley & Sons, Inc., Hoboken, New Jersey, USA. doi: 10.1002/9781118616871.ch12

Glaus, M.A., Baeyens, B., Bradbury, M.H., Jakob, A., Van Loon, L.R., and Yaroshchuk, A. (2007) Diffusion of ^{22}Na and ^{85}Sr in montmorillonite: Evidence for interlayer diffusion being the dominant pathway at high compaction. *Environmental Science & Technology*, **41**, 478–485.

Glaus, M.A., Birgersson, M., Karnland, O., and Van Loon, L. R. (2013) Seeming steady-state uphill diffusion on $^{22}Na^{+}$ in compacted montmorillonite. *Environmental Science & Technology*, **47**, 11522–11527.

Gu, B. and Doner, H.E. (1993) The microstructure of dilute clay and humid acid suspensions revealed by freeze-fracture electron microscopy: reply. *Clays and Clay Minerals*, **41**, 114–116

Herbert, H.J., Kasbohm, J., Moog, H.C., and Henning, K.H. (2004) Long-term behaviour of the Wyoming bentonite MX-80 in high saline solutions. *Applied Clay Science*, **26**, 275–291.

Holzer, L., Münch, B., Rizzi, M., Wepf, R., Marschall, P., and Graule, T. (2010) 3D-microstructure analysis of hydrated bentonite with cryo-stabilized pore water. *Applied Clay Science*, **47**, 330–342.

Jaremalm, M., Köhler, S., and Lidman, F. (2013) Precipitation of barite in the biosphere and its consequences for the mobility of Ra in Forsmark and Simpevarp. SKB report TR-13-28, p. 203, Swedish Nuclear Fuel and Waste Management, Stockholm, Sweden.

Lagaly, G. and Dékány, I. (2006) Colloid clay science. Pp. 243–345 in: *Handbook of Clay Science* (F. Bergaya, B.K.G. Theng, and G. Lagaly, editors). Elsevier, Amsterdam.

Liu, J. and Neretnieks, I. (2006) Physical and chemical stability of the bentonite buffer. SKB report R-06-103, Swedish Nuclear Fuel and Waste Management, Stockholm, Sweden.

Lloret, A. and Villar, M. V. (2007) Advances on the knowledge of the thermo-hydro-mechanical behaviour of heavily compacted "FEBEX" bentonite. *Physics and Chemistry of the Earth*, **32**, 701–715.

Luckham, P.F. and Rossi, S. (1999) The colloidal and rheological properties of bentonite suspensions. *Advances in Colloid and Interface Science*, **82**, 43–92.

Monroy, R., Zdravkovic, L., and Ridley, A. (2010) Evolution of microstructure in compacted London Clay during wetting and loading. *Géotechnique*, **60**, 105–119.

Münch, B. and Holzer, L. (2008) Contradicting geometrical

concepts in pore size analysis attained with electron microscopy and mercury intrusion. *Journal of the American Ceramic Society*, **91**, 4059–4067.

Pusch, R. (2001) The microstructure of MX80 clay with respect to its bulk physical properties under different environmental conditions. Technical Report TR-01-08, Swedish Nuclear Fuel and Waste Management, Stockholm, Sweden.

Pusch, R., Karnland, O., and Hoekmark, H. (1990) GMM – A general microstructural model for qualitative and quantitative studies of smectite calys. Technical Report TR-90-43, Swedish Nuclear Fuel and Waste Management, Stockholm, Sweden.

Saiyouri, N., Hicher, P.Y., and Tessier, D. (2000) Microstructural approach and transfer water modelling in highly compacted unsaturated swelling clays. *Mechanics of Cohesive Frictional Materials*, **5**, 41–60.

Tessier, D. (1990) Behavior and microstructure of clay minerals. Pp. 387–415 in: *Soil Colloids and their Association in Aggregates* (M.F. De Broodt, M.H.B. Hayes, and A. Herbillon, editors). Plenum Press, New York.

Tomioka, S., Kozaki, T., Takamatsu, H., Noda, N., Nisiyama, S., Kozai, N., Suzuki, S., and Sato, S. (2010) Analysis of microstructural images of dry and water-saturated compacted bentonite samples observed with X-ray micro CT. *Applied Clay Science*, **47**, 65–71.

Tompkins, R.E. (1981) Scanning electron microscopy of a regular chlorite/smectite (corrensite) from a hydrocarbon reservoir sandstone. *Clays and Clay Minerals*, **29**, 233–235.

Tournassat, C. and Appelo, C.A.J. (2011) Modelling approaches for anion-exclusion in compacted Na-bentonite. *Geochimica et Cosmochimica Act*a, **75**, 3698–3710.

Velbel, M.A. and Barker, W.W. (2008) Pyroxene weathering to smectite: conventional and cryo-field emission scanning electron microscopy, Koua Bocca ultramafic complex, Ivory Coast. *Clays and Clay Minerals*, **56**, 112–127.

Vali, H. and Bachmann, L. (1988) Ultrastructure and flow behavior of colloidal smectite dispersions. *Journal of Colloid and Interface Science*, **126**, 278–291.

Vali, H. and Hesse, R. (1992) The microstructure of dilute clay and humic acid suspensions revealed by freeze-fracture electron microscopy: discussion. *Clays and Clay Minerals*, **40**, 620–623.

Van Loon, L.R., Glaus, M.A., and Mueller, W. (2007) Anion exclusion effects in compacted bentonites: towards a better understanding of anion diffusion. *Applied Geochemistry*, **22**, 2536–2552.

(*Received 13 December 2013; revised 5 June 2014; Ms. 826, AE: W.D. Huff*)

Clays and Clay Minerals, Vol. 62, No. 3, 188–202, 2014.

THE INTERACTION BETWEEN BENTONITE AND WATER VAPOR. I: EXAMINATION OF PHYSICAL AND CHEMICAL PROPERTIES

MICHEL HEUSER[1], CHRISTIAN WEBER[1], HELGE STANJEK[1], HONG CHEN[2], GUNTRAM JORDAN[3], WOLFGANG W. SCHMAHL[3], AND CARSTEN NATZECK[4]

[1] Clay and Interface Mineralogy, RWTH Aachen University, Bunsenstrasse 8, 52072 Aachen, Germany,
[2] Department of Materials Technology, Flemish Institute for Technological Research (VITO), Boeretang 200, B 2400 Mol, Belgium
[3] Department for Geo- and Environmental Sciences, Ludwig-Maximilians-Universität München (LMU), Theresienstrasse 41, 80333 Munich, Germany
[4] Institute of Functional Interfaces, Karlsruhe Institute of Technology (KIT), Hermann-von-Helmholtz-Platz 1, 76344 Eggenstein-Leopoldshafen, Germany

Abstract—The influence of water vapor on bentonites or smectites is of interest in many different fields of applied mineralogy such as nuclear-waste sealing or casting in the foundry industry. The water vapor affects the smectite surface and perhaps its structure probably leading to mostly unfavorable changes in its properties. In this first part of the present study, the influence of hot water vapor (200ºC) on the physico-chemical and mineralogical properties of smectite-group minerals was studied. After the steam treatment, turbidity measurements, methylene-blue sorption, water adsorption, and cation exchange capacity (CEC) were measured on both untreated and treated samples. Mineralogical changes were monitored by X-ray diffraction (XRD) and X-ray photoelectron spectroscopy (XPS) was used to measure O, Al, and Si. Only a few parameters showed differences between the untreated and vapor-treated samples. Sedimentation volumes (SV) decreased following the treatment. As shown by XRD and XPS, the crystalline structure of smectite remained unaffected by the steam treatment. Equivalent sphere diameters (ESD) were not affected systematically by the steam treatment. Differences in CEC values between untreated and treated samples were observed, but only for smectites with monovalent interlayer cations. From the variety of different measurements the conclusion of the present study was that steam treatment changes the charge properties at or near the smectite particle surface.

Key Words—Cation Exchange Capacity, Equivalent Sphere Diameter, Methylene Blue Sorption, Water Vapor, XPS, XRD.

INTRODUCTION

The industrial and technical applications of clay minerals and bentonites include geotechnical use in contaminant removal (Viraraghavan and Alfaro, 1996; Mellah and Chegrouche, 1997; Gitipour *et al.*, 1997), drilling or reinforcing fluids (Erdoğan and Demirci, 1996; Luckham and Rossi, 1999), landfill technology (Ashmawy *et al.*, 2002; Scalia and Benson, 2011), ceramics in material science (Zhu *et al.*, 2002; Fahrenholtz, 2008), and molding in foundry technology (Baier, 1991; Beeley, 2001).

By definition, bentonites contain >50 wt.% of smectite-group minerals such as montmorillonite or beidellite (Grim and Güven, 1978; EUBA, 2006; Murray, 2007). For foundry applications, smectite contents of >70 wt.% are preferred (Grefhorst, 2006). Additional minerals include quartz, feldspars, micas, kaolinite, anatase, cristobalite, opal, and volcanic glasses (Ufer *et al.*, 2008; Christidis and Huff, 2009). The physical and chemical properties of bentonite vary with the amount of smectite and mainly with its parameters such as particle size and morphology, hydration state of the interlayer cations, and the presence of free water in the pore space (Montes-H. *et al.*, 2003; Kaufhold *et al.*, 2010).

With regard to foundry technology, molding or green sand consists of refractory material, usually quartz (for special applications zircon or chromite sand is used), bentonite as a binder, special additives such as lustrous carbon producers, and water (Träger and Bührig-Polaczek, 2000; Beeley, 2001; Recknagel and Dahlmann, 2008). Smectite in contact with water encloses the surface of quartz particles and contributes to the plasticity and stability of molding sand. During the casting process, liquid water in the molding sand evaporates near the molten metal to an exceedingly hot vapor moving along the temperature gradient to cooler regions, condensing to liquid water. This region, known as the 'condensation zone', is characterized by water contents greater than they were at the beginning of the casting process (Grefhorst *et al.*, 2005; Jordan *et al.*, 2013). During this transport process water vapor affects the smectite particles and probably their surface properties. This potential modification might be a controlling factor leading to poor quality molding sands.

* E-mail address of corresponding author:
michel.heuser@cim.rwth-aachen.de
DOI: 10.1346/CCMN.2014.0620303

The influence of water vapor on bentonite is also important for the sealing of nuclear-waste repositories. Several decades of research has resulted in a detailed understanding of the influence of water vapor on the geotechnical and mineralogical parameters of bentonite. A vapor treatment was performed at temperatures between 150 and 250ºC by Couture (1985a, 1985b). Both permeability and its ability to swell and to fill fractures decreased significantly up to 250ºC. The reduction in swelling capacity commenced at 150ºC.

A decrease in swelling capacity was also observed (Oscarson and Dixon, 1989) which was not caused by an alteration of the mineralogical composition of the montmorillonite and which was influenced by physical aggregation of clay particles, only to a lesser extent. The permeability of unprocessed and treated bentonites was discovered to be different (Oscarson *et al.*, 1990) but those authors gave no reasons why this was so. Both studies have in common that differences between unprocessed and treated bentonites were observed for water-vapor treatments starting at 110ºC. The positive aspects of untreated bentonites (such as fast swelling and low water permeability) were lost.

A steam treatment at temperatures >260ºC was performed by Güven (1990) resulting in a modified microstructure and a disturbance of the lamellar fabric.

The influence of steam on bentonite at temperatures of <120ºC was assessed by Madsen (1998). Analyses by XRD, infrared spectroscopy (IR), and thermogravimetry showed no significant changes due to steam treatment except for a slight increase in CEC. The reduction of swelling pressure was attributed to aggregation of clay particles.

The effects of steam on the surface properties of two sodium-smectites were studied by Bish *et al.* (1997). No structural mineralogical changes (XRD) after treatment were observed. Based on ^{27}Al magic angle spinning-nuclear magnetic resonance (MAS-NMR) measurements, those authors speculated about a relocation of Al, but the differences between spectra of untreated and vapor-treated samples were few. Contact angles determined with polar liquids were noted to change after steaming, however, whereas non-polar liquids did not show any modification of the contact angles. The water-adsorption isotherms of untreated and steam-treated samples differed and the ability of samples to adsorb water decreased, although with hysteresis effects. A small increase in zeta potentials after the treatment was detected.

The influence of water vapor on bentonite over the temperature range 90−110ºC led to bulk-clay expansion and aggregation (Pusch, 2000). The hydration rate and swelling pressure were of the same order of magnitude for untreated and steam-treated clay, however. The hydraulic conductivity increased by up to 10% due to a more heterogeneous microstructure after the treatment. Partial dissolution of smectite and precipitation of Si or silica after cooling following the treatment induced aggregation and cementation of particles. The Si and Al concentrations were not measured in the present study, however. Changes in the physical properties were insignificant.

In summary, the following effects with steam treatment were observed: (1) the ability to swell and the swelling pressure decreased; (2) the permeability and hydraulic conductivity increased; (3) the CEC increased slightly; (4) no structural changes were evident from studies using XRD, IR, or thermogravimetry.

Based on the results of the studies cited above and their interpretation, the mechanisms and processes of steam/smectite interactions and changes at particle level are still not understood fully. The causes of apparent changes in surface properties after steaming, exemplified by contact-angle and zeta-potential measurements (Bish *et al.*, 1997), are unclear. The focus of the present work was to understand the processes in the system involving hot steam and smectite.

MATERIAL AND METHODS

Five industrial bentonites used for foundry applications (Bentonite C, D, E, H, and W abbreviated hereafter as BeC, BeD, BeE, BeH, and BeW) and two commercial clays (Namorit S and Volclay) were used. The mineralogical characterization of samples is presented below in the section on XRD. The sample-preparation steps were: (1) Ultrasonic dispersion of raw material in deionized water to a concentration of 5 wt.%. (2) Enrichment of smectite by separating the <2 μm fraction by Atterberg sedimentation. (3) Preparation of homoionic forms by washing 10 g of sample material under continuous stirring in 600 mL of a 3 M salt solution of NaCl, KCl, $MgCl_2$, or $CaCl_2$, respectively. After ~36 h the stirrer was switched off, and the particles sedimented. The clear supernatant was removed and replaced by a new 3 M salt solution. This procedure was repeated six times. Bentonites C, D, E, H, and W were prepared in the four forms, Namorit S and Volclay only in the Mg- and Na-species respectively. (4) Dialysis in Roth-Nadir dialysis tubing with a diameter of 50 mm and a pore size of 2.5−3.0 nm to remove the remaining free salts in the clay dispersion. Dialysis was completed when the electrical conductivity of the clay dispersion in the dialysis tubing was <20 μS/cm. (5) Freeze drying of sample material and storage in airtight PVC containers.

The steam treatment was performed in Berghof digestion autoclaves (Figure 1). Deionized water and sample material were poured into the polytetrafluoroethylene (PTFE) insert. The sample insert was placed in the water insert and closed with a lid. Both inserts were placed in the steel body and closed. Steam treatments were performed at 200ºC in an oven for a period of 6 days. Note that the sample had no contact with liquid water during the steam process. For all experiments a smectite-to-water ratio of 1:20 was used. After the treatment the closed autoclaves were cooled for 24 h.

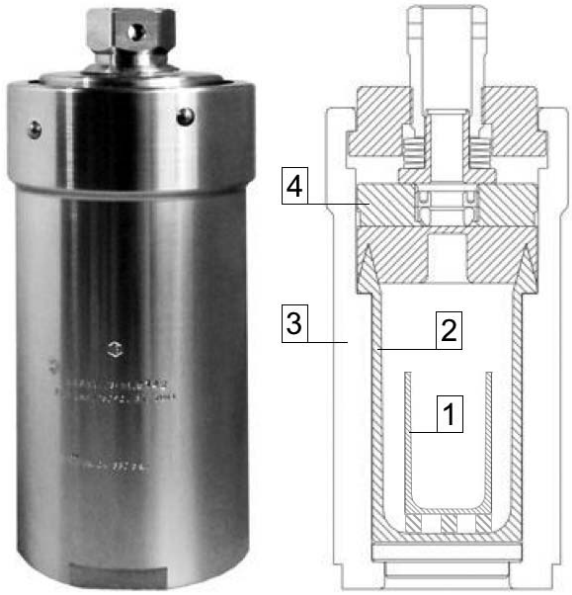

Figure 1. Pressure digestion vessel made of high-alloy stainless steel SS 316 Ti, max. 200 bar, max. 250ºC (Berghof autoclave DAB-3). (Left) Image of stainless steel body with lid; (right) cross section (modified after Berghof, 2012). The autoclave consists of four main components: (1) 50 mL PTFE insert for the sample; (2) 250 mL PTFE insert for the water with lid; (3) high-alloy stainless steel body with bayonet lock; and (4) rupture disc to limit maximum pressure reliably.

Having reached room temperature the clear supernatant was removed for further analysis; the solid was dried at 200ºC for ~1 h, held in a desiccator, and stored in airtight PVC containers.

In order to examine the physico-chemical differences between untreated and steam-treated bentonite samples, laboratory tests were performed as listed below. For all experiments only the <2 μm clay fraction was used.

SOLUTION CHEMISTRY

The ionic composition of the supernatant water after steaming may provide an indication of possible dissolution processes due to the steam treatment. The supernatant was analyzed by ion chromatography (IC 850 Professional, Metrohm, Germany) for anions F^-, Br^-, Cl^-, NO_2^-, NO_3^-, SO_4^{2-}, and PO_4^{3-}, and cations Li^+, NH_4^+, K^+, Na^+, Cs^+, Mg^{2+}, and Ca^{2+}. The lower detection limit was 0.5 mg/L for all ions. The deionized water (Table 1, sample #1) was essentially free of any contamination. For the second test (#2) only water was added to the autoclaves, whereas the standard test procedure remained unchanged. In order to quantify removable ions for the untreated sample, bentonite material was dispersed in deionized water (1:70) and kept in dispersion for five days (#3). After sedimentation, clear supernatant was filtered (0.45 μm) and concentrations of common ions were determined. The last test (#4) represents the standard steam treatment, where the water in the autoclaves was analyzed after steaming.

In order to check if water vapor affects tetrahedral or octahedral sheets, Si and Al were measured in the supernatant. To check whether the concentrations of Al and Si were to be ascribed to the steam treatment, blank experiments were performed. One gram (1 g) of sample was dispersed in 20 mL of deionized water and kept in dispersion for 5 days; the Al and Si concentrations were determined in the clear supernatants. Background concentrations, c_0, of Al ($c_{0,Al}$ = 0.4 mg/L) and Si ($c_{0,Si}$ = 0.1 mg/L) were measured in deionized water and subtracted from sample concentrations.

Silicon was measured by the molybdenum blue method according to Köster (1979, p. 39) at a wavelength of 650 nm. Aluminum was measured using the aluminon red method according to Köster (1979, p. 51) at a wavelength of 530 nm. The relative uncertainties in concentrations are 3 and 0.3% for Al and Si, respectively (Köster, 1979). An UV-VIS spectrophotometer (Specord 210 Plus, Analytik Jena, Germany) was used to perform photometric measurements.

Colorimetry

The change in color in the course of steam treatment was quantified by colorimetry using a Chroma meter

Table 1. Ion concentrations in supernatant water after treatment in selected experiments (three replicates each).

#	Cation [mg/L]	K^+	Na^+	NH_4^+	Mg^{2+}
1	Unprocessed water	0	0	0	0
2	Treated water	0.61	0.93	4.29	0
3	BeW, Mg dispersed in water (1:70)	1.37±0.01	0.77	<0.20	4.32±0.18
4	BeW, Mg, steam-treated	1.18±0.06	1.94±0.18	9.36±0.66	0
#	Anion [mg/L]	F^-	Cl^-	NO_3^-	SO_4^{2-}
1	Unprocessed water	0	0	0	0
2	Treated water	0.47	0.86	0	0.44
3	BeW, Mg dispersed in water (1:70)	0	0.79±0.01	0.85±0.24	0.50±0.09
4	BeW, Mg, steam-treated	2.26±0.19	1.08±0.67	0	0.80±0.27

(CR-400, Konica Minolta, Germany). In the $L^*a^*b^*$ color space (DIN 6174), L^* describes the brightness (luminance) of color, which ranges between 0 (black) and 100 (white). The parameter a^* can range between −150 and +100, where negative values indicate a green and positive ones a red color. The parameter b^* may vary between −100 (blue) and +150 (yellow). Relative uncertainty on L^*, a^*, and b^* is <±1%, according to the Chroma meter manual.

Sedimentation volume (SV)

One gram (1 g) of sample material dispersed in 56 mL of deionized water was poured into graduated cylinders. After adding 3 g of $MgCl_2 \cdot 6H_2O$ (Merck, Germany) to the clay dispersion to facilitate flocculation, the cylinders were shaken and left to sediment for 1 day. The sedimentation volume is given in percent in relation to the initial volume of 56 mL. The test procedure was described by Oscarson and Dixon (1989).

Water adsorption (WA)

Water adsorption or water-uptake capacity is used widely in quality control for industrial clay minerals and bentonites. The water adsorption of untreated and steam-treated bentonites was determined using the method and instrumentation described by Dieng (2005), itself a modification of the Enslin-Neff method (Neff, 1959). For the test, 0.2 g of dry sample material (oven-dried at 200ºC) was brought into direct contact with liquid water. The measurement lasted for 24 h, a time period in which evaporation could be ignored. The relative uncertainty in the water adsorption was ±2.5% (Dieng, 2005).

Cation exchange capacity (CEC)

In order to obtain information about charge conditions in the interlayer of smectite and their change due to steaming, the CEC was determined using the copper(II)-triethylenetetramine (CuTrien) method after Meier and Kahr (1999). For the experiment, 100 mg of sample material was dispersed in 50 mL of deionized water by shaking. Then 2 mL of a 0.1 mol/L Cu-Trien solution, made from $CuSO_4 \cdot 5H_2O$ (Merck, Germany) and triethylene tetramine (>97% purity, Sigma Aldrich, Germany) was added. After 1 h, the dispersion was filtered (pore size of the filter 0.45 μm) and its absorption measured using an UV-VIS spectrophotometer (Specord 210 Plus, Analytik Jena, Germany) at 577 nm (max. absorption of the CuTrien solution). The relative uncertainty in the CEC measurements was ±3%.

Equivalent sphere diameter (ESD)

To determine whether the steam treatment leads either to particle growth or to particle dissolution, equivalent sphere diameters (ESD) of untreated and treated smectites were calculated from turbidity measurements of dispersions having increasing concentrations of solid. Turbidity values can be related to ESD values using the Mie theory of light scattering (Lange, 1968, 1969; Melik and Fogler, 1983; Lange, 1995; Lagaly *et al.*, 1997). One hundred and fifty milligrams (150 mg) of sample material was dispersed in 150 mL of deionized water by ultrasonic treatment (5 min). An aliquot of 0.1 mL was added to 50 mL of deionized water and the dispersion homogenized by a peristaltic pump in a loop including a flow-through cuvette. After measuring absorption at 850 nm, the next aliquot of 0.1 mL was added to the dispersion. This procedure was repeated 20 times, resulting in a total of 20 measurements at increasing concentrations. An UV-VIS spectrophotometer (Specord 210 Plus, Analytik Jena, Germany) was used to measure the absorption.

In order to calculate the particle size, the measured absorption is converted into turbidity according to equation 1, where L is the scattering length of the cuvette (L = 1 cm) and D is the measured absorption (Lagaly *et al.*, 1997):

$$\tau = 2.303 \cdot (D/L) \quad (1)$$

A plot of the clay-water-solution concentration (c) *vs.* the calculated turbidity (τ) should result in a linear function with a slope $\partial\tau/\partial c$.

$$r_{\text{particle}} = \left(\frac{\left(\frac{\tau}{c}\right) \cdot \lambda^4 \cdot \rho}{32 \cdot \pi^4 \cdot n_{\text{fluid}}^4 \cdot \left(\frac{m^2-1}{m^2+2}\right)^2} \right)^{1/3} \cdot 10^7 \quad (2)$$

with $m = n_{\text{solid}}/n_{\text{fluid}}$.

Equivalent sphere radii (r_{particle} in nm) were obtained from the averages of 20 measurements (equation 2 of Lagaly *et al.*, 1997). The wavelength of the photometer is $\lambda = 8.5 \times 10^{-5}$ cm, ρ = 2.6 g/mL is the density of the mineral, n_{fluid} = 1.33 is the refractive index of the fluid (deionized water), and n_{solid} = 1.59 (Lagaly *et al.*, 1997, p. 288) is the refractive index of the solid phase. A slightly smaller n_{solid} was chosen, however, because newer literature (Anthony *et al.*, 2013) provided values of n down to 1.51 for montmorillonite. The absolute error of ESD measurements ranges between 0.5 and 9.0 nm.

Methylene blue absorption (MBS)

The interaction of dye molecules like methyl orange or methylene blue with clay minerals has been studied extensively (Kahr and Madsen, 1995; Bujdák *et al.*, 2001; Jacobs and Schoonheydt, 2001; Ma *et al.*, 2004; Czímerová *et al.*, 2004). The determination of the smectite content in bentonites by methylene blue absorption is a standard method in quality control in foundry technology (Grefhorst, 2006; VDG P35).

For the test, 50 mg of sample material was dispersed in 70 mL of deionized water by ultrasonic treatment for 5 min. Subsequently, 8 mL of a 1.25×10^{-4} mol/L methylene blue solution (Clin-Tech Ltd., United Kingdom) was added. Absorption spectra of clay-dye

dispersions were measured between 400 and 800 nm using an UV-VIS spectrophotometer (Specord 210 Plus, Analytik Jena, Germany). A single experiment lasted for 20 h during which spectra were recorded every 15 min.

X-ray diffraction (XRD)

X-ray diffraction patterns were measured using a Bruker D8 Advance θ-θ diffractometer (CuKα radiation generated at 40 mA and 40 kV) with a variable divergence slit width set to 12 mm sample length and a receiving slit width of 0.2 mm. The Rietveld program BGMN (Bergmann and Kleeberg, 1998) was used to determine the quantitative mineralogical composition of non-oriented powder samples (<2 μm). All samples were analyzed from 2 to 92º2θ with a measuring time of 3 s per step.

X-ray photoelectron spectroscopy (XPS)

XPS was chosen in order to check for a possible change of the internal chemical structure after steam treatment. Specimens were prepared as films from a 1 wt.% dispersion of <2 μm Volclay-Na, BeC-Ca, BeD-Mg, and BeH-K in deionized water. Aliquots of the dispersion were withdrawn using a pipette and distributed carefully over a petrographic microscope glass slide. After evaporation of residual water the specimens were dried at 200ºC and kept in a desiccator until analysis.

Angle-resolved XPS measurements of Volclay-Na were carried out on a Thermo Theta Probe spectrometer (Thermo Fisher Scientific, USA). The incident beam consisted of monochromatic AlKα radiation with a photon energy of E = 1486.6 eV. Step width and spot size were defined as 0.1 eV and 400 μm, respectively. In the case of Al_{2p} and Si_{2p} measurements, dwell time was set at 200 ms and 400 scans were performed for each angle. The O_{1s} line was recorded with a dwell time of 100 ms and 10 scans per angle.

Further angle-resolved XPS measurements of BeC-Ca, BeD-Mg, and BeH-K were carried out on an XPS/AES/UPS-system by PREVAC sp. z o.o. (Poland) with a Hemispherical Analyzer R4000 from VG Scienta Ltd. (UK). The incident beam consisted of non-monochromatic AlKα radiation. All lines of Al_{2p}, Si_{2p}, O_{1s}, and C_{1s} were recorded at five scans per angle. Step width and dwell time per step were defined as 0.05 eV and 100 ms, respectively; the pass energy of the analyzer was fixed at 100 eV.

The angle of the incident beam was either 38º or 68º, measured against the vertical direction. During all experiments a flood-gun was used for charge compensation.

RESULTS

XRD

Bentonites C−W (<2 μm fraction) are almost pure smectites, with a very small anatase content (<1%). Volclay consists of smectite (91%), halite (7%), and quartz (2%); Namorit-S consists of smectite (93%), kaolinite (6%), and anatase (<1%). No changes in peak positions were observed after steaming. The lattice constant b, which is sensitive especially to Fe contents in octahedral sites, did not change after the treatment (Heuser *et al.*, 2013). Minor differences in peak intensities between untreated and treated samples were observed for the (001) reflection of smectite (Figure 2). These differences are assumed to result from sample preparation (texturing) and are, therefore, considered insignificant.

The comparison of peak positions of different samples is possible because humidity and storage time were the same for untreated and treated samples. After drying at 200ºC, the samples were stored in PVC containers and measured with XRD after 1−2 weeks. The XRD measurements took ~8 h, during which the samples were exposed to room temperature and humidity. However, this time period would be sufficient to create similar hydration states for untreated and treated samples.

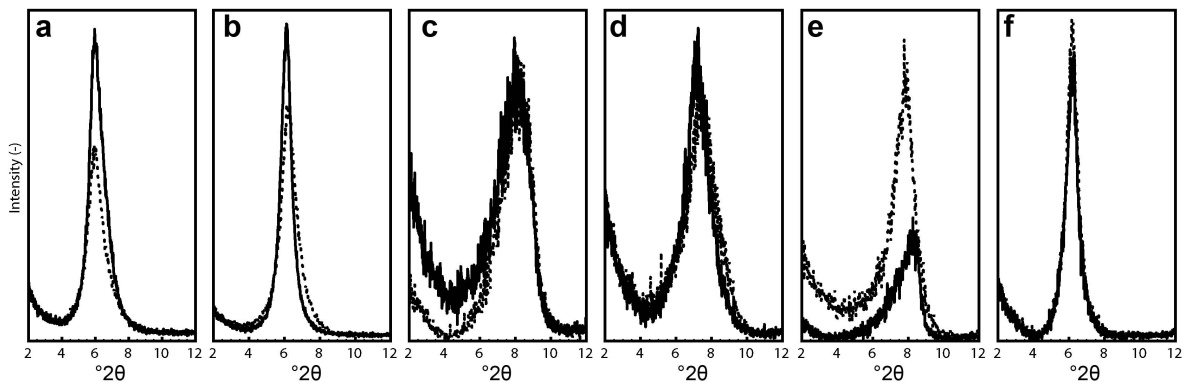

Figure 2. (001) reflection of smectite: (a) bentonite D-Ca; (b) bentonite D-Mg; (c) bentonite D-K; (d) bentonite D-Na; (e) Voclay-Na; and (f) Namorit S-Mg. The solid line represents the untreated sample, the dotted line the steam-treated sample.

Table 2. Si concentration in the supernatant water after the treatment and in 1 g of sample material dispensed in 20 mL of deionized water after filtration (0.45 μm filter).

Si (mg/L)	Supernatant water after treatment	1 g of untreated material dispersed in 20 mL of deionized water
Deionized water	0.085	–
Namorit S	4.742	31.26
BeH-Ca	0.492	9.704
Volclay	5.766	35.42

Ionic inventory

In all samples, lithium, cesium, and calcium, as well as bromide, nitrite, and phosphate, were below the ion chromatography detection limit of 0.5 mg/L (Table 1). In general, all concentrations were in the lower mg/L range. Differences between the four samples can be assigned to measurement uncertainties and a low contamination by PTFE inlets of the autoclaves as shown by test #2.

The Al concentrations in the blank samples and the steam-treated supernatant did not exceed the concentrations found in untreated deionized water. For Si, the steam treatment consistently reduced the concentrations relative to those of the dispersions made from untreated samples (Table 2).

Colorimetry

Color measurements confirmed the visual impression, which did not reveal any differences between untreated and treated smectites.

Sedimentation volume

The sedimentation volume (SV) represents the maximum volume captured by unconfined clay in suspension after a fixed time. The influence of water vapor on the sedimentation volume of montmorillonite depends on the temperature of the vapor and the moisture in the system. In order to verify these results, the specific volume of selected untreated and steam-treated samples was quantified. Sedimentation volumes of treated samples were always smaller than those of treated samples, which was ascribed to a change in swelling capacity of smectite (Oscarson and Dixon, 1989). A linear relationship between untreated and treated samples was found (Figure 3), although with a low correlation factor of $R^2 = 0.66$.

Water adsorption

Water adsorption varies substantially as a function of the interlayer cations of smectite (*e.g.* Montes-H. *et al.*, 2003; Montes-H. and Geraud, 2004). Moreover, a clear

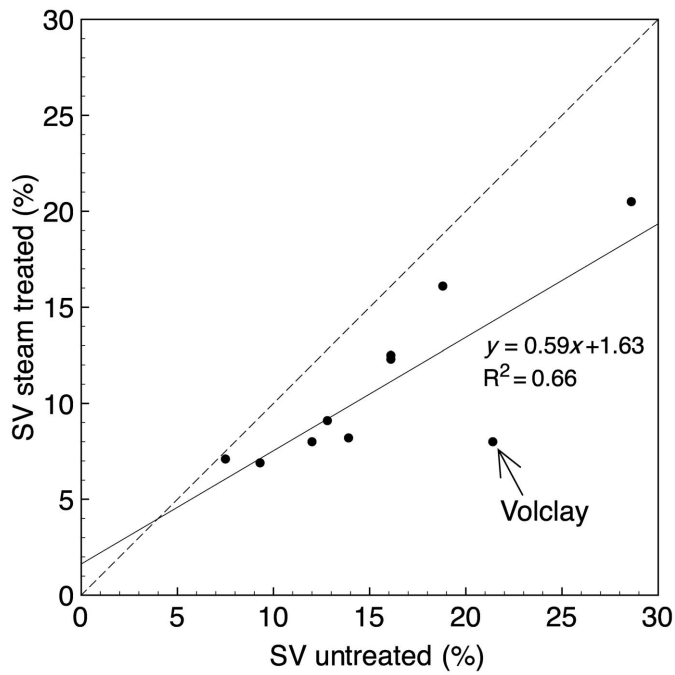

Figure 3. Sedimentation volume (SV) of selected samples after 1 day of sedimentation: results are presented as percentages of the initial volume (56 mL). Dotted line: $y = x$; full line: linear regression (see text for explanation).

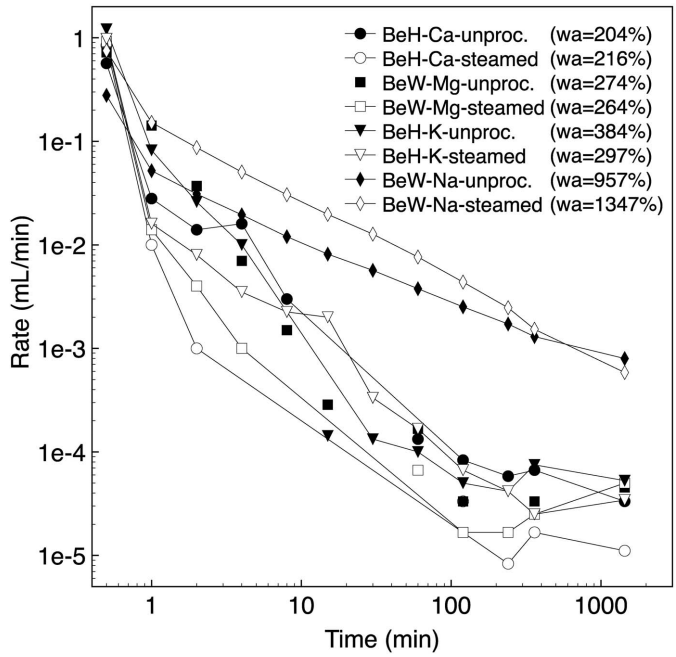

Figure 4. Rates of water adsorption *vs.* time of selected samples and interlayer cations. The values in parentheses represent the water adsorption (wa, %) after 24 h.

distinction between monovalent and divalent interlayer cations was observed. Due to changes in the width of the filling area on the filter plate of the experimental equipment and the dependence of water adsorption on the interlayer cation of smectite, samples adsorbed different amounts of water at the beginning of the experiments (Figure 4). With increasing time, the water adsorption of treated and untreated samples differed by more than the experimental error of 2.5% (Dieng, 2005). Differences in water adsorption between untreated and treated samples (Figure 4, values in parentheses) are significant, therefore. In contrast, water-adsorption rates showed differences at the beginning of the test only. After 30−60 min, the rates of adsorption by untreated and treated samples were identical within uncertainty and converged rapidly toward zero.

Cation exchange capacity

The CEC of some samples decreased while for others it remained unchanged after the steam treatment. The CEC values of untreated and treated samples did not correlate with each other (Figure 5). Furthermore, the kind of smectite had no influence on the CEC, but the interlayer cation of the smectite did (Figure 5a,b). Samples saturated with divalent cations showed little or no change in CEC, whereas samples with monovalent cations reacted to steaming. For most of the samples, the CEC values of K-smectites plot below the CEC values of Na-smectites (Figure 5b). The pH of clay dispersions for the CuTrien-method was approximately equal for all untreated and treated samples and ranged between pH 6 and 7.

Equivalent sphere diameter

Sodium-exchanged smectites had smaller ESD values than smectites exchanged with other cations. Aggregation during oven drying after steaming and destruction of aggregates during sonication of particles in water could explain the scattering of ESD measurements above and below the 1:1 line. The treatment itself, however, did not lead to any systematic trend. Neither the variety of smectite (Figure 6a) nor the variety of interlayer cation (Figure 6b) provided a distinction.

Methylene blue absorption

The spectra of methylene sorption experiments showed band positions at 577±4, 614±9, 675±6, and 768±4 nm (Figure 7), which changed both with time and with interlayer cation. The vapor treatment had no noticeable effect on the band positions. The intensity of the bands, however, depended heavily on the type of interlayer cation (Czímerová *et al.*, 2004), especially in terms of the number of bands and their positions. Samples with a divalent cation in the interlayer space (Figure 7a, b, f) showed only one characteristic band at 577±4 nm. On the other hand, samples with a monovalent interlayer cation (Figure 7c, d, e) showed minor differences in intensities after steaming, but no shift in position. The pure methylene blue solution showed two characteristic bands at 616 nm and 668 nm. Both bands are clearly visible within the spectra of monovalent interlayer cations after 30 min as well as after 1200 min. In contrast, spectra of samples with a divalent cation in the interlayer only show remains of the two methylene blue peaks. Sorption rates of methylene blue for

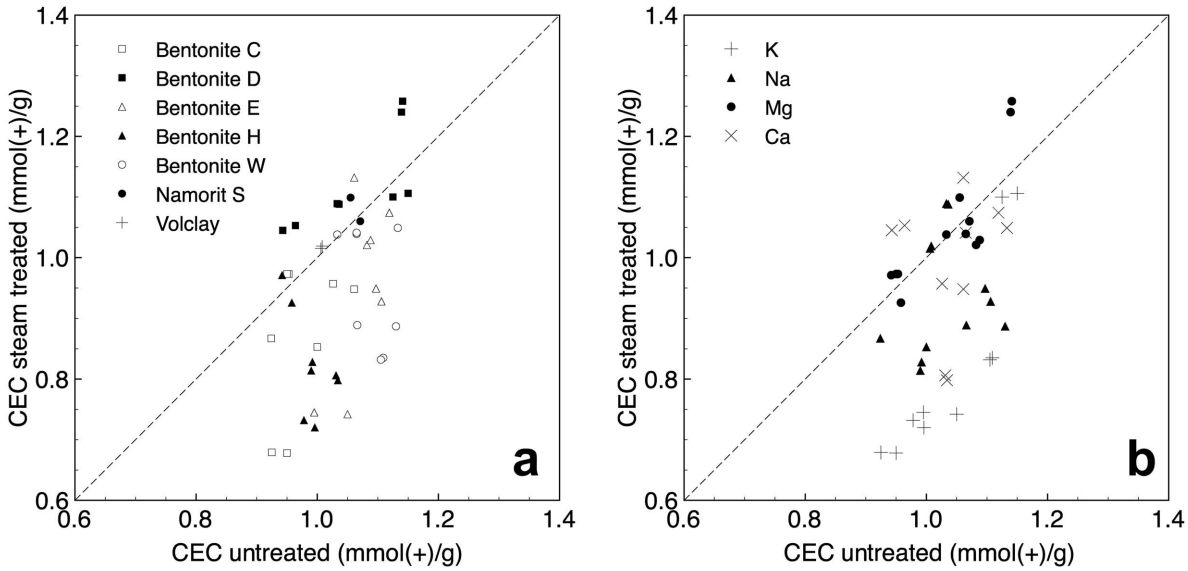

Figure 5. Comparison between the CEC of untreated and steam-treated smectites, sorted by bentonite species (a) and interlayer cation (b).

monovalent cations were almost instantaneous, whereas for divalent cations it took 5−10 min before equilibrium was reached.

XPS

The XPS peaks of Volclay-Na were fitted, after a linear background subtraction, by Gaussian peak-profiles using *Fityk* (Wojdyr, 2010). Unfortunately, no reference line was measured here which makes quantification and direct comparison of binding energies impossible. Nonetheless, qualitative information regarding differences between samples can be obtained by comparing distances between peak centers of species A and B, Δ(AB), according to equation 3:

$$\Delta(AB) = (\text{center}_A - \text{center}_B)_{\text{treated}} - (\text{center}_A - \text{center}_B)_{\text{untreated}} \quad (3)$$

Differences in binding energies, Δ(AB), as calculated from equation 3, are, in all cases, <0.07 eV.

After a linear subtraction of a Shirley background, XPS peaks of BeC-Ca, BeD-Mg, and BeH-K were fitted by Gaussian/Lorentz peak-profiles using *CasaXPS* (Fairley, 2009) and the characteristic peak parameters obtained from all fits were listed (Table 3).

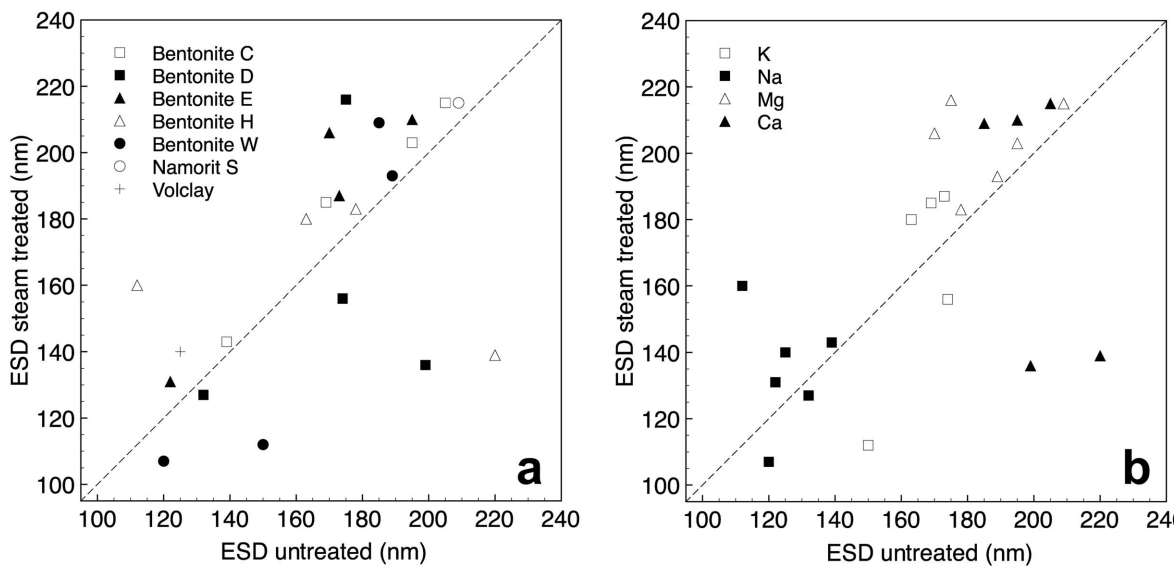

Figure 6. Comparison between ESD values of untreated and steam-treated smectites, sorted by bentonite species (a) and by interlayer cation (b).

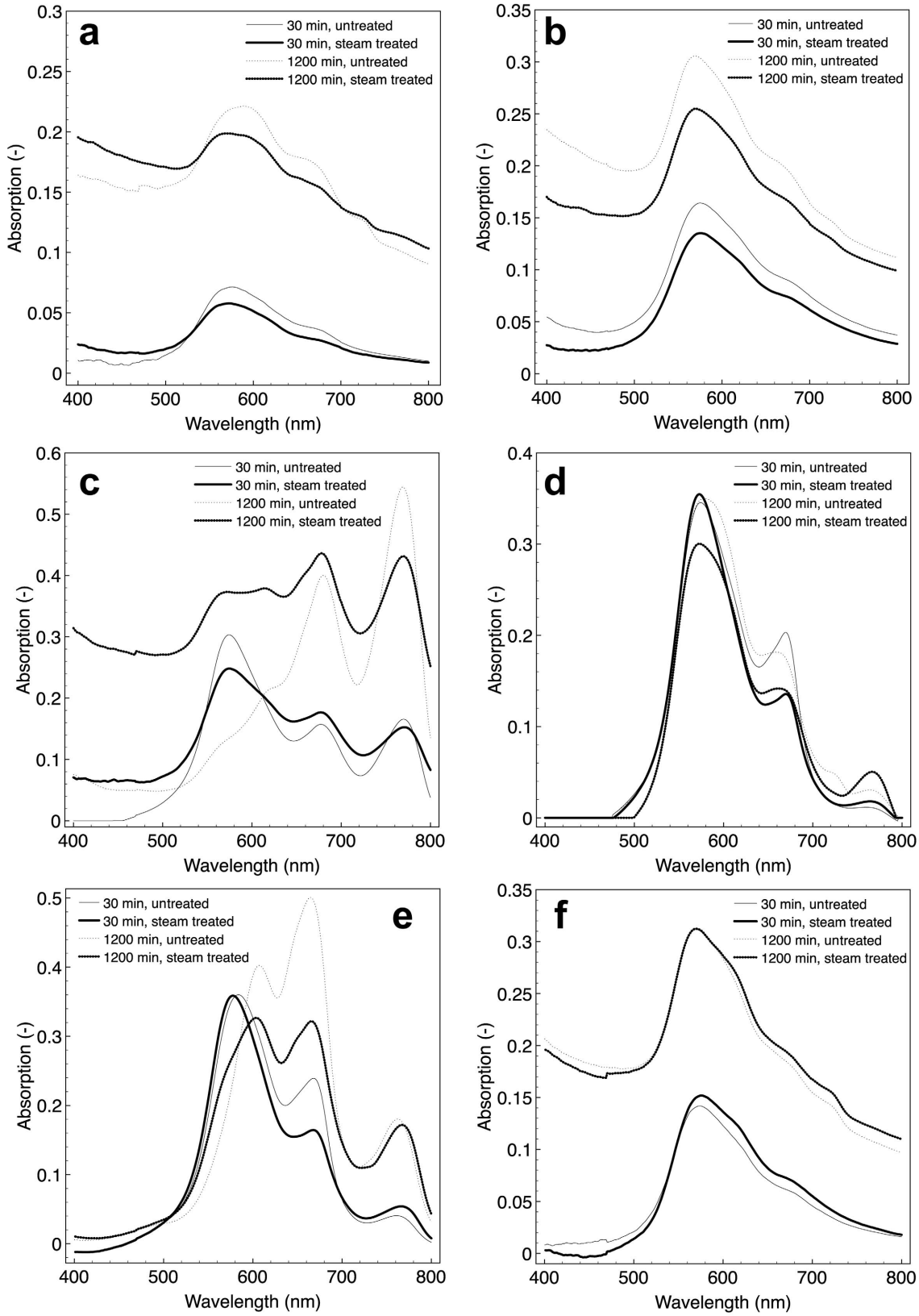

Figure 7. Methylene blue spectra of bentonite D: (a) -Ca, (b) -Mg, (c) -K, (d) –Na, (e) -Volclay-Na, and (f) -Namorit S-Mg, 30 min and 1200 min after the start of the experiment.

Table 3. Characteristic peak parameters of fitted XPS peaks at working angles of 38º and 68º for untreated and steam-treated samples.

Volclay-Na	38º			68º		
Untreated	Al_{2p}	Si_{2p}	O_{1s}	Al_{2p}	Si_{2p}	O_{1s}
Center [eV]	74.2	102.4	531.7	74.2	102.3	531.6
Height [cps]	120.17	455.12	2718.16	58.63	232.72	1585.25
FWHM [eV]	1.65	1.78	1.94	1.68	1.81	1.97
Treated	Al_{2p}	Si_{2p}	O_{1s}	Al_{2p}	Si_{2p}	O_{1s}
Center [eV]	74.4	102.6	531.9	74.4	102.5	531.9
Height [cps]	107.89	417.95	2507.06	54.44	218.93	1504.50
FWHM [eV]	1.94	2.02	2.18	1.96	2.04	2.22
BeC-Ca	38º			68º		
Untreated	Al_{2p}	Si_{2p}	O_{1s}	Al_{2p}	Si_{2p}	O_{1s}
Center [eV]	74.4	102.5	531.7	74.3	102.4	531.6
Height [cps]	69721	191144	922851	63722	172170	775608
FWHM [eV]	1.98	2.21	2.39	1.94	2.11	2.38
Treated	Al_{2p}	Si_{2p}	O_{1s}	Al_{2p}	Si_{2p}	O_{1s}
Center [eV]	74.4	102.6	531.7	74.4	102.6	531.6
Height [cps]	64580	156029	688327	54307	130362	569123
FWHM [eV]	2.26	2.57	3.05	2.67	2.77	3.06
BeD-Mg	38º			68º		
Untreated	Al_{2p}	Si_{2p}	O_{1s}	Al_{2p}	Si_{2p}	O_{1s}
Center [eV]	74.4	102.5	531.6	74.3	102.4	531.5
Height [cps]	65972	178281	812361	54070	137681	585774
FWHM [eV]	2.07	2.26	2.53	2.35	2.46	2.73
Treated	Al_{2p}	Si_{2p}	O_{1s}	Al_{2p}	Si_{2p}	O_{1s}
Center [eV]	74.2	102.3	531.5	74.2	102.3	531.3
Height [cps]	68431	181651	844522	58304	147363	625588
FWHM [eV]	2.30	2.52	2.79	2.66	2.58	3.08
BeH-K	38º			68º		
Untreated	Al_{2p}	Si_{2p}	O_{1s}	Al_{2p}	Si_{2p}	O_{1s}
Center [eV]	74.2	102.4	531.5	74.0	102.3	531.4
Height [cps]	75735	218156	1246495	46541	122185	522195
FWHM [eV]	2.02	2.13	2.37	2.22	2.46	2.67
Treated	Al_{2p}	Si_{2p}	O_{1s}	Al_{2p}	Si_{2p}	O_{1s}
Center [eV]	74.2	102.5	531.5	74.1	102.3	531.4
Height [cps]	64896	148288	730853	60044	166322	794525
FWHM [eV]	2.02	2.12	2.43	2.05	2.33	2.48

For these measurements, Carbon C1s at 284.6 eV was used as a reference for a direct comparison of binding energies. After calibration of all binding energies in relation to this reference, the deviation of binding energies was no more than ±0.1 eV.

As the precision of binding-energy determination is generally estimated to be 0.1 eV (Canesson, 1982; Paterson and Swaffield, 1994), the rather small shifts in peak positions are interpreted to be insignificant. From these results the steam treatment is interpreted not to have altered the binding energy of the species investigated.

DISCUSSION

Several laboratory tests were performed to demonstrate and to quantify the influence of hot water steam on

smectite. Most of the experiments showed no systematic trend between vapor-treated and untreated samples. In contrast, samples subjected to water adsorption, CEC, sedimentation volume, and methylene blue sorption did respond to the treatment.

The effects of steaming were generally influenced little if at all by the bentonite or clay type, whereas the interlayer cation of the smectite clearly had an influence in the case of hot water vapor. Moreover, a distinction between monovalent and divalent cations seems to be clearly visible in most of the tests.

As previously shown by Bish *et al.* (1997) and Madsen (1998), the XRD measurements revealed no differences between untreated and treated samples. The peak positions of different mineral phases remained unaffected by the steam treatment; minor changes in peak intensity can be explained easily by slight changes in particle orientation, packing density and instrumental conditions affecting absolute intensities. The mineralogical composition of samples (XRD) and the chemical environment of the species investigated (XPS) did not change due to the steam treatment.

Based on ^{27}Al NMR results, Bish *et al.* (1997) speculated about an attack on the octahedral sheet, resulting in a reduced proportion of octahedral Al after steam treatment. Regarding the disposition of octahedral Al, the authors assumed it to have relocated at the surface of the smectite particles. A relocation of the octahedral species seems unlikely in view of our XPS results. Such an attack-relocation mechanism would be detectable by XPS because the chemical environment of the element would change and so shift the band energies. The latter was not observed here. Note, however, that most of the peaks of the unprocessed sample show a smaller FWHM than peaks of the treated sample (Table 3). The FWHM values were interpreted in terms of crystallinity by Ebina *et al.* (1997) who reported decreasing FWHM with increasing crystallinity. A dependence of the FWHM of the O_{1s} and Al_{2p} peaks on the crystallinity of a given sample was also predicted by Mosser *et al.* (1992). Mapping these findings to the present situation implies that the treated samples are less crystalline than the untreated ones.

Based on the result that the chemistry and crystal structure of the samples were unchanged, only the surface characteristics of the particle could explain the differences observed. Phase transitions or structural transformations of the minerals present are unlikely, therefore.

The decreased sedimentation volume depended on temperature and, to a lesser extent, on moisture according to Oscarson and Dixon (1989) who related this effect to a decreased swelling capacity after steaming. The modification of SV and swelling capacity appeared at temperatures of 110ºC and increased with increasing temperature. The SV in the present study, however, was only measured after a 200ºC steam treatment but resulted in a decrease in SV also. As known, changes in SV are related to different electrokinetic charge properties at the particle surface, an aspect which will be discussed further in part II of this study.

In contrast to the findings of Oscarson and Dixon (1989) but in agreement with the results of Madsen (1998), the CEC values of K- and Na-smectites decreased by as much as 30% after the steam treatment, whereas the Mg- and Ca-smectites were identical, within a 10% error range (according to the findings of Dohrmann *et al.*, 2012). Theoretically, an isochemical growth of smectite particles should change the proportion of exchange sites stemming from the permanent layer charge relative to the variable charge sites on the *hk*0 faces. Hence, samples which show no particle growth should also show no changes in CEC. No systematic correlation was found between the change in CEC and the change in ESD. Neither does a direct comparison between ESD and CEC lead to a correlation.

The concentrations of the clay–water dispersion for the methylene blue (MB) spectra were identical for treated and untreated samples. Assuming that the density and diameter of the clay particles remained unchanged due to the treatment, the absolute clay surface available for methylene blue sorption is approximately equal for both treated and untreated samples. For this reason, the sorption kinetics of treated and untreated samples should be similar (Figure 7), which is true in terms of band positions but not in terms of absorption intensities. The kind of interlayer cation could be derived from the number of peaks and their positions and agreed with the results of Czímerová *et al.* (2004). The four band positions observed are related to the four different forms of MB in clay dispersion: larger or higher agglomerates: $(MB^+)_n$ – 577±4 nm, dimers: $(MB^+)_2$ – 614±9 nm, monomers: MB^+ – 675±6 nm, and the protonated form: MBH^{2+} or J-aggregates – 768±4 nm (Bujdák *et al.*, 2001). Changes in absorption intensity could probably be assigned to variations in layer charge for bands near 675±6 and 768±4 nm and charge density for the band near 577±4 nm (Bujdák *et al.*, 1998; Bujdák *et al.*, 2001). As previously indicated by CEC measurements and confirmed by MB spectra, the charge conditions of samples with a divalent interlayer cation remained unaffected, whereas samples with a monovalent cation showed a decrease in CEC and also a change in the MB spectra. These qualitative differences between mono- and divalent-loaded smectites are indicated by the results of time-dependent VIS spectra of methylene blue–clay interaction.

The ESD was expected to increase after the steam treatment. Dissolution and recrystallization processes in terms of Ostwald ripening (Eberl *et al.*, 1990) could occur due to enhanced temperature and pressure conditions in the autoclaves. The hydrothermal alteration of bentonite as a buffer material in nuclear-waste reposi-

tories led to particle growth of clay particles (Pusch and Kasbohm, 2002). Another process that also leads to change in particle size is aggregation. Physical particle aggregation in partially saturated and heated clays might contribute to the decrease in swelling capacity (Oscarson and Dixon, 1989). In contrast to the findings of Pusch and Kasbohm (2002) and Oscarson and Dixon (1989), no systematic increase in the ESD upon hot-vapor treatment was found, possibly because the treatment times were insufficient or the temperatures not high enough. The effects of particle growth and particle aggregation could not be confirmed, therefore, under the experimental conditions in the present study.

From the water-adsorption measurements, two results are available: an absolute value after 24 h and rates for the water adsorption (Figure 4). To transfer the laboratory results into application in foundry technology and casting, only the rates of water adsorption are really important. Absolute values after 24 h are of little interest in terms of molding-sand preparation and regeneration because the time necessary for one casting cycle in serial production in a foundry is <<24 h (Grefhorst *et al.*, 2005). The absolute water adsorption or water-uptake capacity as well as the rate of water adsorption showed no clear difference between treated or untreated samples. The water-adsorption process depends on relative humidity, the interlayer cation, and on the amount of sample (Montes-H. and Geraud, 2004). Mechanical compaction of the sample plays a minor role and the drying temperature is irrelevant in terms of water adsorption. The relative humidity, amount of sample, drying temperature, and mechanical compaction were equal for both the untreated and treated samples. The influence of different interlayer cations on water adsorption was of great interest, however. As expected from Montes-H. *et al.* (2003), Montes-H. and Geraud (2004), and Kaufhold *et al.* (2010), the Na-loaded samples showed very high water-uptake capacities compared to those with a divalent interlayer cation. Samples saturated with Mg^{2+} and Ca^{2+} showed approximately equal amounts and rates, which agrees with the results of Montes-H. and Geraud (2004). As shown by Dontsova *et al.* (2004), the smaller and even more hydrated cations (Na^{+} and Mg^{2+}) lead to greater water sorption by the smectite than those with larger cations (K^{+} and Ca^{2+}). The amount of water adsorbed as well as the rates of adsorption were influenced by the interlayer cations in the order: $Na^{+} > K^{+} > Mg^{2+} > Ca^{2+}$ (Figure 4). The order of adsorption, depending on interlayer cation, varies from study to study (*i.e.* Montes-H. and Geraud, 2004; Dontsova *et al.*, 2004). A comparison of values from the present study with those of other studies is difficult, therefore. The correlation between CEC and water adsorption, as shown by Kaufhold *et al.* (2010), was not observed. After 30–60 min, however, the rates of water adsorption were equal and converged to zero (Figure 4) independent of sample, interlayer cation, and whether untreated/treated. Most of the water adsorbed had been taken up in the first minutes of the experiment, therefore, leading to the conclusion that the water adsorption has little or no influence on the molding-sand regeneration process or quality.

Unlike Al, increased Si concentrations in samples after the steam treatment were measured. Similar results, due to a hydrothermal treatment on MX-80 bentonite, were noted by Pusch (2000). During cooling of the samples after a hydrothermal treatment, silica from the surfaces of the clay particles was precipitated. This process caused superficial dissolution of smectite and accessory silicates and led to cementation and particle aggregation (Pusch, 2000) and might explain the increased Si concentrations.

In comparison to the Si concentrations measured in the blank experiments (1 g of sample immersed in 20 mL of water for 5 days), the concentrations of Si after steam treatment were rather low, however (see Table 2). This can be explained by noting that the transport of ionic species is more effective in a liquid medium than in a gaseous phase. In order to check if the measured Si concentrations in the blank experiments can be ascribed to the dissolution of smectite, the blank experiment of BeH Ca was modeled using *PhreeqC* (Parkhurst and Appelo, 1999) at pH 7. The calculated Si concentration is smaller than the measured concentration by a factor of six. Changing the pH to five does not affect this factor. These results suggest that the measured aqueous Si concentrations cannot be ascribed to the dissolution of smectite alone. Similar conclusions were reached by Baeyens and Bradbury (1997) who suggested that aqueous Si concentrations were controlled by the dissolution of quartz at circumneutral pH. Another potential source of Si is volcanic glasses altered during the alteration of the bentonites (Klinkenberg *et al.*, 2009). As volcanic glasses are amorphous, the recalculation of small amounts based on XRD analyses may not be possible. The suggestion that measured aqueous Si concentrations are not due to the dissolution of smectite is in accord with the observation that no structural changes took place due to the steam treatment.

Finally, changes in parameters (ESD, CEC, SV, and WA) showing differences between untreated and steam-treated samples is discussed. The parameters plotted show no correlation with each other and so no relation between them, measured or calculated, exists.

CONCLUSION AND FUTURE WORK

From the variety of comparative experiments performed, few revealed differences between untreated and steam-treated samples. On the basis of XRD and XPS results, steam treatment does not affect the internal structure of the minerals.

The reduced sedimentation volume observed for all samples after exposure to water vapor confirms success-

ful steam treatment but did not allow us to identify the processes involved.

The measured changes in CEC are significant only in the case of monovalent interlayer cations, in contrast to the findings of Couture (1985) and Oscarson and Dixon (1989). The fact that CEC values of samples containing divalent interlayer cations do not change (within a 10% error margin) cannot be explained at present and requires further investigation. These differences between monovalent- and divalent-loaded smectites are also indicated by the results of time-dependent VIS spectra of methylene blue−clay interaction.

Realizing that sedimentation volume (see chapters 2 and 9 of Kruyt, 1952, for example) and CEC are influenced by the electrokinetic charge density and the surface-charge density, respectively, suggests that the differences observed in the present study are due to changes in the charge distribution at the surface of the minerals. This idea is in qualitative agreement with zeta potentials reported by Bish *et al.* (1997).

The likely negative influence of water vapor on the quality of the molding sand and on the sand-regeneration process could be due to the aforementioned results, but are not fully confirmed. Further experiments presented in part II of this study will include conductometric titrations as well as the determination of zeta potentials or electrophoretic mobilities as a function of pH. Furthermore, rheological measurements, which could be related directly to modifications in electrokinetic properties and changes in particle shape computed from conductometric titrations in particular (Dukhin and Derjaguin, 1974), will also be performed.

ACKNOWLEDGMENTS

The present research was funded within the special program 'Geotechnologien' (grant # 03G0707A) of the German Federal Ministry of Education and Research (BMBF). The authors thank S & B Industrial Minerals for supplying the bentonites and the Department of Engineering Geology and Hydrogeology RWTH for the opportunity to measure water adsorption. Finally, the authors thank the anonymous reviewers for their helpful comments and suggestions which improved the manuscript.

REFERENCES

Anthony, J.W., Bideaux, R.A., Bladh, K.W., and Nichols, M.C. (2013) *Handbook of Mineralogy*. Mineralogical Society of America, Chantilly, VA 20151-1110, USA. http://www.handbookofmineralogy.org/.

Ashmawy, A.K., El-Hajji, D., Sotelo, N., and Muhammad, N. (2002) Hydraulic performance of untreated and polymer-treated bentonite in inorganic landfill leachates. *Clays and Clay Minerals*, **50**, 546−552.

Baeyens, B. and Bradbury, M.H. (1997) A mechanistic description of Ni and Zn sorption on Na-montmorillonite. Part I: Titration and sorption measurements. *Journal of Contaminant Hydrology*, **27**, 199−222.

Baier, J. (1991) Griechischer Bentonit für Gießereien. *Giesserei*, **78**, 501−506.

Beeley, P. (2001) *Foundry Technology*. Butterworth-Heinemann, London, 719 pp.

Berghof (2012) Homepage of the Berghof company, http://www.berghof.com, visited on 15.01.2012.

Bergmann, J. and Kleeberg, R. (1998) Rietveld analysis of disordered layer silicates. *Materials Science Forum*, **278-2**, 300−305.

Bish, D.L., Wu, W., Carey, J.W., Costanzo, P., Giese, R.F., Earl, W., and Oss, C.J. (1997) Effects of steam on the surface properties of Na-smectite. *Proceedings of the 11th International Clay Conference: Clays for our Future*, Ottawa, pp. 569−575.

Bujdák, J., Janek, M., Madejová, J., and Komadel, P. (1998) Influence of the layer charge density of smectites on the interaction with methylene blue. *Journal of the Chemical Society, Faraday Transactions*, **94**, 3487−3492.

Bujdák, J., Janek, M., Madejová, J., and Komadel, P. (2001) Methylene blue interactions with reduced-charge smectites. *Clays and Clay Minerals*, **49**, 244−254.

Canesson, P. (1982) E.S.C.A. studies of clay minerals. Pp. 211−236 in: *Advanced Techniques for Clay Mineral Analysis* (J. Fripiat, editor). Developments in Sedimentology, **34**, Elsevier, Amsterdam.

Christidis, G.E. and Huff, W.D. (2009) Geological aspect and genesis of bentonites. *Elements*, **5**, 93−98.

Couture, R.A. (1985a) Steam rapidly reduces the swelling capacity of bentonite. *Nature*, **318**, 50−52.

Couture, R.A. (1985b) Rapid increases in permeability and porosity of bentonite-sand mixtures due to alteration by water vapor. *Materials Research Society Symposia Proceedings*, **44**, 515−522.

Czímerová, A., Jankovic, L., and Bujdák, J. (2004) Effect of exchangeable cations on the spectral properties of methylene blue in clay dispersions. *Journal of Colloid and Interface Science*, **274**, 126−132.

Dieng, M.A. (2005) Der Wasseraufnahmeversuch nach DIN 18132 in einem neu entwickelten Gerät. *Bautechnik*, **82**, 28−32.

DIN 6174 Farbmetrische Bestimmung von Farbmaβzahlen und Farbabständen im angenähert gleichförmigen CIELAB-Farbenraum. Ausgabe DIN 6174:2007-10.

Dohrmann, R., Genske, D., Karnland, O., Kaufhold, S., Kiviranta, L., Olsson, S., Plötze, M., Sandén, T., Sellin, P., Svensson, D., and Valter, M. (2012) Interlaboratory CEC and exchangeable cation study of bentonite buffer materials: I. Cu(II)-Triethylenentetramine method. C*lays and Clay Minerals*, **60**, 162−175.

Dontsova, K.M., Norton, D.L., Johnston, C.T., and Bigham, J.M. (2004) Influence of exchangeable cations on water adsorption by soil clays. *Soil Science Society of America Journal*, **68**, 1218−1227.

Dukhin, S.S. and Derjaguin, B.V. (1974) Equilibrium double layer and electrokinetic phenomena. Pp. 49−272 in: *Surface and Colloid Science* (E. Matijevic, editor). John Wiley & Sons, New York.

Eberl, D.D., Środoń, J., Kralik, M., Taylor, B.E., and Peterman, Z.E. (1990) Ostwald ripening of clays and metamorphic minerals. *Science*, **248**, 474−477.

Ebina, T., Iwasaki, T., Chatterjee, A., Katagiri, M., and Stucky, G.D. (1997) Comparative study of XPS and DFT with reference to the distributions of Al in tetrahedral and octahedral sheets of phyllosilicates. *Journal of Physical Chemistry B*, **101**, 1125−1129.

Erdoğan, B. and Demirci, Ş. (1996) Activation of some Turkish bentonites to improve their drilling fluid properties. *Applied Clay Science*, **10**, 401−410.

EUBA (European Bentonite Association) (2006) Position Paper, 10/2006, http://www.ima-europe.eu/sites/ima-europe.eu/files/publications/Bentonite_An-WEB-2011.pdf.

Fahrenholtz, W.G. (2008) Clays. Pp. 111–133 in: *Ceramic and Glass Materials: Structure, Properties and Processing* (J.F. Shackelford and R.H. Doremus, editors). Springer, Berlin.

Fairley, N. (2009) CasaXPS Manual – 2.3.15 Introduction to XPS and AES. Casa Software Ltd., 177p.

Gitipour, S., Bowers, M.T., and Bodocsi, A. (1997) The use of modified bentonite for removal of aromatic organics from contaminated soil. *Journal of Colloid and Interface Science*, **196**, 191–198.

Grefhorst, C. (2006) Prüfung von Bentoniten – Ausführliche Bewertung der Eigenschaften und ihr Wert für die Praxis. *Giesserei*, **93**, 26–31.

Grefhorst, C., Podobed, O., and Böhnke, S. (2005) Bentonitgebundene Formstoffe – Umlaufverhalten von Bentoniten unter besonderer Betrachtung des Kreislaufsystems und der Nasszugfestigkeit. *Giesserei*, **92**, 63–67.

Grim, R.G. and Güven, N. (1978) *Bentonites – Geology, Mineralogy, Properties and Uses*. Developments in Sedimentology **24**, Elsevier, Amsterdam.

Güven, N. (1990) Longevity of bentonite as buffer material in a nuclear-waste repository. *Engineering Geology*, **28**, 233–247.

Heuser, M., Andrieux, P., Petit, S., and Stanjek, H. (2013) Iron-bearing smectites: A revised relationship between structural Fe, *b* cell edge lengths and refractive indices. *Clay Minerals*, **48**, 97–103.

Jacobs, K.Y. and Schoonheydt, R.A. (2001) Time dependence of the spectra of methylene blue–clay mineral dispersions. *Langmuir*, **17**, 5150–5155.

Jordan, G., Eulenkamp, C., Calzada, E., Schillinger, B., Hoelzel, M., Gigler, A., Stanjek, H., and Schmahl, W.W. (2013) Quantitative in-situ study on the dehydration of bentonite bonded molding sands. *Clays and Clay Minerals*, **61**, 133–140.

Kahr, G. and Madsen, F.T. (1995) Determination of the cation exchange capacity and the surface area of bentonite, illite and kaolinite by methylene blue adsorption. *Applied Clay Science*, **9**, 327–336.

Kaufhold, S., Dohrmann, R., and Klinkenberg, M. (2010) Water-uptake capacity of bentonites. *Clays and Clay Minerals*, **58**, 37–43.

Klinkenberg, M., Rickertsen, N., Kaufhold, S., Dohrmann, R., and Siegesmund, S. (2009) Abrasivity by bentonite dispersions. *Applied Clay Science*, **46**, 37–42.

Köster, H.M. (1979) *Die chemische Silikatanalyse: Spektralphotometrische, komplexometrische und flammenspektrometrische Analysenmethoden.* Springer, Berlin, 212 pp.

Kruyt, H.R. (1952) *Colloid Science Volume 1 – Irreversible Systems*. Elsevier, Amsterdam.

Lagaly, G., Schulz, O., and Zimehl, R. (1997) *Dispersionen und Emulsionen. Einführung in die Kolloidik feinverteilter Stoffe einschließlich der Tonminerale*. 1st edition, Steinkopff-Verlag Darmstadt, Germany, pp. 285–289.

Lange, H. (1968) Bestimmung von Teilchengrößen aus Trübung und Brechungsinkrement. *Kolloid Zeitschrift und Zeitschrift für Polymere*, **223**, 24–30.

Lange, H. (1969) Bestimmung der Teilchengröße in ABS-Kunststoffen. *Kolloid Zeitschrift und Zeitschrift für Polymere*, **232**, 753–757.

Lange, H. (1995) Comparative test of methods to determine particle size and particle size distribution in the submicron range. *Particle and Particle Systems Characterization*, **12**, 148–157.

Luckham, P.F. and Rossi, S. (1999) The colloidal and rheological properties of bentonite dispersions. *Advances in Colloid and Interface Science*, **82**, 43–92.

Ma, Y.-L., Xu, Z.-R., Guo, T., and You, P. (2004) Adsorption of methylene blue on Cu(II)-exchanged montmorillonite. *Journal of Colloid and Interface Science*, **280**, 283–288.

Madsen, F.T. (1998) Clay mineralogical investigations related to nuclear waste disposal. *Clay Minerals*, **33**, 109–129.

Meier, L.P. and Kahr, G. (1999) Determination of the cation exchange capacity (CEC) of clay minerals using the complexes of copper (II) ion with triethylenetetramine and tetraethylenepentamine. *Clays and Clay Minerals*, **47**, 386–388.

Melik, D.H. and Fogler, H.S. (1983) Turbidimetric determination of particle size distributions of colloidal systems. *Journal of Colloid and Interface Science*, **92**, 161–180.

Mellah, A. and Chegrouche, S. (1997) The removal of zinc from aqueous solutions by natural bentonite. *Water Research*, **31**, 621–629.

Montes-H., G., and Geraud, Y. (2004) Sorption kinetics of water vapour of MX80 bentonite submitted to different physical–chemical and mechanical conditions. *Colloids and Surfaces A: Physicochemical and Engineering Aspects*, **235**, 17–23.

Montes-H., G., Duplay, J., Martinez, L., Geraud, Y., and Rousset-Tournier, B. (2003) Influence of interlayer cations on the water sorption and swelling-shrinkage of MX80 bentonite. *Applied Clay Science*, **23**, 309–321.

Mosser, C., Mosser, A., Romeo, M., Petit, S., and Decarreau, A. (1992) Natural and synthetic copper phyllosilicates studied by XPS. *Clays and Clay Minerals*, **40**, 1125–1129.

Murray, H.H. (2007) *Applied clay mineralogy – Occurrences, Processing and Application of Kaolins, Bentonites, Palygorskite-Sepiolite, and Common Clays*. Developments in Clay Science **2**, Elsevier, Amsterdam.

Neff, K.H. (1959) Über die Messung der Wasseraufnahme ungleichförmiger bindiger anorganischer Bodenarten in einer neuen Ausführung des Enslingerätes. *Die Bautechnik*, **39**, 415–421.

Oscarson, D.W. and Dixon, D.A. (1989) The effect of steam on montmorillonite. *Applied Clay Science*, **4**, 279–292.

Oscarson, D.W., Dixon, D.A., and Gray, M.N. (1990) Swelling capacity and permeability of an unprocessed and a processed bentonitic clay. *Engineering Geology*, **28**, 281–289.

Parkhurst, D.L. and Appelo, C.A.J. (1999) User′s Guide to PHREEQC (Version 2) A Computer Program for Speciation, Batch-Reaction, One-Dimensional Transport, and Inverse Geochemical Calculations. Water-Resources Investigations Report 99-4259, 312 pp. USGS Geological Survey, Denver, Colorado, USA.

Paterson, E. and Swaffield, R. (1994) X-ray photoelectron spectroscopy. Pp. 226–259 in: *Clay Mineralogy: Spectroscopic and Chemical Determinative Methods* (M.J. Wilson, editor). Chapman & Hall, London.

Pusch, R. (2000) On the effect of hot water vapor on MX-80 clay. Technical Report TR-00-16, SKB, 41 pp.

Pusch, R. and Kasbohm, J. (2002) Alteration of MX-80 by hydrothermal treatment under high salt content conditions. Technical Report TR-02-06, SKB, 39 pp.

Recknagel, U. and Dahlmann, M. (2008) Spezialsande-Formgrundstoffe für die moderne Kern- und Formherstellung. Hüttenes-Albertus, Düsseldorf, Germany.

Scalia, J. and Benson, C.H. (2011) Hydraulic conductivity of geosynthetic clay liners exhumed from landfill final covers with composite barriers. *Journal of Geotechnical and Geoenvironmental Engineering*, **137**, 1–13.

Träger, H. and Bührig-Polaczek, A. (2000) Foundry Technology. In: *Ullmann's Encyclopedia of Industrial Chemistry*. Wiley, New Jersey, USA.

Ufer, K., Stanjek, H., Roth, G., Dohrmann, R., Kleeberg, R., and Kaufhold, S. (2008) Quantitative phase analysis of bentonites by the Rietveld method. *Clays and Clay Minerals*, **56**, 272–282.

VDG P35 Prüfung von tongebundenen Formstoffen. Bestimmung des Anteils an bindefähigem Ton. 5 p., Okt. 1999.

Viraraghavan, T. and Alfaro, F. (1996) Adsorption of phenol from wastewater by peat, fly ash and bentonite. *Journal of Hazardous Materials*, **57**, 59–70.

Wojdyr, M. (2010) Fityk: a general-purpose peak fitting program. *Journal of Applied Crystallography*, **43**, 1126–1128.

Zhu, X., Jiang, D., and Tan, S. (2002) Preparation of silicon carbide reticulated porous ceramics. *Materials Science and Engineering A*, **323**, 232–238.

(*Received 9 April 2013; revised 25 July 2014; Ms. 757; AE: K. Emmerich*)

Clays and Clay Minerals, Vol. 62, No. 3, 203–210, 2014.

APPLICATION OF THE DYNAMIC CULTIVATION SYSTEM FOR MICROORGANISMS – A NEW WAY TO CULTURE THE UNCULTURABLES

René Kaden[1,*], Eve Menger-Krug[2], Katja Emmerich[2], Kerstin Petrick[2], and Peter Krolla-Sidenstein[2]

[1] Uppsala University, Department of Medical Sciences, Dag Hammarskjöldsväg 17, 75185 Uppsala, Sweden
[2] Karlsruhe Institute of Technology (KIT), Institute of Functional Interfaces (IFG) Herrmann-von-Helmholtz-Platz 1, 76131 Eggenstein-Leopoldshafen, Germany

Abstract—To date, ~1% of all bacteria that occur in environmental ecosystems such as soil, sedimentary rocks, and groundwater have been described. Comprehensive explanation of ecological interactions on a microscale level is thus almost impossible. The Dynamic Cultivation System (DCS) was developed in order to detect more microbial taxa than with common cultivation approaches, as well as previously undescribed bacterial species. The DCS is a quick and easy *in situ* method for the cultivation of numerous bacterial taxa in support of the description of microbial colonized ecosystems. To investigate the bacterial populations within a clay-maturation process after mining the raw material, the DCS was used to increase the microbial biomass for further molecular analysis. Two different methods were applied to extract the bacteria from the DCS and these were compared in terms of efficiency at detection of large numbers of different taxa and in terms of applicability to the detection of previously undescribed species in raw clays. A collection of different undescribed species was detected with sequencing. While direct picking of bacterial colonies leads to the detection of different genera, species mainly of the genus *Arthobacter* were proved in the phosphate-buffered saline-suspended biomass. Thus, a combination of the approaches mentioned above is recommended to increase the number of detectable species. The DCS will help to describe better the microbial content of ecosystems, especially soils that contain charged particles.

Key Words—Clay, DGGE, DCS, Ecology, Microbial Diversity, Sequencing.

INTRODUCTION

For the ceramics industry, specific properties of clay during processing and firing are necessary in order to obtain a final product of the required quality. Moistened clay is often stored in buildings with high humidity prior to industrial use. This process of clay maturation enhances the properties of the raw material for clay processing in the ceramics industry as well as for the final product quality (Telle, 2007). Thus clay maturation has a significant economic impact in the ceramics industry. On the other hand, the storage of tons of clay for the maturation process requires space which is expensive. The core questions about this procedure are: what are the main processes that cause the known improvements with respect to the plasticity of the clay during storage at high humidity and how could the processes be controlled effectively? Both clay scientists and microbiologists have attempted to answer these questions but to date have been unsuccessful. Microorganisms cause changes in the chemical (*e.g.* pH), biochemical (*e.g.* metabolites), and physical (*e.g.* distribution of water) parameters during clay aging, which lead to the known maturation effect. Knowledge of the maturation process was used centuries ago to produce the robust Chinese egg shell porcelain, which has a wall thickness of <0.4 mm (Weiss, 1963). Microorganisms can cause these changes in material properties. An increase in bacterial and fungal biomass during clay aging was discovered by Glick (1936). Microbial interactions in clay which influenced the clay matrix were also observed by Velde (1995). Organisms interrelate directly with their habitat in ecosystems (Fiore, 2007). The question to be asked is: does the clay-maturation process drive the physical or chemical reactions that influence the composition of the bacterial population composition because of the change in environmental parameters or do the bacteria cause shifts in the ecosystem that lead to the change in the chemical and physical properties? Microorganisms have a direct impact on the properties of clays as they use ions or molecules and release other substances such as exudates, metabolites, or functional complexes, *e.g.* siderophores (Vaiberg *et al.*, 1980; Groudeva and Groudev, 1995). Those compounds are released by bacteria to capture metal ions outside of the organism and might act as lubricants to improve plasticity.

To ascertain the influence of microorganisms on clay maturation, an investigation of the composition of the microbial population is needed. While classical cultivation methods select special groups of bacteria and fungi, extraction of the complete deoxyribonucleic acid (DNA) leads to characterization of all genotypes in general.

* E-mail address of corresponding author:
Rene.Kaden@akademiska.se
DOI: 10.1346/CCMN.2014.0620304

Clays may be able to capture the negatively charged DNA and prevent complete extraction of nucleic acids (Takada-Hoshino and Naoyuki, 2004). Bi- or multivalent cations and humic substances enhance this effect of DNA-binding on clay minerals. Furthermore, DNA extraction from raw materials leads to co-extraction of allochthonous nucleic acids as well as of those of dead organisms. In fact, neither cultivation methods nor complete DNA-extraction methods are able to extract information about the real incidence of all active species in clayey ecosystems.

The purpose of the present study was to provide a new method for the detection of some of the missing 99% of undescribed microbial species that influence clay properties during clay maturation. The method described is used for further analyses of the clay-maturation process. Once the effect of single bacterial species on clay minerals is known, those specific taxa can be used in future for manipulation of nanoparticles.

MATERIALS

For all experiments a silty clay W2, from Westerwald, Germany was used. The W2 clay is applied widely in the ceramics industry. The grain-size distribution was determined with and without Na-pyrophosphate as a dispersant (Table 1).

Table 1. Grain-size distribution with and without dispersant (data from Petrick *et al.*, 2011).

Fraction (μm)	Grain size with dispersant (%)	Grain size without dispersant (%)
>63	3	5
20−63	12	21
2−20	31	31
0.6−2	13	39
<0.6	41	4

The mineralogy was determined by X-ray diffraction (XRD) followed by Rietveld analysis, using SEIFERT *AutoQuan* software (GE Inspection Technologies, Ahrensburg, Germany), of patterns from powdered samples and one-dimensional pattern fitting (ODPF) using *SYBILLA* (Zeelmaekers *et al.*, 2007) of patterns from textured samples to determine the mixed-layer I-S (quartz (46±2%); kaolinite (20±2%); illite (19±2%); R1 I(0.8)-S(11±3%); feldspar (3±1%); rutile (1±1%)).

The kaolinite was distinguished from halloysite by several treatments of the textured samples. A detailed characterization of the material together with detailed description of methods used was given by Petrick *et al.* (2011).

METHODS

Five tons of raw clay (as mined) was homogenized, wetted to a total water content of 15% and divided into buckets containing 20 kg each (Figure 1). The samples were stored in a chamber with a humidity of 60% and a temperature of 21ºC. Beginning at the first day after clay preparation (=t1), samples were analyzed after 3, 6, 9, 13, 16, 20, 27, 41, and 83 days (=t3...t83).

Culturing bacteria and fungi in their original matrix (biol. *in situ*) is a possible means of overcoming the disadvantages of common culture-dependent methods and those of complete DNA extraction. The majority of bacterial species are not culturable with common methods and the analysis of whole genomes of bacterial populations to determine their potential biochemical pathways is difficult and expensive. The charges associated with clay minerals have a negative impact on all molecular analysis (Takada-Hoshino and Naoyuki, 2004). The DCS method (Figure 2), which is clay dependent, was therefore devised

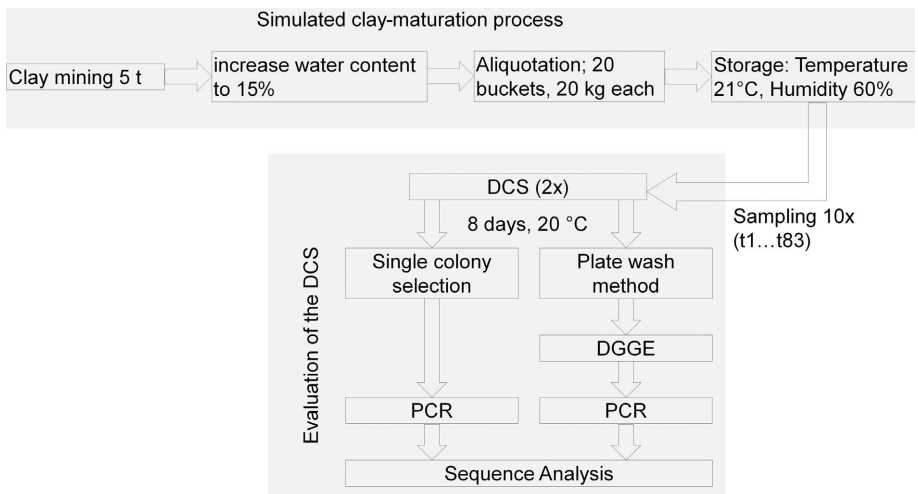

Figure 1. Experiment workflow with a simulated clay-maturation process and DCS evaluation.

(Kaden *et al.*, 2012) as a further development of the diffusion chamber of Bollmann *et al.* (2007).

The main principle of this method is to enrich the bacterial biomass (inoculum) separated from the clay above the incubation system to obtain an almost clay-mineral-free sample for molecular analysis. To separate the clay with a total water content of 30% and the inoculum in the incubation chamber, filters with a pore size of 0.2 µm were applied. Nutrients and water are available for the bacteria from the surrounding clay. A throughput of substances from the clay to the inoculum through the filters occurs due to the gravitational head of the clay-agar below the filter in addition to natural diffusion. The dilution of the sample combined with the enrichment of bacterial biomass during incubation causes a shift in the ratio between bacteria and clay minerals that allows molecular analyses with a reduced impact of inhibiting substances such as charged layer silicates. The main advantages of DCS are the cheap and easy construction and the fact that no external metal ions interact with this artificial but pseudo-natural ecosystem.

The inoculum used in this study was 50 µL of diluted clay slurry, with a solid clay content of 2%, and 98% (w/w) sterile physiological NaCl. The clay at the top of the DCS and the inoculum were taken from the same samples t1 to t83.

Microorganisms grow very slowly in clay due to the oligotrophic characteristic of this matrix. Therefore, the DCS prepared from each matured sample (t1 to t83) in duplicate (Figure 1) was also incubated for 8 days at a temperature of 20ºC. After incubation, the upper filter and the clay above this filter were discarded to collect the cells on the lower filter.

The method for removing the bacteria from the lower filter might have an impact on the detectable species so two procedures within sample analyses were performed to show the differences between them.

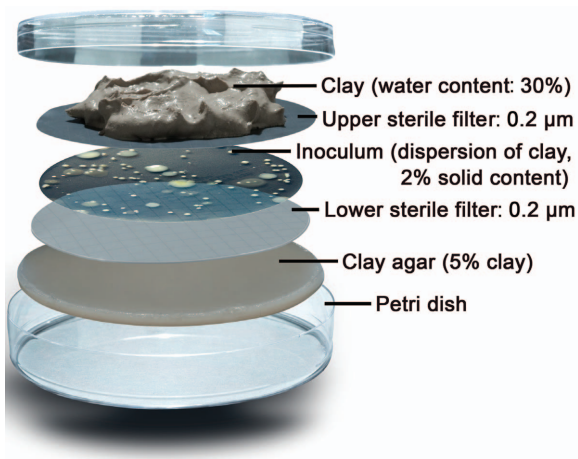

Figure 2. Construction of a DCS for microorganisms (after Kaden *et al.*, 2012).

Method 1. All visible colonies were removed from the lower filter using a sterile toothpick. In many cases, each colony consisted of a single species. Therefore, no further steps for dividing strains for the species determination were required when applying this method. The approach described is straightforward but may lead to an incomplete population analysis. Many bacteria grow in micro-colonies or as translucent biofilm. They are not visible without a microscope and thus it is impossible to remove them with the selection method described.

Method 2. The lower filter was washed with 1 mL of sterile PBS. Furthermore, a cell scraper was used to remove the colonies completely. This method should allow an almost complete molecular screening of all grown species.

The extraction of nucleic acids from the single colonies as well as from the bacterial suspension was performed according the QIAamp DNA Mini Kit manual (QIAGEN, 2003). To increase the amount of DNA for sequencing or for subsequent Denaturing Gradient Gel Electrophoresis (DGGE), a polymerase chain reaction (PCR) was performed using the forward primer 27f (AGAGTTTGATCMTGGCTCAG) (Schuppler *et al.*, 1995) with a GC-clamp that allows an enhanced discrimination of species-specific bands in DGGE (CGCCCGCCGCGCCCCGCGCCCGCTCCGCCGCCG-CCCCCGCCCC) and the reverse primer 517r (ATTACCGCGGCTGCTG) (Gotz *et al.*, 2002). The PCR was performed by enzyme activation for 10 min at 94ºC and 27 cycles of denaturation of DNA for 30 s at 94ºC followed by a primer annealing for 30 s at 58ºC and an elongation for 45 s at 72ºC. The final elongation was for 7 min at 72ºC. The 16S rRNA gene sequences from single picked colonies were determined after the PCR at GATC Biotech in Konstanz, Germany. With 10 µL of the DNA-PBS solution-based PCR products, a DGGE (Fischer and Lerman, 1980) was implemented with a run time ratio of 1000 Vh to divide the DNA at a species-specific level. The vertical urea gradient was 40−60%. The single bands, which represent 16S rRNA gene fragments of a single species, were cut with a sterile scalpel. Same-distanced bands were accepted as the same taxon. In the present case, only one band was chosen for further analysis. The DNA was removed from the gel by diffusion while single slices of the gel were placed into reaction tubes containing PCR water at 8ºC for 12 h. A further PCR was implemented with the same primer set 27f and 517r but without the GC-clamp. The products were sequenced using the primer 27f at GATC Biotech, Konstanz, Germany. The species were determined using the NCBI database (Altschul *et al.*, 1990) and the *blastn* algorithm. For phylogenetic analyses, the *Megalign* 8.0.2 *DNASTAR* software based on Clustal W (Larkin *et al.*, 2007) with the neighbor-joining algorithm was applied.

RESULTS AND DISCUSSION

As most of the single picked colonies were pure cultures, a 16S rRNA gene fragment of these organisms was amplified and sequenced directly without further steps. Within the mixed cultures in the PBS-suspension, a DGGE (Figure 3) was needed to separate the 16S rDNA molecules of the different species. No uniform bar pattern existed through multiple steps in the time series. A few species were present in multiple samples but each sample had a different population composition. This confirms the observation of Connell and Slayter (1977) that changes in ecosystems lead to changes in population composition. A microbial diversity of 27 species based on 16S rRNA genes was detected 1 day after processing of the samples (t1). This diversity persisted up to 16 days (t16) after the start of the experiment and decreased after 20 days (t20). In their experiment, Varnam and Evans (2000) placed bacteria in a soil sample that resulted in an increased number of added allochthonous species while the amount of autochthonous species decreased within the first 20 days. Species that are brought into the system with process water at the beginning of the clay-alteration process seemed to interact with the allochthonous microorganisms directly or with secreted compounds such as signal molecules for positive growth mediation (Kaeberlein *et al.*, 2002; Peterson *et al.*, 2006) or inhibitory substances.

In the undisturbed sample prior to mining, the lack of oxygen caused a significant diversity of anaerobic species. These were exposed to oxygen after the change in conditions while moistening. Furthermore, autochthonous species that lived in symbiosis or other dependency

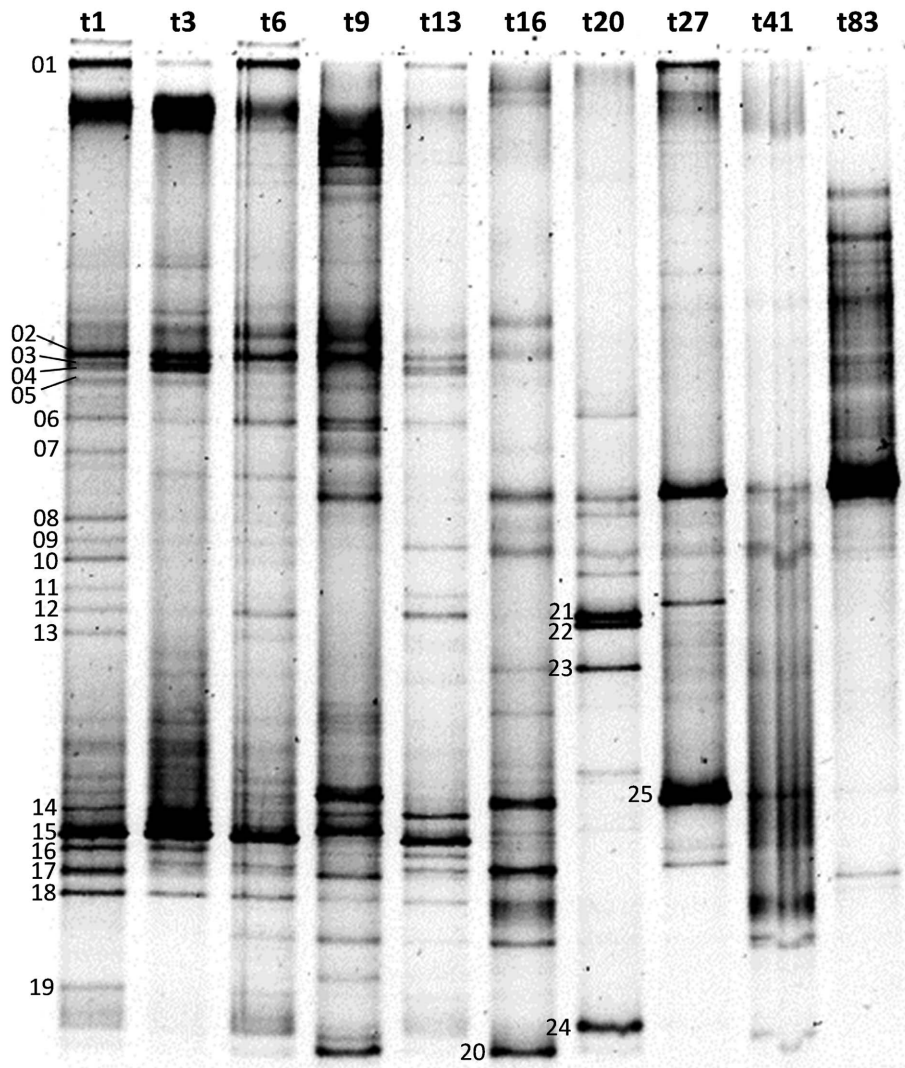

Figure 3. DGGE patterns of the time series t1 to t83 after cultivation on the DCS; bacteria removed by PBS-plate wash; DNA of numbered bands was analyzed (after Kaden *et al.*, 2012).

relationships potentially may not able to survive on a solitary basis. Within hours or days of mining and homogenization of clay, the nutrients are allocated nearly homologously. The microhabitats that are caused by irregular distribution of molecules, and that are characterized by a unique composition of bacterial species as described by Kirk *et al.* (2004), are rarely present at this manipulated state of the system. Such habitats only exist in soils with small particle sizes, such as clays, and are characterized by poor levels of water throughput and thus less physical exchange of nutrients.

After a dwell time, the system stabilized by building new microhabitats due to local metabolic activity and interactions of specific microbial species according to the conditions present which depend on the availability of oxygen, nutrients, and many other ecological factors. The number of detectable species seemed to depend on the particle size of the matrix. Bacteria have almost the same size range (0.2−5 μm) as clay particles. In clays that contain more particles in the <0.6 μm fraction than W2, fewer bacteria might occur. Less microbial biodiversity than in clay is also expected in soils with a large proportion in the >20 μm particle size range because of the flush of nutrients with the leaching water. In contrast, clays have a large water-binding capacity and thus nutrients are much more available. A large microbial diversity was expected in the system examined.

Twenty seven different samples were analyzed and 16 species were detected within the colonies grown that were removed directly from the filter (Table 2). Six of these 16 organisms potentially represented uncultured species regarding the species-level definition with a 16S rRNA gene-homology between two organisms of >97% (Janda and Abbott, 2002). A greater homology of the 16S rRNA gene within different taxa such as *Mycobacterium marinum* and *Mycobacterium ulcerans* the 16S rRNA of which differs by only 0.2% (Stinear *et al.*, 2000) is also possible. At least 37% of all cultured and determined species within the picked colonies were undescribed bacteria.

More than 60% of DNA samples that grew on the PBS washed plates represented potentially new cultured species (Table 3). The genus detected most, *Arthrobacter*, occurs frequently in soils (Cacciari and Lippi, 1987). Aside from their very simple life cycle, some species of *Arthrobacter* are able to survive under difficult conditions such as limited nutrients or in the presence of ionizing radiation, oxygen radicals, and toxic substances (Mongodin *et al.*, 2006). The closest related species of the strains B13 and B16, according to the NCBI database, was *Arthrobacter oxydans* (Table 3), while these two 16S rRNA gene sequences differ by more than 10% (Figure 4). This demonstrates that at least one of these species is not really *Arthrobacter oxydans* and illustrates the difficulties of interpreting sequence database entries.

Within the picked colonies the diversity of genera and the genetic divergence of all taxa were greater than the microbial diversity of the PBS-suspended samples. While species of *Arthrobacter* occurred mainly in the samples obtained from the PBS-washed plates, a few species related to *Pseudomonas* and a great diversity of other taxa were detected within the picked colonies (Figure 4). Some bacteria that grow slowly under the given conditions in the DCS were unable to develop visible single colonies and were not considered in the single colony-selection approach. The differences in detection of bacterial species between these two approaches might also be influenced by bacteria with a lesser abundance but a better state of metabolism that influences directly the number of 16S rRNA copies in the bacterial cell. While starving, bacteria produce a smaller amount of rRNA which increases by the factor 30−70 after nutrients become available (Kramer and

Table 2. Species determined within the colonies analyzed; NCBI PopSet [261288875] (Kaden *et al.*, 2009a).

Colony no.	First entry of described species	Ident	NCBI Acc. No.
C01	*Pseudomonas fluorescens*	99%	
C02	*Sphingobium yanoikuyae*	96%	GU002571
C03=C06	*Enterococcus faecalis*	94%	GU002572
C04	*Nocardioides fulvus*	99%	
C05	*Arthrobacter globiformis*	98%	GU002573
C07=C08	*Pseudomonas borealis*	98%	GU002574
C09	*Pseudomonas aeruginosa*	98%	GU002575
C10=C11	*Streptomyces phaeochromogenes*	99%	
C13	*Thiobacillus plumbophilus*	92%	
C15	*Acidithiobacillus ferrooxidans*	94%	
C16	*Aquaspirillum autotrophicum*	95%	
C17=C26=C27=C28=C29	*Massilia plicata*	98%	GU002579
C18=C21	*Arthrobacter sulfonivorans*	98%	
C19=C20	*Rhizobium giardinii*	98%	GU002576
C22=C25	*Nocardioides jensenii*	95%	GU002577
C23=C24	*Streptomyces caniferus*	98%	GU002578

Table 3. Species determined using the NCBI database; samples from PBS washed plates; NCBI PopSet [261288870] (Kaden and Krolla-Sidenstein, 2009b).

Bar no.	First entry of described species	Ident	NCBI Acc. No.
B01	*Arthrobacter ramosus*	91%	
B02=B06=B08=B11=B13	*Arthrobacter oxydans*	96%	GU002566
B3=B04=B15	*Arthrobacter sulfonivorans*	98%	
B05=B09=B10=B14	*Arthrobacter oryzae*	96%	
B16=B18	*Arthrobacter oxydans*	98%	GU002567
B17	*Arthrobacter globiformis*	95%	
B20	*Terrabacter lapilli*	94%	
B22	*Duganella nigrescens*	96%	GU002568
B23	*Dyella ginsengisoli*	96%	GU002569
B24	*Arthrobacter humicola*	99%	
B25	*Aestuariimicrobium kwangyangensis*	98%	GU002570

Singleton, 1992). Within the plate-wash experiment, some species might exist that are under-represented in terms of abundance but overestimated in terms of the analysis of the 16S rRNA gene. The PCR is a method that amplifies the nucleic acid in an exponential way. The difference in the number of rRNA molecules between two species is enhanced significantly after each cycle of the PCR and may lead to the result that the species with low abundance that were detected in the colony-pick experiment were also present on the washed plate but were undetectable due to the differences in the amount of 16S rRNA molecules resulting after PCR (Figure 5).

Furthermore, all primer pairs are selective and are unable to amplify the DNA of all bacterial species, even the universal 16S rRNA specific primer used in this study. Those alleged disadvantages of the method lead to the question of why no other genetic marker was chosen for the molecular analyses. For species determination, the largest number of entries in the NCBI database exists for the 16S rRNA gene. Furthermore, no PCR primers currently exist that indicate more bacterial species than a general 16S-specific primer combination (Stackebrandt, 2009).

Aside from the methodological challenges described, natural processes in clay may have influenced the results. Many direct interactions exist between clay minerals and microorganisms. Thus, it would be almost impossible to describe and explain the whole ecosystem 'clay' with the recent methods. Culturing bacteria in a clay-free approach might lead to enormous differences in contrast to DCS-cultivation of the inoculum, which

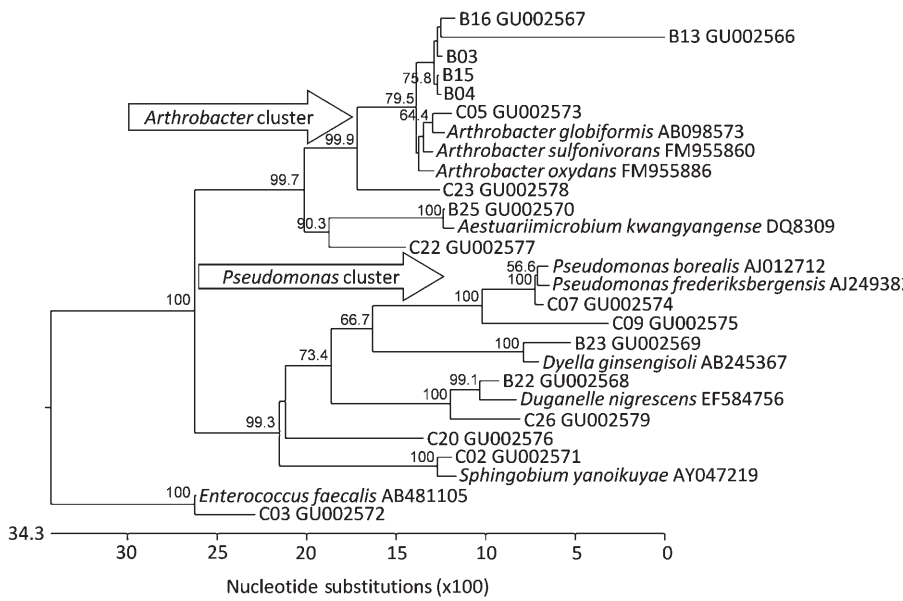

Figure 4. Taxonomic tree (Clustal W neighbor joining method and bootstrap, 1000 trails, seed of 111) of all analyzed sequence samples obtained by cultivation on the DCS, PBS-plate wash technique (BXX) and picked colonies (CXX), PCR, DGGE and sequencing; next related taxa were included (full name and NCBI accession number).

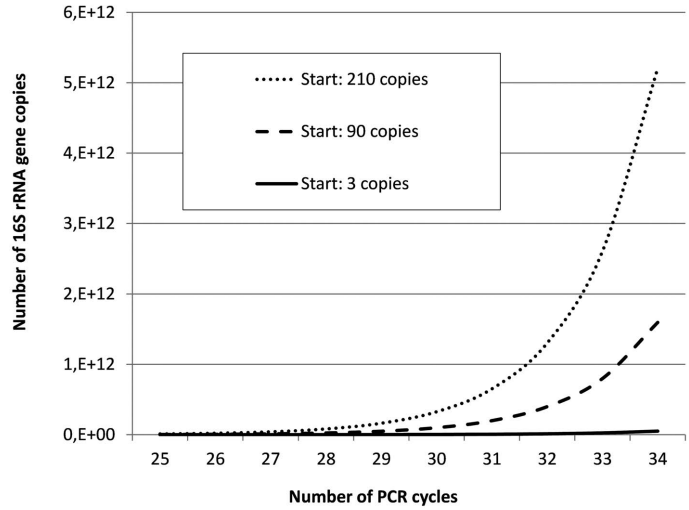

Figure 5. Model of the dependency of the number amplified gene fragments on the number of cycles in PCR assuming that all species occur in the same abundance and species 1 contains three copies of 16S rRNA (poor metabolic state), species 2 and 3 (good metabolic state), 30 and 70 times more 16S rRNA copies, respectively.

was a dilute clay slurry. As a result of direct interaction between clay minerals and microorganisms, the rate of sulfur oxidation is enhanced in *Thiobacillus thiooxidans* in the presence of clay minerals (Rinder, 1979). The products of this process lead to a decreased pH which also influences clay minerals as well as the microbial populations. The type of clay mineral is also important in terms of its effect on microorganisms. *Pseudomonas cepatia* and probably some other undescribed species are able to solubilize inorganic phosphorus in feldspar-rich silicate rocks only in the presence of kaolinite or montmorillonite (Bar-Yosef *et al.*, 1999). Comparable interactions with other available minerals might occur in the clay examined. Some bacteria are able to transform clay minerals. *Shewanella oneidensis* converts smectite to illite (Kim, 2004; Zhang, 2007). The changed properties in terms of the charge of the minerals have an effect on other microbial species. Other than clay, it is possible that for microorganisms no other ecosystem exists that is characterized by such extensive interactions. With the help of DCS, it was possible to culture many known and unknown species that exist in clay. The number of culturable species was enhanced from ~1% up to 60% in the present study.

SUMMARY AND CONCLUSIONS

In the present study, the dynamic cultivation system was applied to culture *in situ* a large number of currently unknown bacteria. Two methods for the removal of biomass from the system were compared. One approach was based on single-colony selection and another on suspension of the whole biomass from the filter. A large abundance of species related to the genus *Pseudomonas* and *Arthrobacter* was detected. Because of the different results from the two approaches used, a combination of these methods is recommended to obtain the largest number possible of taxa. While 60% of the bacteria in the plate-wash approach represented new species, only 37% of the picked-colonies approach were previously undescribed species. In contrast, ~1% of all bacterial species are culturable with common culture methods. The DCS is therefore more applicable to the detection of new species in several clay-mineral-containing matrices than standard media. The method may contribute to a better understanding of several ecosystems, once the bacterial diversity is described. Only with knowledge of the species which occur in clays and how they metabolize the substances available will it be possible to describe interactions between clay minerals and whole bacterial populations. Furthermore, the processes during clay maturation can only be described in detail when all the contributing bacteria are known. This will lead to more time- and cost-efficient clay-maturation procedures in future.

ACKNOWLEDGMENTS

The Project BIOTON was funded by the German Federal Ministry of Education and Research BMBF (Funding No. 01RI0626). The authors are grateful to P. Kuch and M. Dieterle (SIBELCO Deutschland GmbH) for preparing and providing clay samples.

REFERENCES

Altschul, S.F., Gish, W., Miller, W., Myers, E.W., and Lipman, D.J. (1990) Basic local alignment search tool. *Journal of Molecular Biology*, **215**, 403–410.

Bar-Yosef, B., Rogers, R., Wolfram, J., and Richman, E. (1999) *Pseudomonas cepacia*-mediated rock phosphate solubilization in kaolinite and montmorillonite suspensions. *Soil Science Society of America Journal*, **63**, 1703–1708.

Bollmann, A., Lewis, K., and Epstein, S.S. (2007) Incubation of environmental samples in a diffusion chamber increases the diversity of recovered isolates. *Applied and*

Environmental Microbiology, **73**, 6386–6390.
Cacciari, I. and Lippi, D. (1987) Arthrobacters: Successful arid soil bacteria: A review. *Arid Soil Research and Rehabilitation*, **1**, 1–30.
Connell, J.H. and Slayter, R.O. (1977) Mechanisms of succession in natural communities and their role in community stability and organization. *The American Naturalist*, **111**, 1119–1144.
Fiore, S., Dumontet, S., and Huertas, J.F. (2007) Clay minerals and bacteria. *Proceedings of Euroclay 2007*, Aveiro, Portugal, pp. 62–65.
Fischer, S.G. and Lerman, L.S. (1980) Separation of random fragments of DNA according to properties of their sequences. *Proceedings of the National Academy of Sciences of the United States of America – Biological Sciences*, **77**, 4420–4424.
Glick, D.P. (1936) The microbiology of aging clays. *Journal of the American Ceramic Society*, **19**, 169–175.
Gotz, D., Banta, A., Beveridge, T.J., Rushdi, A.I., Simoneit, B.R.T., and Reysenbach, A. (2002) *Persephonella marina* gen. Nov., sp nov and *Persephonella guaymasensis* sp nov., two novel, thermophilic, hydrogen-oxidizing microaerophiles from deep-sea hydrothermal vents. *International Journal of Systematic and Evolutionary Microbiology*, **52**, 1349–1359.
Groudeva, V.I. and Groudev, S.N. (1995) Microorganisms improve kaolin properties. *American Ceramic Society Bulletin*, **74**, 85–89.
Janda, J.M. and Abbott, S.L. (2002) Bacterial identification for publication – when is enough enough? *Journal of Clinical Microbiology*, **40**, 1887–1891.
Kaden, R., Menger-Krug, E., and Krolla-Sidenstein, P. (2009a) NCBI Pop Set [261288875]: Population analysis of clay. NCBI database.
Kaden, R. and Krolla-Sidenstein, P. (2009b) NCBI PopSet [261288870]: The Dynamic Cultivation System, a new method to show temporal shifts in microbial community structure. NCBI database.
Kaden, R., Menger-Krug, E., Emmerich, K., Petrick, K., Mühling, M., and Krolla-Sidenstein, P. (2012) The dynamic cultivation system: A new method for the detection of temporal shifts in microbial community structure in clay. *Applied Clay Science*, **65–66**, 53–56.
Kaeberlein, T., Lewis, K., and Epstein, S.S. (2002) Isolating "uncultivable" microorganisms in pure culture in a simulated natural environment. *Science*, **296**, 1127–1129.
Kim, J., Dong, H.L., Seabaugh, J., Newell, S.W. and Eberl, D.D. (2004) Role of microbes in the smectite-to-illite reaction. *Science*, **303**, 830–832.
Kirk, J.L., Beaudette, L.A., Hart, M., Moutoglis, P., Khironomos, J.N., Lee, H., and Trevors, J.T. (2004) Methods of studying soil microbial diversity. *Journal of Microbiological Methods*, **58**, 169–188.
Kramer, J.G. and Singleton, F.L. (1992) Variations in rRNA content of marine vibrio spp. During starvation-survival and recovery. *Applied and Environmental Microbiology*, **58**, 201–207.
Larkin, M.A., Blackshields, G., Brown, N.P., Chenna, R., McGettigan, P.A., McWilliam, H., Valentin, F., Wallace, I.M., Wilm, A., Lopez, R., Thompson, J.D., Gibson, T.J., and Higgins, D.G. (2007) Clustal W and Clustal X version 2.0. *Bioinformatics*, **23**, 2947–2948.
Mongodin, E.F., Shapir, N., Daugherty, S.C., DeBoy, R.T., Emerson, J.B., Shvartzbeyn, A., Radune, D., Vamathevan, J., Riggs, F., Grinberg, V., Khouri, H., Wackett, L.P., Nelson, K.E., and Sadowsky, M.J. (2006) Secrets of soil survival revealed by the genome sequence of arthrobacter aurescens tc1. *PLoS Genet*, **2**, e214. (doi: 10.1371/journal.pgen.0020214)
Peterson, S.B., Dunn, A.K., Klimowicz, A.K., and Handelsman, J. (2006) Peptidoglycan from bacillus cereus mediates commensalism with rhizosphere bacteria from the cytophaga-flavobacterium group. *Applied and Environmental Microbiology*, **72**, 5421–5427.
Petrick, K., Diedel, R., Peuker, M., Dieterle, M., Kuch, P., Kaden, R., Krolla-Sidenstein, P., Schuhmann, R., and Emmerich, K. (2011) Character and amount of I-S mixed-layer minerals and physical-chemical parameters of two ceramic clays from Westerwald, Germany: Implications for processing properties. *Clays and Clay Minerals*, **59**, 58–74.
QIAGEN (2003) QIAamp DNA Mini Kit and QIAamp DNA Blood Mini Kit 02/2003. User manual, pp. 33–36.
Rinder, G. (1979) Einfluß von tonmineralen auf der verhalten von acidophilen thiobacillus-arten in suspensionen. *Zeitschrift für Allgemeine Mikrobiologie*, **19**, 643–651.
Schuppler, M., Mertens, F., Schon, G., and Gobel, U.B. (1995) Molecular characterization of nocardioform actinomycetes in activated-sludge by 16S rRNA analysis. *Microbiology*, **141**, 513–521.
Stackebrandt, E. (2009) *Phylogeny Based on 16S rRNA/DNA*. eLS. John Wiley & Sons Ltd, Chichester, UK. doi: 10.1002/9780470015902.a0000462.pub2.
Stinear, T., Jentkin, G.A., Johnson, P.D.R., and Davies, J.K. (2000) Comparative genetic analysis of *Mycobacterium ulcerans* and *Mycobacterium marinum* reveals evidence of recent divergence. *Journal of Bacteriology*, **182**, 6322–6330.
Takada-Hoshino, Y. and Naoyuki, M. (2004) An improved DNA extraction method using skim milk from soils that strongly adsorb DNA. *Microbes and Environments*, **19**, 13–19.
Telle, R. (2007) *Salmang scholze keramik*, 7th edition. Springer, Berlin, Heidelberg.
Vaiberg, S.N., Vlasov, A.S., and Skripnik, V.P. (1980) Treating clays with silicate bacteria. *Glass and Ceramics*, **37**, 387–389.
Varnam, A.H. and Evans, G.G. (2000) *Environmental Microbiology*. Manson Publishing, London.
Velde, B. (1995) *Origin and Mineralogy of Clays. Clays and the Environment*. Springer-Verlag, New York, 358 pp.
Weiss, A. (1963) A secret of Chinese porcelain manufacture. *Angewandte Chemie International Edition in English*, **2**, 697–703.
Zeelmaekers, E., McCarty, D., and Mystkowski, K. (2007) *SYBILLA* user manual. Chevron proprietary software, Houston, Texas, USA.
Zhang, G.X., Kim, J.W., Dong, H.L., and Sommer, A.J. (2007) Microbial effects in promoting the smectite to illite reaction: Role of organic matter intercalated in the interlayer. *American Mineralogist*, **92**, 1401–1410.

(*Received 29 July 2013; revised 28 June 2014; Ms. 795; AE: M. Kawano*)

Clays and Clay Minerals, Vol. 62, No. 3, 211–223, 2014.

THE SURFACE MODIFICATION OF ZEOLITE 4A AND ITS EFFECT ON THE WATER-ABSORPTION CAPABILITY OF STARCH-G-POLY (ACRYLIC ACID) COMPOSITE

ZHANG YAN[1,3], ZHAO LIN[1,2,*], MA KAI[2], AND MAO GUOZHU[2]

[1] School of Chemical Engineering and Technology, Tianjin University, 92 Weijin Road, Nankai District, Tianjin 300072, P.R. China
[2] School of Environment Science and Engineering, Tianjin University, 92 Weijin Road, Nankai District, Tianjin 300072, P.R. China
[3] School of Chemistry and Chemical Engineering, Yulin university, 4 Chongwen Road, Yulin City , Shaanxi 719000, P.R. China

Abstract—The surface modification of Zeolite 4A using cetyl trimethyl ammonium bromide (CTAB) as a modifier *via* an ultrasonic method was carried out and the surface physicochemical properties measured. Response surface methodology (RSM) was developed with CTAB concentration, handling time, and handling temperature as variables, to help predict the performance of the modified zeolite under particular conditions. The influence of organic-modified surface treatment and of the amount of modified zeolite on the water-absorption capability of starch-g-poly (acrylic acid) hydrogel composites was also assessed. The results showed that the channels and skeleton structure of zeolite 4A were unchanged after organic modification by CTAB and the surface modification was effective. The results suggest that organic-modified zeolite 4A has improved the water-absorption capability.

Key Words—Organic Modification, Response Surface Methodology, Superabsorbent Composite, Water Absorption, Zeolite 4A.

INTRODUCTION

Superabsorbents have a three-dimensional network of hydrophilic polymers that can swell to an equilibrium state, and retain a significant amount of water and/or biological fluids. Because of this property, superabsorbents have been used extensively in areas such as sanitary goods, waste-water treatment, agriculture, and in medicine for drug-delivery systems since the first superabsorbent polymer was reported by the U.S. Department of Agriculture in 1976 (Li and Wang, 2005; Mohana Raju and Padmanabha Raju, 2001; Lokhande and Gotmare, 1999; Weaver *et al.*, 1976). The absorption capacity is dominated by the ability of three-dimensional networks of superabsorbents to absorb free water. The water-absorption capacity of a superabsorbent is determined both by extension, caused by ionic-charge repulsion of the macromolecular electrolyte, and by expansion resistance, caused by the cross-linking structure and hydrogen bonding (Zhou *et al.*, 2012). The internal micromorphology of a superabsorbent polymer (SAP) also affects directly its absorption mechanism and characteristics (Wang and Zhang, 2006). Most superabsorbents are based on poly(acrylic acid), however, which has poor biodegradability in soil, for example, and so poses an environmental problem. The increasing prices of petrochemical feedstock, concern about waste disposal, and the desire to use renewable and environmentally friendly resources have prompted recent research interest in this area. Starch-grafted copolymers have received considerable attention because the introduction of this biodegradable and low-priced natural starch not only improves the biodegradability of the corresponding superabsorbents, but also reduces dependence on petrochemical monomers (Lanthong *et al.*, 2006; Zdanowicz *et al.*, 2010). Traditional superabsorbent networks of synthetic polymers often have limitations other than poor biodegradability which restrict their application. Many methods have been applied to improve the absorption properties and to extend the range of possible applications of SAPs (Lee and Yang, 2004). Inorganic-organic superabsorbent composites based on mica, attapulgite, and kaolinite have been created in attempts to realize smaller production costs and better water-absorption capacity (Zhang *et al.*, 2006). Starch-grafted acrylic acid/clinoptilolite/fly-ash composite with a water-absorption capacity of 320 g/g was prepared by Zhang *et al.* (2011) who deemed it unsatisfactory. Introduction of the fly-ash modified the zeolite network resulting in its local dissolution and stimulated aggregation that decreased the water absorbency of the composites.

Studies of composites based on zeolites were suggested. Zeolites are highly crystalline aluminosilicates represented by the general formula $M^{+}_{x/n}[(AlO_2)_x(SiO_2)_y]^{x-}\cdot ZH_2O$ (where M is a metal cation, a proton, or less frequently, a charged molecule) (Rožić and Miljanić, 2011). Zeolite crystals are characterized by a regular three-dimensional network of intracrystalline nanovoids. Zeolites have been applied in various fields as sorbents (Faghihian *et al.*, 2013; Rožić and Miljanić, 2011; Haggerty and Bowman, 1994), soil amendments

* E-mail address of corresponding author:
zhaolin@tju.edu.cn
DOI: 10.1346/CCMN.2014.0620305

(Bernardi *et al.*, 2013; Zwingmann *et al.*, 2011), ion exchangers (Wang *et al.*, 2011, 2012; Stojakovic *et al.*, 2011), and catalysts (Saxena *et al.*, 2013) and are classified into various types according to their structures, *e.g.* A, X, Y, ZSM-5, and clinoptilolite. Among them, single-phase zeolite 4A has been of great interest because of its large cation exchange capacity and its large number of acid sites due to its 8-ring, 6-ring, and 4-ring channel structure with the largest cavity dimension measuring 0.41 nm × 0.41 nm; because of this, zeolite 4A is used widely in ion-exchange processes (Hui *et al.*, 2005). Zeolite 4A also has significant absorption capacity, large cation-exchange capacity, and excellent water-holding capacity in the free channels, leading to the interesting and potentially important application of zeolite 4A as a soil amendment in agriculture. The addition of synthetic zeolite pellets to soils contaminated with cadmium was reported by Gworek (1992) to reduce significantly the concentrations of Cd in the roots and shoots of a range of crop plants. Use of synthetic zeolite type 4A, at application rates of 1% by soil weight, caused reductions in Cd concentrations of up to 86% in leaves of lettuce grown in pots, compared to controls with no added zeolites. Asb-A zeolites were synthesized by Le Van Mao *et al*. (1991) who found that these zeolites helped soil to retain moisture for extended periods of time. When the amount of the zeolite material added was 5 wt.% the length of time for which moisture was retained was increased from 3 h to 7 days. The water-retention capacity is heavily dependent on the textural properties of the zeolite materials and the zeolite materials exhibited no *in vitro* cell toxicity. To date, no research has been published on the water-absorption ability of superabsorbent composites in relation to zeolite 4A.

Micro-sized zeolite 4A particles show a strong tendency to aggregate due to their specific surface structure and surface interactions resulting in irregular dispersal in polymeric systems when added directly without pretreatment. The apparent difference between the interfacial characteristics of zeolite 4A and the polymer matrix has resulted in poor compatibility during polymeric synthesis (Guo *et al*., 1999; Ahmad and Hägg, 2003; Khoonsap and Amnuaypanich, 2011). These drawbacks decrease the final absorption capacity of the composite. Chemical modification of zeolite 4A before it is polymerized removes these problems. Surfactants are water-soluble organic molecules which have hydrophilic and hydrophobic properties. Cationic surfactants with positively charged head groups attached to hydrocarbon moieties, such as alkyl ammonium compounds, have been utilized to form organically modified clays (Irani *et al.*, 2013).

The optimization technique referred to as 'one-variable-at-a-time' is often applied to determine the effects of the relevant parameters in the modification process (Wang, *et al*., 2006). The major disadvantage is that it does not account for the interactive effects among the variables studied and so does not illustrate all the effects of the parameter on the response (Lundstedt *et al.*, 1998). Another disadvantage of the one-factor optimization is the increase in the number of experiments required to conduct the research, which leads to increased time and expense as well as increased consumption of reagents and materials. To overcome these problems, response surface methodology (RSM), one of the most sophisticated multivariate statistical methods used in analytical optimization, was deployed. Response surface methodology is a collection of mathematical and statistical techniques based on the fit of a polynomial equation to the experimental data which must describe the behavior of a set of data with the objective of making statistical predictions (Bezerra *et al.*, 2008). The method is used under experimental conditions where a response or a set of responses of interest are influenced by several variables; the levels of these variables can be optimized simultaneously to reach optimal system performance using minimum experimental effort. Box-Behnken designs (BBD) are a class of rotatable or nearly rotatable second-order designs based on three-level incomplete designs. In the present study, a BBD design was proposed to fit a second-order model for optimal conditions studies (Ferreira *et al.*, 2007).

In the present study, organically modified zeolite 4A was synthesized under ultrasonic waves using CTAB as a surfactant to improve the surface properties of zeolite 4A with the aim of increasing its surface reactivity to the starch-g-poly (acrylic acid) matrix. The RSM was applied to determine the optimum modification conditions of the organic-modified zeolite 4A. In addition, the effects of surface treatment of zeolite 4A and the water-absorption capacity of starch-g-poly(acrylic acid)/organic-modified 4A composite were also investigated.

EXPERIMENTAL

Materials

Zeolite 4A purchased from Nan Kai University Catalyst Co., Ltd. (Tianjin, China) was milled using an agate mortar to pass through a 320-mesh screen and treated with NaOH for 24 h followed by washing with distilled water and then dried at 100ºC for 12 h. Zeolite 4A CTAB with a molar mass of 364.46 g/mol and a minimum of 99% of active substance was used. Corn starch was supplied by Tianjin Dingyan Trading & Property Co., Ltd. (Tianjin. China). Acrylic acid was supplied by Tianjin Damao Chemical Reagent Factory (Tianjin, China) and purified by recrystallization. Potassium persulfate was purchased from Tianjin Kewei Chemical Reagent Factory (Tianjin, China) and recrystallized before use. N,N-methylenebisacrylamide (MBA) was supplied by Tianjin Kemiou Chemical Reagent Corp. (Tianjin, China). All the other chemicals were of analytical grade and used without further purification.

Synthesis of modified zeolite 4A

A 3-factors-3-level response surface Box-Behnken design, which required 17 runs including three replicates of the central run, was used in the modification of zeolite 4A with CTAB as the organic modifier under ultrasonic waves. The factors were: CTAB concentration (X_1 = 43.1, 59.1, and 75.1 mmol/L), ultrasonic handling time (X_2 = 30, 60, and 90 min), and handling temperature (X_3 = 30, 50, and 70ºC). Second-order polynomial regression models, as shown below (equation 1) were fitted to the response, in terms of the factors selected:

$$Y_i = b_o + \Sigma b_i X_i + \Sigma b_{ii} X_i^2 + \Sigma\Sigma b_{ij} X_i X_j + \varepsilon \quad (1)$$

Where Y_i represents the response; b_o, b_i, b_{ii}, and b_{ij} were the regression coefficients, X values were the independent factors and ε was the experimental error. Only significant coefficients ($r \leqslant 0.005$) and corresponding terms were included in the model. The factors were coded in three levels (−1, 0, and 1) before fitting the model.

Five grams (5 g) of zeolite 4A and the specified aqueous solution of CTAB were placed in a 500 mL conical flask. The flask was kept in a water bath at the required temperature (30, 50, 70ºC) under ultrasonic waves for specified periods of time (30, 60, 90 min). The reaction product was filtered and washed with aqueous ethanol several times to ensure the complete removal of the Br^-. The product was washed with distilled water and dried at 60ºC, then milled to pass a 180 mesh sieve after grinding using an agate mortar.

Zeolite 4A has the ability to attract positively charged ions due to its electrically neutral framework. The basic structure of zeolite is the Si−O (SiO_4) tetrahedron. During the course of modification with CTAB, Al^{3+} replaces Si^{4+}, so that the entire Al−O tetrahedron bears a single negative charge. In order to maintain electrical neutrality, appropriate positively charged cations must be introduced to offset the negative charge around the vicinity of the Al−O tetrahedron. Sodium or potassium ions are adsorbed on external surfaces and in the pores to balance the charge.

The CTAB as cationic surfactant can diffuse on the external surface and replace the adsorbed ions. When CTAB replaces the adsorbed ions the surfactant acts further to change the charge and chemistry of the zeolite 4A surface. The surfactant adsorbs with its positively charged head group ($C_{16}H_{33}(CH_3)_3N^+$ ions) next to the negatively charged zeolite surface, forcing the hydrophobic surfactant tail to adsorb and be exposed to the solution. Thus, while the native zeolite surface is hydrophilic, the adsorption of a small amount of surfactant on the surface can render it hydrophobic. As shown in equation 2:

$$C_{16}H_{33}(CH_3)_3N^+Br + M\text{-Zeolite 4A} \rightarrow C_{16}H_{33}(CH_3)_3N^+\text{-Zeolite} + MBr \quad (2)$$

(where $M = Na^+$, Ca^{2+}, Mg^{2+}).

Determination of results of modification

Stability of zeolite 4A in deionized water. Modified zeolite 4A (5 g) under optimum conditions with CTAB was added to 400 mL of distilled water using a 500 mL Schott Duran Separating Funnel (Zhou *et al.*, 2005) under stirring to obtain suspension. The system was left to stand for 30 min until no modified zeolite 4A was seen to fall to the bottom of funnel. A test without CTAB was done under the same conditions.

Active index. Zeolite 4A is wetted easily in distilled water due to its hydrophilic surface. Through organic modification, its hydrophilic surface will change to hydrophobic as a result of which organic-modified zeolite 4A will float on the surface of the distilled water instead of being wetted. This makes it easy to test for the modification. 'Active index' is a special term introduced here which means the ratio of the weight of the floating organic-modified zeolite 4A to the total weight of organic-modified zeolite 4A, to explain the effect of the modification reaction. The exact weights of the two kinds of organic-modified zeolite 4A are the values needed to determine the active index.

Stability of zeolite 4A in deionized water. The modified zeolites 4A were divided into two types: one was sediment deposited at the bottom of the vessel, the other was that found floating on the surface of the distilled water. Both types were filtered, dried, and weighed. The active index was calculated from equation 3:

$$H = \left(\frac{M_1}{M}\right) \times 100\% \quad (3)$$

where H denotes the 'active index' of the modified zeolite 4A (%); M denotes weights of total modified zeolite 4A (g), and M_1 denotes sediments from modified zeolite 4A (g). The blank test without CTAB was done under the same conditions as above. All procedures were carried out in triplicate (n = 3) and the value is the mean of three replicates.

Synthesis of starch-g-poly (acrylic acid)/organic-modified zeolite 4A superabsorbent composite

The composite based on corn starch, acrylic acid, NaOH solution, and modified zeolite 4A was synthesized according to the following procedure: 4 g of corn starch was solubilized in 100 mL of distilled water at 90ºC for 60 min using a 500 mL four-neck flask equipped with a reflux condenser, a funnel, and a $N_{2(g)}$ line. Then, while the temperature was cooled to 45ºC, 5 g/L of potassium persulfate was added to the system. After 15 min, the mixed solution of sodium acrylate (acrylic acid partially neutralized with 80 mol.% NaOH solution), 5 g/L of N, N-methylenebisacrylamide (MBA), and specific amounts of modified zeolites 4A under optimum conditions (weight ratios of modified

zeolites 4A/acrylic acid of 5−40 wt.%) were added. The water bath was heated slowly to 70ºC and kept at that temperature for 3 h to complete the polymerization reaction. Throughout the process the system was under a N_2 atmosphere. The material obtained was washed several times with ethanol to ensure the complete removal of the homopolymer. The superabsorbent was oven-dried at 75ºC. As mentioned above, a blank sample, without organic-modified zeolite 4A, was also synthesized and is referred to here as starch-g-poly (acrylic acid). A proposed mechanistic pathway for the synthesis of the starch-g-poly (acrylic acid) is presented in Figure 1 (Spagnol *et al.*, 2012).

Evaluation of water absorption for the composite

The water-absorption capacity of the composite was determined at ambient temperatures using the procedure of Alummoottil *et al.* (2010). The composite (0.1 g) was immersed in distilled water (200 mL) for 24 h to reach its swelling equilibrium (resulting from the absorption of water within the network of the composites). Residual water was removed by filtration over an 80-mesh screen for 25 min. The water-absorption capacity was calculated as the weight of the water absorbed per gram of dry composite. In addition, the sample was weighed at various time intervals to follow the kinetics of swelling in water. The water absorption for starch-g-poly (acrylic acid)/organic-modified zeolite 4A composite was determined according to equation 4:

$$W = [m/m_0] - 1 \quad (4)$$

where W was the mass of the water gained per gram of the dry composite (g/g), m was the mass of the swollen absorbent (g), and m_0 was the mass (g) of the dry composite. Three replicates were tested for each component.

X-ray diffraction analysis

The powder X-ray diffraction (XRD) traces of the samples were obtained using a Bruker X-ray diffractometer (Model D8 Advance, Bruker AXS, Madison, Wisconsin, USA) with CuKα radiation (λ = 0.15406 nm) source.

Infrared spectroscopy

Infrared spectra of unmodified zeolite 4A and the modified zeolite 4A were recorded using a Nicolet-6770 Fourier Transform Infrared (FTIR) instrument with the KBr pressed-disk technique. Spectra were taken over the spectral range 4000−400 cm^{-1} with a resolution of 4 cm^{-1}.

Scanning electron microscopy

A Nanosem 430 scanning electron microscope (SEM) with energy dispersive X-ray spectrometer (EDS) was

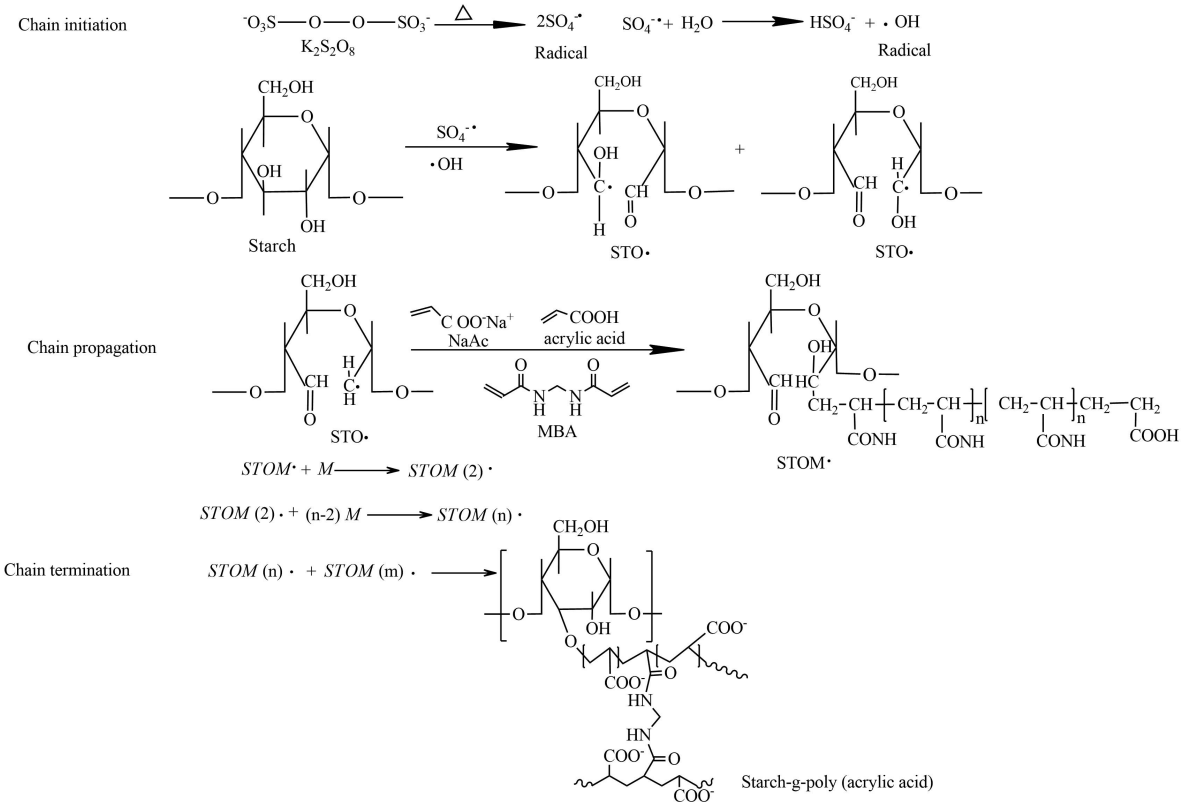

Figure 1. Proposed mechanistic pathway for synthesis of the starch-g-poly (acrylic acid).

used to obtain secondary electron images of the unmodified zeolite 4A, modified zeolite 4A surface, starch-g-poly (acrylic acid), starch-g-poly(acrylic acid)/zeolite 4A, and starch-g-poly(acrylic acid)/organic-modified zeolite 4A. Specimens for examination by SEM were prepared by coating with a thin gold layer to enhance the conductivity and secondary electron emission characteristics and to avoid surface charging under the electron beam.

Statistical analysis

The data were analyzed statistically using the *Design-Expert* package (Razali *et al.*, 2012) to perform ANOVA (analysis of variance), to fit the second-order polynomial equations and to generate second-order surface plots (Dawood and Li, 2013). Coefficients of determination (R^2) were computed and the adequacy of the model was tested by separating the residual sum of squares into pure error and lack of fit. Three replicates were tested for each.

RESULTS AND DISCUSSION

Analysis of the stability of zeolite 4A in deionized water

Prior to modification (Figure 2a), some of the zeolite 4A dispersed into the deionized water and a large of proportion was deposited at the bottom of the Schott Duran Separating Funnel. No zeolite 4A was observed on the surface of the deionized water, demonstrating that zeolite 4A was hydrophilic. After modification under optimum conditions (Figure 2b), zeolite 4A was seen to float on the surface of the deionized water and an obvious interface layer was formed. These results revealed that CTAB was effective at modifying zeolite 4A; the dispersion of zeolite 4A in deionized water was reduced. This result is attributed to the fact that CTAB is a long-chain cationic surfactant which possesses a permanent positive charge. When brought into contact with zeolite 4A, the HDTMA exchanges selectively with the inorganic cations on the external surfaces of the zeolite and forms a surfactant layer with anion-exchange properties (Misaelides, 2011). The surfactant layer helps to improve the hydrophobic capability.

Optimization of the modification conditions for the active index

The active indexes of the samples obtained under different conditions are presented in Table 1. The active indexes of the samples ranged from 20.55 to 98.81% with the largest value obtained from the sample which was modified under the following conditions: CTAB concentration of 59.1 mmol/L, ultrasonic handling time of 60 min, and ultrasonic handling temperature of 50ºC.

Response surface methodology applied to the variables indicated that the experimental data had an

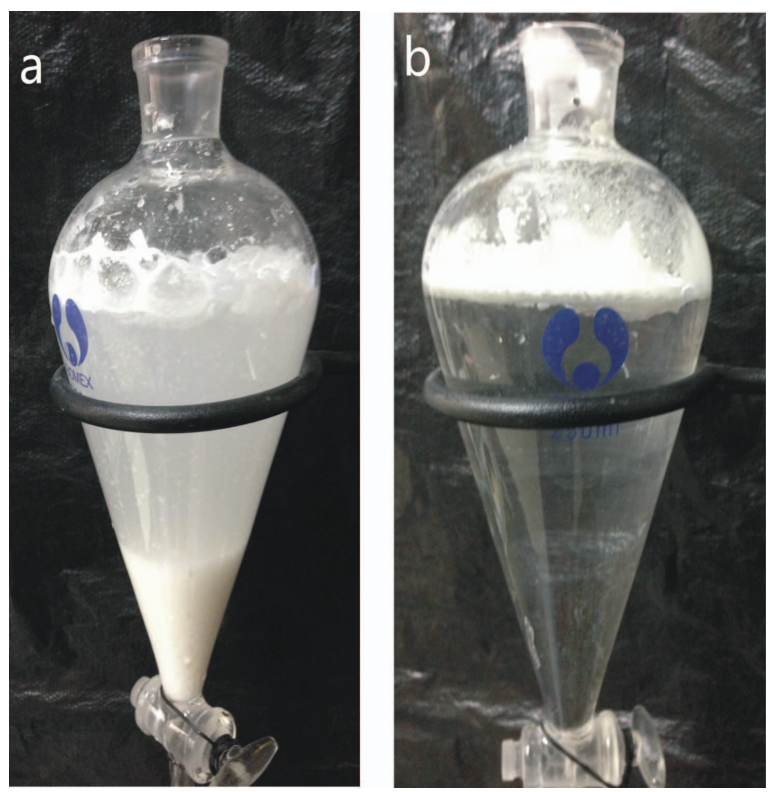

Figure 2. Stability of zeolite 4A in distilled water (a) without modification, and (b) following modification using CTAB.

Table 1. The active index, concentration of CTAB, handling time, and handling temperature of modified zeolite 4A*.

Sample	Concentration of CTAB (mmol/L)	Handling time (min)	Handling temperature (ºC)	Active index (%)
S_1	59.1	30	50	62.96
S_2	59.1	60	50	95.26
S_3	43.1	60	70	64.05
S_4	43.1	30	50	60
S_5	75.1	60	30	97.92
S_6	43.1	90	50	88.99
S_7	59.1	60	50	97.85
S_8	75.1	30	50	22.73
S_9	59.1	60	50	98.81
S_{10}	59.1	30	30	20.55
S_{11}	59.1	90	30	84.16
S_{12}	59.1	90	70	51.93
S_{13}	59.1	60	50	99.9
S_{14}	75.1	90	50	20.13
S_{15}	75.1	60	70	34.73
S_{16}	59.1	60	50	98.19
S_{17}	43.1	60	30	55.68
Unmodified zeolite 4A*				20.48

* Values are the mean of three replicates.

adequate fit to a second-order polynomical model ($\rho < 0.5$). The model showed the active index to be a function of the reaction variable, as represented in equation 5. Only significant effects were retained in the fitted model.

$$Y = 98 - 11.65X_1 + 9.87X_2 - 5.58X_3 - 20.92X_1^2 - 29.12X_2^2 - 13.98X_3^2 - 7.90X_1X_2 - 17.89X_1X_3 - 148.66X_2X_3 \quad (5)$$

The linear and quadratic terms of the three variables have significant effects on the active index ($\rho < 0.5$). The negative coefficients of the quadratic effects of concentration of CTAB, handling time, and handling temperature indicate a decrease in the active index after reaching an optimum. The results showed that the interaction effect of concentration of CTAB and ultrasonic handling time had a significant effect on the active index ($\rho < 0.5$).

The trend was visualized in the three-dimensional surface plots of the predicted models for the active index according to changes in concentration of CTAB and handling time (Figure 3a), the CTAB concentration and the handling temperature (Figure 3b), and handling time and handling temperature (Figure 3c) on the activation of the modified zeolites 4A, when the other variable was fixed at the middle of its three given values.

The value of the coefficient of determination (R^2) was calculated as 0.83 for equation 5. The equation explains 83% of the total variation for H%, which shows the good prediction performance of the proposed model. This also confirmed that the process parameters selected had an influence on the degree of modification.

The optimum conditions for obtaining the maximum active index were predicted using the quadratic model proposed by the RSM modeling of the reaction. The values of the three factors involved were as follows: concentration of CTAB = 59.1 mmol/L, handling time = 60 min, and handling temperature = 50ºC. The active indexes of experiment and analysis under the optimum conditions mentioned above were 98.10% and 98.19%, respectively. This result verified the feasibility and effectiveness of the RSM.

XRD analysis

The diffraction patterns (Figure 4a,b) showed that both the modified and unmodified zeolite 4A presented diffraction peaks at 7.5º2θ, 16.2º2θ, 21.7º2θ, and 24.2º2θ characteristic of the 100, 110, 111, and 210 planes which are characteristic of the crystalline form of zeolite 4A. In addition, no diffraction peaks belonging to CTAB in the diffraction profile of modified zeolite 4A (Figure 4a) were found, indicating that introduction of CTAB did not lead to destruction of the zeolite 4A crystals and confirmed that the modification process took place on the surface of the zeolite 4A. The zeolite 4A cavity dimensions (0.4 nm) are much smaller than the length of the HDTMA alkyl chains (2.3 nm), and this prevents penetration by organocations into these pores. As a result, the structure of the modified zeolite 4A will not be changed during modification.

The process performed to obtain the organic-modified zeolite 4A led to XRD patterns which are characteristic of zeolite 4A with a series of sharp reflections compared to unmodified zeolite 4A. This is due to the preference of CTAB for attacking the amorphous regions of zeolite 4A under suitable temperatures through ultrasonic treatment, which increased the amount of crystalline domains in the zeolite 4A nanocrystals obtained and formed significant long-range order characteristics of the crystals.

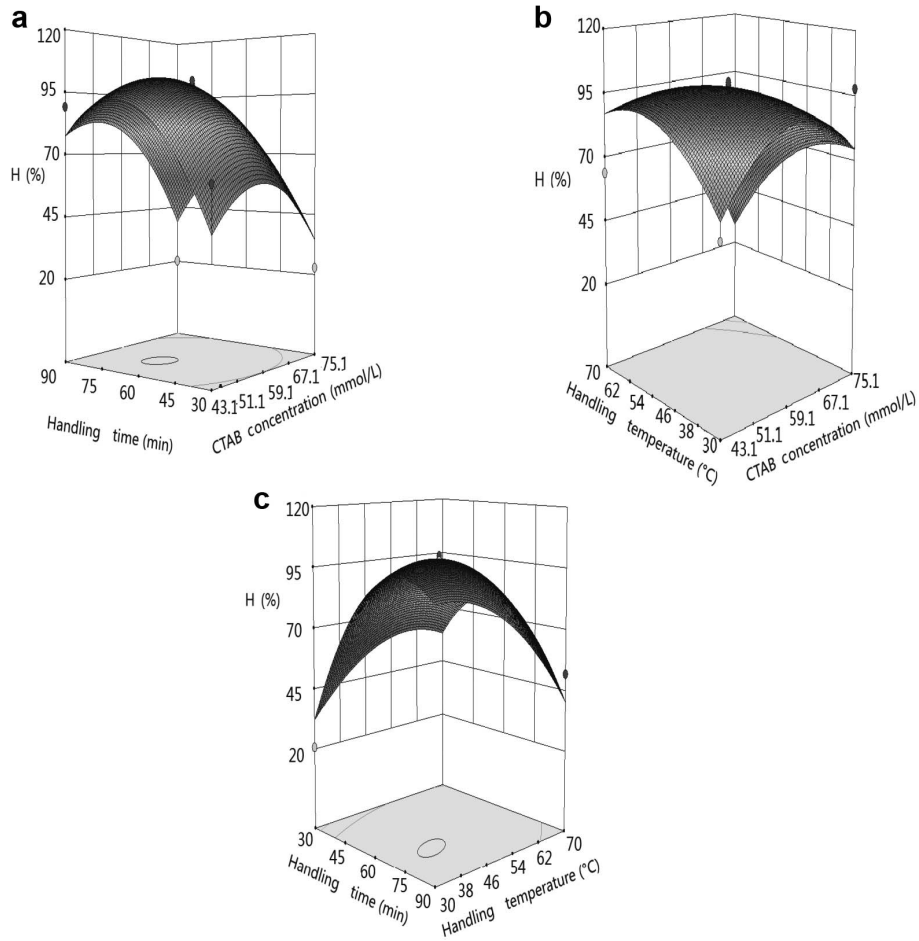

Figure 3. Response surface plots showing the effect of: (a) handling time and concentration of CTAB (X_3 = 50ºC); (b) handling temperature and concentration of CTAB (X_2 = 60 min); and (c) handling time and handling temperature (X_1 = 59.1 mmol/L) on the active index of organic-modified zeolite 4A.

FTIR analysis

The FTIR spectra of natural zeolite 4A and modified zeolite 4A under optimum conditions (Figure 5a,b) presented similar FTIR spectra in the range 500−1300 cm^{-1}. These bands are associated with Si−O−Si and Si−O−Al bending and stretching belonging to the major bands of the aluminosilicate and forming the crystal structure. At the same time, the spectra of modified zeolite 4A (Figure 5b) showed that the CTAB did not affect the linkage of Si−O and Al−O bonds. Thus, the band positions remained the same.

Two other groups of bands belonging to the modified zeolite 4A (Figure 5b) at 1630−1650 and 3500 cm^{-1} were also observed. In the first group, the absorption band is related to the bending vibration of water molecules absorbed on the natural zeolite and on the modified zeolite. In the second group, the broad band was related to the overlapping asymmetric and symmetric bands due to OH-stretching vibrations of the structural OH groups at 3433 cm^{-1}. The most intense absorption bands at 2970 and 2877 cm^{-1} arise from CH_2 asymmetric and symmetric stretching vibration modes of methylene groups in the FTIR spectrum of the crystalline CTAB. Such absorption bands can be observed in the FTIR spectrum of modified zeolite 4A (Figure 5b). For the zeolite 4A modified with CTAB, the ν_{as}, ν_s of CH_2 and methylene modes present at 1472 cm^{-1} were visible, verifying that CTAB was absorbed onto the zeolite surface and the characteristic absorption bands of zeolite 4A did not change after modification. These results were consistent with the XRD analysis.

SEM analysis

The morphology and size of the zeolite are of tremendous importance for their performance in any specific application. The SEM images of the unmodified zeolite 4A and modified zeolite 4A crystals (Figure 6) revealed shapes and sizes of zeolite 4A. The average crystal size was ~2−4 μm. The SEM observations (Figure 6a,b) confirmed the crystalline nature of zeolite 4A and the crystal morphology which can be described in terms of closely bound aggregates of small cubic

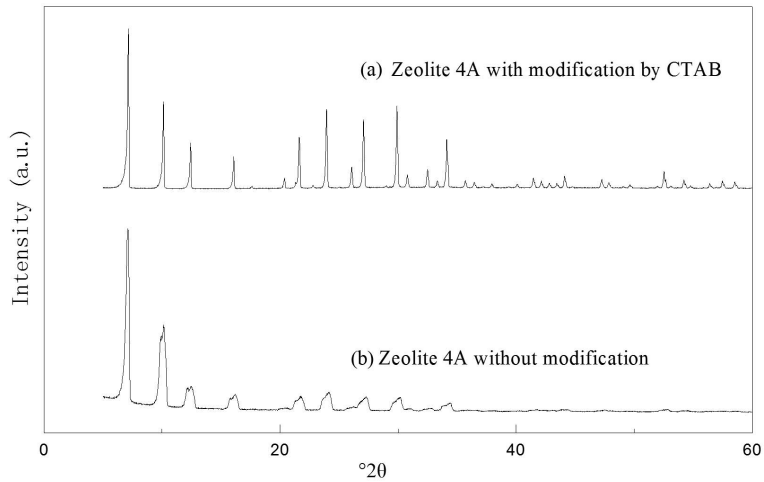

Figure 4. XRD patterns of (a) zeolite 4A following modification by CTAB under optimum conditions, and (b) zeolite 4A without modification.

particles. These crystalline aggregates, however, were not clearly visible on the SEM images of the modified zeolite 4A (Figure 6c,d). The particles of modified zeolite 4A can be dispersed favorably due to CTAB coverage on the external crystal surface and the SEM images proved that the surface modification had no obvious influence on the crystal structure of zeolite 4A.

Effect of organic-modified zeolite 4A content on water absorption by superabsorbent composites

The effect on water absorption of the amount of organic-modified zeolite 4A in the superabsorbent composite is illustrated in Figure 7. According to the results, water absorption by the superabsorbent composite increased with increasing organic-modified zeolite 4A content when the amount of organic-modified zeolite 4A was <10 wt.%. This is attributed to the fact that the presence of the organic-modified zeolite 4A in the starch-g-poly (acrylic acid) polymeric network improved the polymeric network – the long alkyl chains from CTAB are attached to the surface of the zeolite 4A rather like tadpoles, resulting in the formation of tiny hydrophobic regions in the polymeric network. The long alkyl chains are in the polymeric network when the superabsorbent composite is in a dry state; they are unfolded owing to the repulsion among the hydrophobic long alkyl chains when the superabsorbent composite is swollen in water. On the other hand, the water-absorption capacity decreased when the amount of organic-modified zeolite 4A was >10 wt.%. The excess organic-modified zeolite 4A in the superabsorbent network prevents water from being absorbed.

The surface of organic-modified zeolite 4A with long alkyl chains acts as a set of additional network points, which can participate in the polymerization reaction and

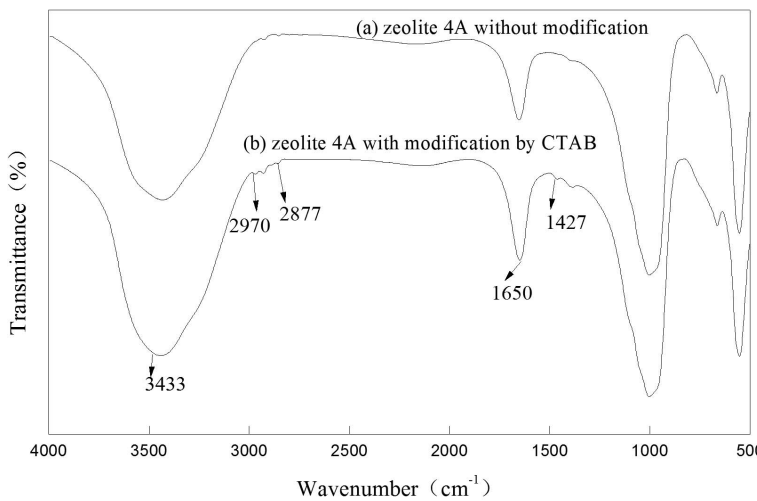

Figure 5. FTIR spectra of (a) zeolite 4A before modification, and (b) zeolite 4A following modification using CTAB under optimum conditions.

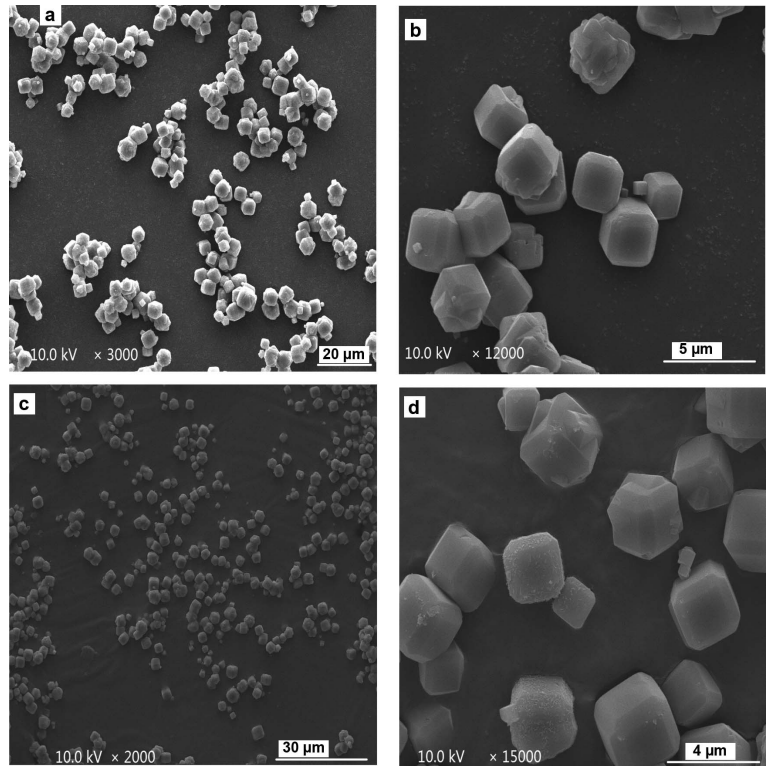

Figure 6. SEM images, at different magnifications, of (a, b) zeolite 4A without modification, and (c, d) zeolite 4A following modification using CTAB under optimum conditions.

in the formation of a 3D polymer network. As a result, the intertwining of polymerization chains was precluded and the hydrogen-bonding interactions among the hydrophilic groups, such as −COOH, −COO−, and −OH, among others, became weaker. Thus, the degree of physical crosslinking decreased and the network sites for uptake of water molecules were more available, which favors water absorption. A larger amount of organic-modified zeolite 4A, however, results in the generation of more crosslink points and fewer network

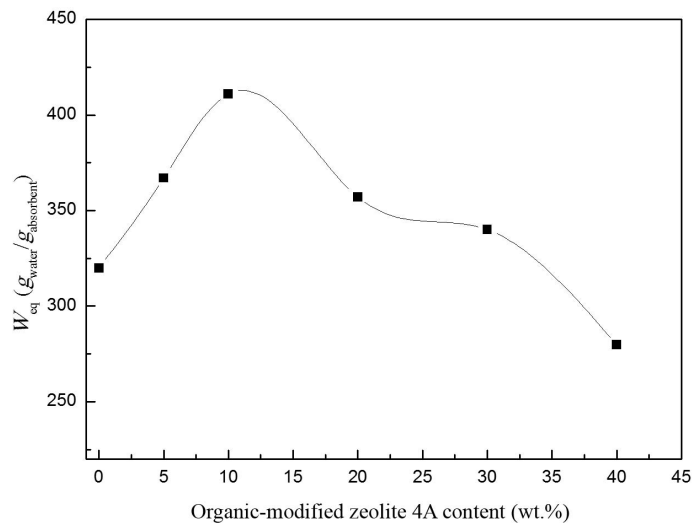

Figure 7. Effect of the amount of organic-modified zeolite 4A on water absorption by starch-g-poly (acrylic acid)/organic-modified zeolite 4A superabsorbent composite (organic-modified zeolite 4A under optimum modification conditions; concentration of potassium persulfate = 5 g/L; concentration of MBA = 5 g/L; reaction temperature = 70ºC; reaction time = 3 h; degree of neutralization = 80%).

voids which are responsible for absorbing and taking up water molecules. Also, the excess organic-modified zeolite 4A may stack physically within the network voids. The larger the amount of organic-modified zeolite 4A, the larger is the crosslink density of the superabsorbent composite. This means that the space network for water molecules to enter becomes smaller and the water-absorption capacity decreases gradually. Some voids were plugged and so water absorption decreased for that reason also.

The water-absorption capacity of the starch-graft poly (acrylic acid) was 320 g/g. The starch-graft poly (acrylic acid)/organic-modified zeolite 4A obtained had a water-absorption capacity of 410 g/g under optimized conditions. The water-absorption properties of starch-graft acrylic acid/zeolite/fly ash *via* the aqueous solution polymerization method was studied by Zhang *et al*. (2011). They found that the water absorption of the superabsorbent composite was 314.4 g/g. The present study gave a better result possibly because of the different zeolite and different method of modification used. The use of CTAB as an organic modifier was reported (Guo *et al*., 1999) to bring about tremendous increase in the dispersion capacity of zeolite.

Surface morphology of starch-g-poly (acrylic acid)/ organic-modified zeolite 4A superabsorbent composite

SEM images of starch-g-poly (acrylic acid), starch-g-poly (acrylic acid)/with 10 wt.% zeolite 4A, and starch-g-poly (acrylic acid)/organic-modified zeolite 4A with 10 wt.% superabsorbent composites are shown in Figure 8. The image of starch-g-poly (acrylic acid) (Figure 8a) shows a smooth and tight surface, but the addition of zeolite 4A leads to a rough surface (Figure 8b) which is convenient for the penetration of water into the polymeric network. Compared with starch-g-poly (acrylic acid) and starch-g-poly (acrylic acid)/zeolite 4A, starch-g-poly (acrylic acid)/organic-

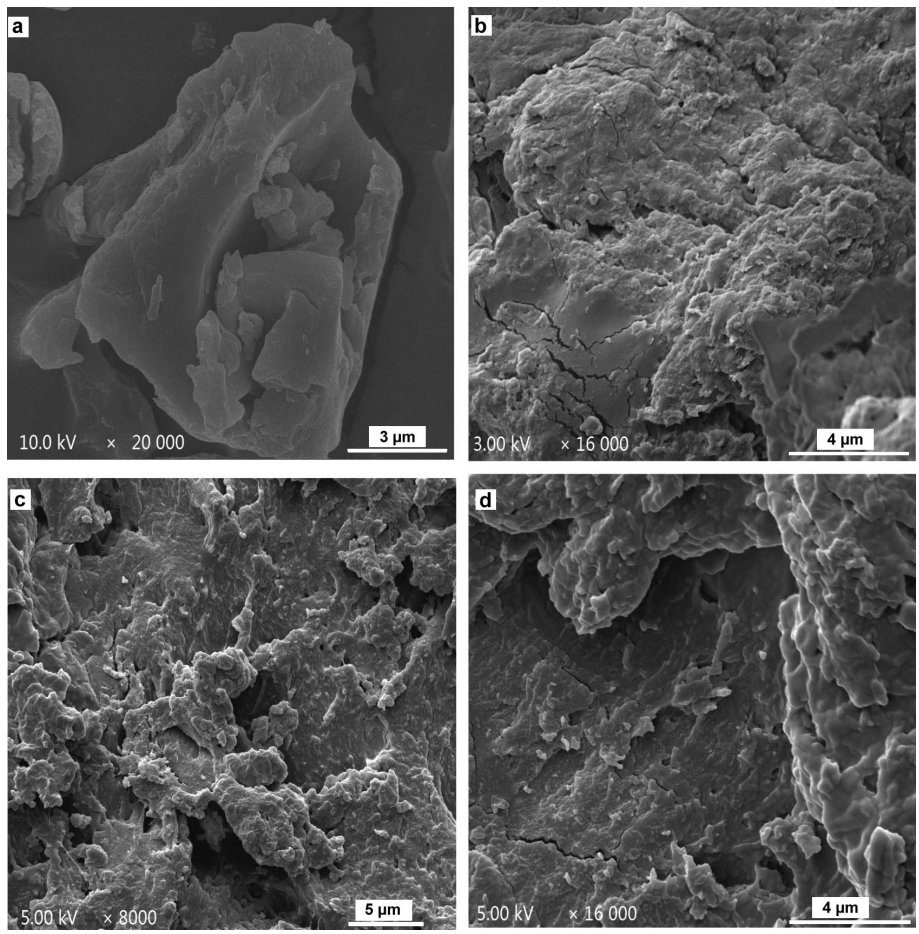

Figure 8. SEM images of (a) starch-g-poly (acrylic acid), (b) starch-g-poly (acrylic acid)/zeolite 4A without modification, (c, d) starch-g-poly (acrylic acid)/organic-modified zeolite 4A (zeolite 4A content = 10 wt.%; organic-modified 4A content under optimum modification conditions = 10 wt.%, potassium persulfate concentration = 5 g/L; MBA concentration = 5 g/L; reaction temperature = 70 ºC; reaction time = 3 h; neutralization degree = 80%).

modified zeolite 4A superabsorbent composites (Figure 8c,d) has a coarse, polyporous, and corrugated surface. This surface structure also facilitates the permeation of water. Incorporation of zeolite 4A both with modification and without modification clearly introduces a rough surface which is related to equilibrium-water absorbency and swelling behaviors of the corresponding superabsorbent composites (Figure 8b–d). In addition, no phase separation is observed in Figure 8c or 8d. This morphology reconfirms the homogeneity of the superabsorbents synthesized as real superabsorbent composites.

Swelling kinetics analysis

The swelling kinetics in aqueous media for starch-g-poly (acrylic acid)/organic-modified zeolite 4A superabsorbent composite with 10 wt.% organic-modified zeolite 4A and starch-g-poly (acrylic acid) (Figure 9a) indicated that the profiles of swelling kinetics were similar. The degree of swelling increased quickly during the first 80 min after the immersion, reaching 95 wt.% of the equilibrium value in this time. The degree of swelling then increased slowly until the equilibrium was reached ~50 min later, depending on the products. Both have high initial swelling rates in distilled water. In general, the initial swelling rate is determined primarily by the penetration of water into the polymeric network through diffusion and capillarity (Mathakiya *et al.*, 1998). Osmotic pressure and chain relaxation may also be responsible for the high swelling rate.

The incorporation of organic-modified 4A zeolite within the starch-g-poly (acrylic acid) network increased the water-absorption capacity at equilibrium conditions. The water-absorption capacity of starch-g-poly (acrylic acid) composite is 320 g/g while that for starch-g-poly (acrylic acid)/organic-modified zeolite 4A superabsorbent composite is 410 g/g meaning that the introduction of organic-modified zeolite 4A into polymeric networks helps to improve the absorption capacity of superabsorbent composites. This behavior is because OH on the surface of organic-modified zeolite 4A increases the affinity of the polymeric network for water molecules. Another reason for the superabsorbent composite in traduced organic-modified zeolite 4A achieving greater absorption values may be that it has a coarse surface and capillarity is more evident, thereby accelerating the penetration of water molecules into the polymeric network.

Some of the characteristics collected from the swelling curves, used to evaluate the swelling mechan-

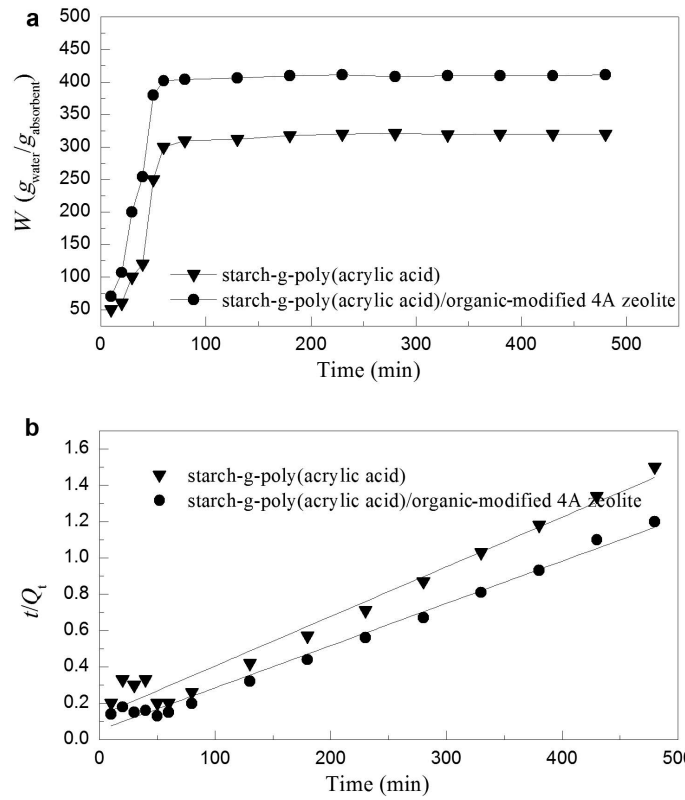

Figure 9. (a) Swelling kinetics curves and (b) t/Q_t *vs.* time plot for the starch-g-poly acrylic acid and starch-g-poly (acrylic acid)/organic-modified zeolite 4A superabsorbent composites (zeolite 4A content = 10 wt.%; organic-modified 4A content under optimum modification conditions = 10 wt.%; potassium persulfate concentration = 5 g/L; MBA concentration = 5 g/L; reaction temperature 70ºC; reaction time 3 h; neutralization degree = 80%).

ism of superabsorbents – Schott's pseudo-second order swelling kinetics model (Schott, 1992) – were adopted to fit the experimental data. The pseudo-second order swelling kinetic model can be expressed through the relations proposed below:

$$t/Q_t = A + Bt \quad (6)$$

where:

$$A = 1/kQ_\infty^2 \quad (7)$$

and

$$B = 1/Q_\infty \quad (8)$$

where k is the constant rate for swelling, t is the swelling time, Q_t is a theoretical swelling value at moment t, and Q_∞ is a theoretical swelling value at equilibrium. Q_∞ and k were calculated by fitting experimental data (Figure 9a,b, equations 6–8).

Depending on experimental data, the plot of t/Q_t *vs.* the starch-g-poly(acrylic acid) and starch-g-poly(acrylic acid)/organic-modified 4A zeolite composite (Figure 9b) gave perfect straight lines with a good linear correlation coefficient ($R^2 > 0.98$), indicating that the swelling processes of the superabsorbents followed the Schott swelling kinetic model.

CONCLUSIONS

Organic-modified zeolite 4A particles as inorganic functional materials were first incorporated into the polymer with a view to manufacturing superabsorbent composites with good water-absorption properties. The zeolite Active index test, XRD, FTIR, and SEM were performed to evaluate the effects of surface treatment of zeolite 4A and RSM was used to investigate the optimum condition for the surface treatment. Starch-g-poly (acrylic acid) composites with doped organic-modified zeolite 4A were prepared by the aqueous-solution polymerization method and the water absorptions of the composites were determined. The experimental results indicated that CTAB has a significant effect on the surface modification of zeolite 4A. The water-absorption capacity increased with increasing organic-modified zeolite content up to 10 wt.%. At a 10 wt.% loading, the greatest capacity, 410 g/g, was reached. In addition, swelling-kinetics analysis in distilled water was performed and the results revealed that the introduction of the organic-modified zeolite 4A can improve the water-absorption capacity of the superabsorbent composite.

ACKNOWLEDGMENTS

The authors acknowledge the National Key Technology R&D Program of the Ministry of Science and Technology, P.R. China (No.2012BAC07B02) for support and for providing the funds to make this study possible.

REFERENCES

Ahmad, J. and Hägg, M. (2013) Preparation and characterization of polyvinyl acetate/zeolite 4A mixed matrix membrane for gas separation. *Journal of Membrane Science*, **427**, 73–84.

Alummoottil, N.J., Janardhanan, S., Subramoney, N.M., and Moothandaserry, S.S. (2010) Response surface methodology for the optimization and characterization of cassava starch-graft-poly (acrylamide). *Starch - Stärke*, **62**, 18–27.

Bernardi, A.C.D., Oliviera, P.P.A., Monte, M.B.D., and Barros, F.S. (2013) Brazilian sedimentary zeolite use in agriculture. *Microporous and Mesoporous Materials*, **167**, 16–21.

Bezerra, M.A., Santelli, R.E., Oliveira, E.P., Villar, L.S., and Escaleira, L.A. (2008) Response surface methodology (RSM) as a tool for optimization in analytical chemistry. *Talanta*, **76**, 965–977.

Dawood, A.S. and Li, Y. (2013) Modeling and optimization of new flocculant dosage and pH for flocculation: removal of pollutants from wastewater. *Water*, **5**, 342–355.

Faghihian, H., Moayed, M., Firooz, A., and Iravani, M. (2013) Synthesis, characterization, and evaluation of a ferromagnetically modified natural zeolite composite for removal of Cs^+ and Sr^{2+}. *Clays and Clay Minerals*, **61**, 193–203.

Ferreira, S.L.C., Bruns, R.E., Ferreira, H.S., Matos, G.D., David, J.M., Brandão, G.C., da Silva, E.G.P., Portugal, L.A., dos Reis, P.S., Souza, A.S., and Dos Santos, W.N.L. (2007) Box-Behnken design: An alternative for the optimization of analytical methods. *Analytica Chimica Acta*, **597**, 179–186.

Guo, L.P., Chen, Y.Z., and Yang, J. (1999) The surface modification of zeolite-4A by CTAB and its properties. *Journal of Wuhan University of Technology-Material*, **14**, 18–23.

Gworek, B. (1992) Inactivation of cadmium in contaminated soils using synthetic zeolites. *Environmental Pollution*, **75**, 269–271.

Haggerty, G.M. and Bowman, R.S. (1994) Sorption of chromate and other inorganic anions by organo-zeolite. *Environmental Science & Technology*, **28**, 452–458.

Hui, K.S., Chao, C.Y.H., and Kot, S.C. (2005) Removal of mixed heavy metal ions in wastewater by zeolite 4A and residual products from recycled coal fly ash. *Journal of Hazardous Materials*, **127**, 89–91.

Irani, M., Ismail, H., and Ahmad, Z. (2013) Preparation and properties of linear low-density polyethylene-g-poly (acrylic acid)/ organo-montmorillonite superabsorbent hydrogel composites. *Polymer Testing*, **32**, 502–512.

Khoonsap, S. and Amnuaypanich, S. (2011) Mixed matrix membranes prepared from poly(vinyl alcohol) (PVA) incorporated with zeolite 4A-graft-poly(2-hydroxyethyl methacrylate) (zeolite-g-PHEMA) for the pervaporation dehydration of water-acetone mixtures. *Journal of Membrane Science*, **367**, 182–189.

Lanthong, P., Nuisin R., and Kiatkamjornwong, S. (2006) Graft copolymerization, characterization, and degradation of cassava starch-g-acrylamide/itaconic acid superabsorbents. *Carbohydrate Polymers*, **66**, 229–245.

Le Van Mao, R., Sjiariel, B., and Dunnigan, J. (1991) Asbestos-derived zeolites as water-retaining materials in soils. *Zeolites*, **11**, 804–809.

Lee, W.F. and Yang, L.G. (2004) Superabsorbent polymeric materials. XII. Effect of montmorillonite on water absorbency for poly (sodium acrylate) and montmorillonite nanocomposite superabsorbents. *Journal of Applied Polymer Science*, **92**, 3422–3429.

Li, A. and Wang, A.Q. (2005) Synthesis and properties of clay-based superabsorbent composite. *European Polymer Journal*, **41**, 1630–1637.

Lokhande, H.T. and Gotmare, V.D. (1999) Utilization of textile loomwaste as a highly absorbent polymer through graft copolymerization. *Bioresource Technology*, **68**, 283–286.

Lundstedt, T., Seifert, E., Abramo, L., Thelin, B., Nyström, Å., Pettersen, J., and Bergman, R. (1998) Experimental design

and optimization. *Chemometrics and Intelligent Laboratory Systems*, **42**, 3–40.

Mathakiya, I., Vangani, V., and Rakshit, A.K. (1998) Terpolymerization ofacrylamide, acrylic acid, and acrylonitrile: Synthesis and properties. *Journal of Applied Polymer Science*, **69**, 217–228.

Misaelides, P. (2011) Application of natural zeolites in environmental remediation: A short review. *Microporous and Mesoporous Materials*, **144**, 15–18.

Mohana Raju, K. and Padmanabha Raju, M. (2001) Synthesis and swelling properties of superabsorbent copolymers. *Advances in Polymer Technology*, **20**, 146–154.

Razali, M.A., Sanusi, N., Ismail, H., Othman, N., and Ariffin, A. (2012) Application of response surface methodology (RSM) for optimization of cassava starch grafted polyDADMAC synthesis for cationic properties. *Starch - Stärke*, **64**, 935–943.

Rožić, M. and Miljanić, S. (2011) Sorption of HDTMA cations on Croatian natural mordenite tuff. *Journal of Hazardous Materials*, **185**, 423–429.

Saxena, S.K., Kumar, M., and Viswanadham, N. (2013) Studies on textural properties of lanthanum-exchanged Y zeolites as promising materials for value upgradation of Jatropha oil. *Journal of Materials Science*, **48**, 7949–7959.

Schott, H. (1992) Swelling kinetics of polymers. *Journal of Macromolecular Science Part B – Physics*, **31**, 1–9.

Spagnol, C., Rodrigues, F.H.A., Pereira, A.G.B., Fajardo, A.R., Rubira, A.F., and Muniz, E.C. (2012) Superabsorbent hydrogel nanocomposite based on starch-g-poly (sodium acrylate) matrix filled with cellulose nanowhiskers. *Cellulose*, **19**, 1225–1237.

Stojakovic, D., Milenkovic, J., Daneu, N., and Rajic, N. (2011) A study of the removal of copper ions from aqueous solution using clinoptilolite from Serbia. *Clays and Clay Minerals*, **59**, 277–285.

Wang, A. and Zhang, J.P. (2006) *High-Absorption Resin Composed of Organic and Inorganic Materials*. Science Press, Beijing.

Wang, C.Y., Zhou, J.T., He, J.K., Hao C.S., Pan Y.Z., and Meng, C.G. (2012) Synthesis of zeolite A and its application as a high-capacity cadmium ion exchanger. *Chinese Journal of Catalysis*, **33**, 1862–1869.

Wang, M.S., Liao, L.B., Zhang, X.L., Li, Z.H., Xia, Z.G., and Cao, W.D. (2011) Adsorption of low-concentration ammonium onto vermiculite from Hebei province, China. *Clays and Clay Minerals*, **59**, 459–465.

Wang, S.G., Gong, W.X., Liu, X.W., Gao, B.Y., Yue, Q.Y., and Zhang, D.H. (2006) Removal of fulvic acids from aqueous solutions via surfactant modified zeolite. *Chemical Research in Chinese Universities*, **22**, 566–570.

Weaver, M.O., Bagley, E.B., Fanta, G.F., and Doane, W.M. (1976) Highly absorbent starch-containing polymeric compositions. US Patent 3.981.100.

Zdanowicz, M., Schmidt, B., and Spychaj, T. (2010) Starch graft copolymers as superabsorbents obtained via reactive extrusion processing. *Polish Journal of Chemical Technology*, **12**, 14–17.

Zhang, J., Li, A., and Wang, A. (2006) Study on superabsorbent composite. VI. Preparation, characterization and swelling behaviors of starch phosphate-graft-acrylamide/attapulgite superabsorbent composite. *Carbohydrate Polymers*, **65**, 150–158.

Zhang, X.L., Li, Y.H., Hao, P.P., and Yang S. (2011) Research on synthesis and performance of water preserver starch-grafted acrylic acid/zeolite/fly ash. *Journal of Anhui Agricultural Science*, **39**, 3–5.

Zhou, B., Liao, R.K., Li, Y.K., Gu, T., Yang, P.L., Feng, J.,Xing, W.M., and Zou, Z.C. (2012) Water-absorption characteristics of organic–inorganic composite superabsorbent polymers and its effect on summer maize root growth. *Journal of Applied Polymer Science*, **126**, 423–435.

Zhou, J.P., Qiu, K.Q., and Fu, W.L. (2005) The surface modification of ZnO and its effect on the mechanical properties of filled polypropylene composites. *Journal of Composite Materials*, **39**, 1931–1941.

Zwingmann, N., Mackinnon, I.D.R., and Gilkes, R.J. (2011) Use of a zeolite synthesized from alkali treated kaolin as a K fertiliser: Glasshouse experiments on leaching and uptake of K by wheat plants in sandy soil. *Applied Clay Science*, **53**, 684–690.

(*Received 1 March 2014; revised 20 June 2014; AE: S.M. Kuznicki; Ms. 854*)

Clays and Clay Minerals, Vol. 62, No. 3, 224–234, 2014.

METHODS FOR *IN SITU* SIMS MICROANALYSIS OF BORON AND ITS ISOTOPES IN PALAGONITE

BRUCE D. PAULY[1]*, LYNDA B. WILLIAMS[2], RICHARD L. HERVIG[2], PETER SCHIFFMAN[1], AND ROBERT A. ZIERENBERG[1]

[1] Department of Geology, University of California, Davis, California 95616-5270, USA
[2] School of Earth and Space Exploration, Arizona State University, Tempe, Arizona 85287-1404, USA

Abstract—Boron has been shown to be a useful trace element in clay-mineralization reactions, raising the possibility that B studies may provide a means to investigate environmental controls on palagonitization. The objective of the present study was to address calibration, matrix effects, and B exchangeability issues such that meaningful secondary ion mass spectrometry (SIMS) microanalysis of B in thin sections of palagonite will be feasible. Silver Hill illite (IMt-1) was found to be a suitable calibration reference material, based on compositional similarity, relatively high B content, and ease of mounting on thin-section samples for SIMS microanalysis. Matrix effects of borated sideromelane and illite were compared and found to be similar, confirming previous studies which showed no matrix effects for B among minerals. Boron substitutes for Si in tetrahedral sites and also can be adsorbed in exchangeable sites of 2:1 clay minerals. Similarly, B can be found in tetrahedral and exchangeable sites within palagonite, which consists of both layered and amorphous volumes. In order to measure tetrahedral B content and isotopic ratio in the palagonite, exchangeable B was removed by soaking sample thin sections in a 1 M NH_4Cl solution until exchangeable cation concentrations were constant. Treated samples showed decreases in B content and isotopic ratio with exchange. Extraction of exchangeable B permits the direct measurement of tetrahedral B content and isotopic ratio. The exchange technique devised and tested here should have broad applicability to thin-section microanalysis of B in clay and clay-like materials where cation exchange can be used for surface-analytical techniques. The present study represents an initial attempt to address sample-preparation, calibration, and potential matrix-effects problems for analyses by SIMS. Further refinements may improve the accuracy of the measurements, but the results presented here indicate that meaningful measurements are possible.

Key Words—B content, B exchangeability, B isotopes, Boron, Palagonitization, Sideromelane, SIMS, Thin Section.

INTRODUCTION

Sideromelane (basalt glass) is a thermodynamically unstable material which, in aqueous, low-temperature environments, can undergo a geochemical alteration process known as ''palagonitization'' (Fisher and Schmincke, 1984). Palagonitization is a hydrolytic alteration process during which sideromelane is dissolved and hydrated by water, forming palagonitized sideromelane (referred to hereafter as palagonite). Concurrent with dissolution and hydration of sideromelane is the precipitation (to varying extents) of authigenic minerals, mainly smectites and zeolites (Stroncik and Schmincke, 2001; Walton and Schiffman, 2003; Pauly *et al.*, 2011); see Figure 1. Palagonitization is a globally significant process, with broad geological implications for volcano-edifice stability (Schiffman *et al.*, 2006), nuclear-waste storage (Zielinski, 1980; Jercinovic *et al.*, 1990; Crovisier *et al.*, 2003), and Martian crustal evolution (Bishop *et al.*, 2002). The factors controlling palagonitization are still not well understood, however.

* E-mail address of corresponding author:
bdpauly@ucdavis.edu
DOI: 10.1346/CCMN.2014.0620306

Palagonite is regarded as the initial sideromelane replacement product during hydrolytic alteration, the ultimate fate of palagonite being conversion to smectite (Stroncik and Schmincke, 2001; Pauly *et al.*, 2011). Many early workers (Hay and Iijima, 1968a; Singer, 1974; Eggleton and Keller, 1982; Zhou and Fyfe, 1989) suggested that palagonite has a smectite-like structure. Palagonite appears to be amorphous to poorly crystalline when examined using X-ray diffraction on hand-separated palagonites (Stroncik and Schmincke, 2001). High-resolution transmission electron microscopy (HRTEM) images of a palagonite sample (Drief and Schiffman, 2004) show the existence of both amorphous material and poorly crystalline sheeted material with variable layer stackings (Figure 2). Currently, palagonite is considered to be a metastable proto-smectite replacement product of sideromelane (Pauly *et al.*, 2011).

Palagonite is commonly observed rimming sideromelane fragments in hyaloclastites (Figure 1). These palagonitized rinds are friable and generally <100 μm thick; isolating palagonite completely from fresh sideromelane is extremely difficult, therefore. An advantage of using *in situ* micro-analytical methods to study palagonite is the ability to analyze palagonite and co-existing fresh sideromelane in its textural/petrologic

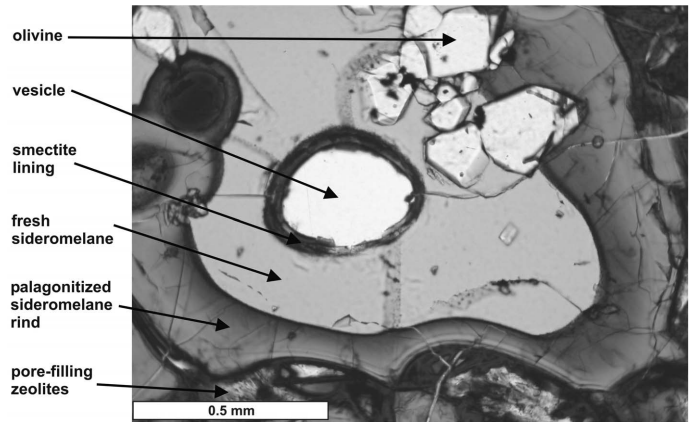

Figure 1. Thin-section photomicrograph (plane-polarized light) of sample R0777-17.4, palagonitized hyaloclastite from the Hawaii Scientific Drilling Project (Mauna Kea volcano, SE flank). A single vesiculated sideromelane fragment is shown. Palagonitization has created a dark altered rind (palagonite) around the lighter fresh sideromelane, a smectite lining within the clear vesicle, and pore-filling zeolites as shown.

context. Electron probe microanalysis (EPMA) has been used for many years to characterize the *in situ* major-element composition of palagonite (Stroncik and Schmincke, 2001; Pauly *et al.*, 2011 and references therein). Laser-ablation inductively coupled plasma mass spectroscopy (LA-ICP-MS) has been used to determine the *in situ* trace-element composition of palagonite samples (Walton *et al.*, 2005; Walton and Schiffman, 2003; Pauly *et al.*, 2011). With these studies as a foundation, a logical next step would be to carry out an *in situ* trace-element study in order to evaluate the geochemical-process controls on palagonitization.

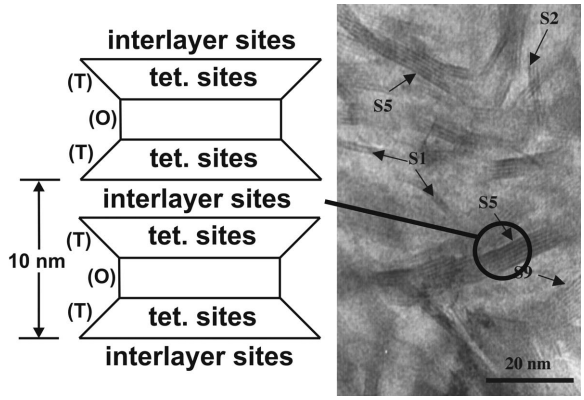

Figure 2. HRTEM lattice-fringe image of the palagonitized portion of sample R0777-17.4 (see Figure 1). Layered intervals, showing different layer stackings (*e.g.* S2 = two layers of 1 nm each), are visible, consistent with previous workers' suggestions that palagonite resembles smectite (see text). Amorphous intervals are also distinguishable. Bubble and schematic enlargement (this study) show tetrahedral (tet.) and interlayer sites for B occupancy within the smectite-like areas (image after Drief and Schiffman, 2004). Interlayer sites dominate cation exchange in smectite-groups minerals, but exchange may also occur at sites (*e.g.* edge sites) in addition to interlayer sites.

Elements having stable isotopes that fractionate during geochemical processes have been used successfully as tracers of geochemical processes (Hoefs, 2004; Lerman and Clauer, 2007). By definition, $\delta^{11}B$ (‰) = $((^{11}B/^{10}B_{sample})/(^{11}B/^{10}B_{standard})-1) \times 1000$; the standard used in most studies is NIST-SRM 951 boric acid (Palmer and Swihart, 1996). Substantial ^{11}B enrichment in seawater ($\delta^{11}B$ ~+40‰; Hoefs, 2004) relative to sideromelane ($\delta^{11}B$ −10 to 0‰; Hoefs, 2004) has been attributed to isotopic fractionation that occurs as ^{10}B is incorporated by clay minerals during low-temperature alteration of oceanic crust (Hemming and Hanson, 1992). The B isotopic system is not affected by changes in oxidation state, and it has a known dependence on fluid composition and temperature (Williams *et al.*, 2012). These factors suggest that B may be useful as a trace element for studying palagonite-water fractionation during palagonitization.

Boron has two stable isotopes, ^{10}B (~19%) and ^{11}B (~81%). Isotope systematics (Palmer and Swihart, 1996) indicate that ^{11}B is concentrated into trigonal coordination sites, and ^{10}B is concentrated into tetrahedrally coordinated sites. The relative distribution of $B(OH)_4^-$ and $B(OH)_3$ in aqueous solutions is controlled by pH (Hemming and Hanson, 1992), with $B(OH)_3$ dominant at pH <8 (Palmer and Swihart, 1996) at 25ºC. The tetrahedral sheet of clay minerals will thus incorporate ^{10}B preferentially in the tetrahedral sites (Palmer and Swihart, 1996, and references therein), unless the fluid has a high pH at which tetrahedral borate anion dominates the fluid phase. This raises the possibilities that, similar to clay minerals such as smectite, B can substitute into tetrahedral sites within the layered intervals, and that B isotopic fractionation between palagonite and water can occur during palagonitization.

Secondary ion mass spectrometry (SIMS) has been shown to be useful for routine B microanalyses (content

and isotopic ratio) of minerals and glasses (Hervig, 1996). The analysis of palagonite by SIMS has not been attempted previously, although SIMS has been used successfully to analyze B in clay minerals (Williams *et al.*, 2012 and references therein). These recent studies are of particular relevance to the present study due to the apparent similarities described above between palagonite and smectite (Figure 2). As a prerequisite to performing similar studies of palagonitization, in the present study methods were tested for conducting reproducible *in situ* SIMS microanalyses of B and its isotopes in polished thin sections of palagonite.

Expandable clay minerals such as smectite normally have a negative charge on their basal siloxane surface due to cation substitutions in the silicate framework. In a simple model, the basal siloxane surface attracts cations, which occupy the sites labeled 'interlayer sites' in Figure 2; some cation exchange at other sites is also possible. However, Brindley and Brown (1980) found that neutral as well as negatively charged species are held in the interlayers of illite-smectite, raising the possibility that both of the dominant aqueous B species (neutral $B(OH)_3$ as well as negatively charged $B(OH)_4^-$) could be held in interlayer sites. Based on infrared spectroscopy work (Moore and Reynolds, 1991; Sposito *et al.*, 1991), cations attracted to the basal siloxane surfaces are hydrated, so neutral $B(OH)_3$ may be introduced and incorporated with the water. Because B trapped in exchangeable sites may not be in equilibrium with B in the silicate framework (Williams *et al.*, 2007), the isotopic composition of tetrahedrally bound B (substituted for Si) and exchangeable B must be separated (Williams and Hervig, 2006). According to Zhang *et al.* (1998) and Williams and Hervig (2005) adsorbed B could can be removed from exchangeable sites of bulk smectite separates using a concentrated 1 M NH_4Cl solution. Using major-element composition as analyzed by EPMA, Schiffman and Southard (1996) showed that cations can be exchanged in thin-section samples of both smectite and palagonite using a CsCl solution. As part of the present study, an experiment was performed on palagonite thin sections to determine if adsorbed B can be removed from exchangeable sites of the sample using NH_4Cl solution.

ANALYTICAL METHODS

SIMS

Analytical conditions. In situ B content and $\delta^{11}B$ were analyzed using a Cameca ims 3f SIMS at the Arizona State University SIMS Facility (Hervig, 1996; http://sims.asu.edu). Each analysis used an O^- primary beam current of 3−5 nA. The analyses were done in spot mode for high spatial resolution (10 μm craters), and the sample was pre-sputtered for 5 min to remove any remaining surface contaminants and achieve stable secondary ion signals. The primary beam voltage was −12.5 kV with a sample voltage of −4500 V for a total impact energy of ~17 keV. The SIMS was operated at a mass resolving power (MRP) of ~1200 (MRP = mass/Δmass at 10% peak width), sufficient to separate the $^{10}BH^+$ species from $^{11}B^+$, and ions with ~20±20 eV initial kinetic energy were allowed into the mass spectrometer. Energy filtering (secondary ions with 75±20 eV initial kinetic energy) was used for B-content analyses (Hervig, 1996). Measurements were made on the major B isotope ^{11}B, which is four times more abundant than the minor isotope ^{10}B, and normalized to ^{30}Si, a minor isotope of Si, selected to keep the ions detected on the same electron multiplier used to count the ^{11}B. Boron content was determined using a well established calibration curve (Williams *et al.*, 2012) based on analyses of various minerals and glasses (NIST standards) with certified B contents. The B-content analyses were run for long enough (10−15 min) to acquire sufficient counts for errors to be <10%. The actual time depended on the amount of B in each sample. The analytical errors were compared with predicted errors (from counting statistics) and if the analytical error was more than twice the predicted error, the analysis was evaluated for potential charging or other instrumental instability. Analyses that did not agree closely with the predicted errors were disregarded, but such analyses were useful as warning signs of an instrumental setup problem (charging) or aging electron multiplier.

After analysis of the B content, analyses of $^{11}B/^{10}B$ ratio were made in the same analytical crater. Energy filtering was not used for B-isotope ratio analysis, but rather entrance and exit slits were adjusted to the appropriate MRP. The isotope-ratio analyses must be far more precise than trace-element analyses. Here users normally count for 2 s on ^{11}B and 8 s on the less abundant ^{10}B. For this study 100 cycles were measured, but where B contents were small the number of cycles was increased to improve statistics. The total analysis time for each sample depended on the number of cycles. Again the standard error (standard deviation from the average/square-root 100, where 100 measurements were made) was compared to the predicted error based on total number of ion counts, to determine the statistical significance of results.

Reference material for calibration. Ideally the reference material would be mineralogically identical to the unknown sample, so that matrix effects on SIMS analyses of both materials would also be identical. Because of the natural variability of palagonite, however, like clay minerals, defining and characterizing a reference material composed of palagonite is not possible. Phases with similar chemistry to palagonite (smectite and illite) were tested as potential reference materials. An advantage of using a clay mineral as a reference material is that a drop of a dilute clay mineral

suspension can be applied directly onto polished thin sections, where it then orients clay particles flat as it dries, a requirement for SIMS analysis. The on-sample location of the reference material allows the instrumental mass fractionation (IMF) to be determined readily between analyses of the unknown materials without having to exchange samples and disturb the vacuum. This 'bracketing' of reference material analyses between unknown analyses is critical for assessing instrumental stability during analytical sessions.

Natural illite and smectite were evaluated as potential reference materials. SWy-1 smectite (Crook County, Wyoming, from the Source Clays Repository of The Clay Minerals Society) was tested but was not selected as a reference material for this study because of the possibility of large analytical errors due to its relatively small B content. Illite IMt-1 (Silver Hill, Montana, also from the Source Clays Repository) was tested and selected for use. IMt-1 has a relatively large B content (240±20 ppm; Williams *et al.*, 2001), with B located in the silicate tetrahedral sites, similar to palagonite (Figure 2), and it has also been analyzed previously (Williams *et al.*, 2001) for isotopic composition using both positive and negative thermal-ion mass spectrometry (TIMS).

Matrix effects. Because the proposed reference material (IMt-1) does not have identical chemistry to the palagonites of interest, the difference between measured B isotope ratios for IMt-1 and a synthetically borated basalt glass, estimated to represent the initial composition of the material subsequently palagonitized, was examined closely. A borated basalt with 2300 ppm B (BB-1), was synthesized using glassy basalt from the Juan de Fuca ridge (sample TT-152 of Hervig *et al.*, 2002) and NIST-SRM 951 boric acid; synthesis details were given by Hervig *et al.* (2002). Because BB-1 was doped with 2300 ppm NIST standard boric acid (SRM 951), its isotopic composition is 0‰ by definition. No significant change of the B content in BB-1 was noted (Hervig *et al.*, 2002) during melt-aqueous solution fractionation experimental runs at 950−1100ºC and 110−170 MPa; no change in isotopic composition of BB-1 during initial preparation was expected, therefore. The B content and $\delta^{11}B$ of IMt-1 has been analyzed using both TIMS and SIMS and has given consistent isotopic ratios over the past 15 years (Williams *et al.*, 2012). Boron isotopic ratios are reported relative to NIST 951 boric acid, and the IMt-1 internal reference was used to determine the instrumental mass fractionation (IMF) during each analytical session. Three SIMS analyses of IMt-1 were followed by five analyses of BB-1 and three further analyses of IMt-1 during a single SIMS session (Table 1). The SIMS analyses were compared to the average of five TIMS analyses of IMt-1 (bulk $\delta^{11}B = -9.1\pm0.6$‰, determined independently by TIMS; Williams *et al.*, 2001).

The SIMS instrumental fractionation (α_{inst}) was calculated by taking the ratio of the $^{11}B/^{10}B$ measured by SIMS of the reference material (IMt-1) divided by the $^{11}B/^{10}B$ ratio measured by TIMS. The SIMS measurement on BB-1 was then corrected by dividing the raw isotope ratio by α_{inst}. The δ value was then calculated using standard notation relative to the accepted standard for B which is NIST SRM 951 boric acid with a certified $^{11}B/^{10}B$ ratio of 4.0437 (Catanzaro *et al.*, 1970):

$$\text{Raw } (^{11}B/^{10}B) \,/\, \alpha_{inst} = \text{corrected ratio}$$
$$\delta^{11}B‰ = ((\text{corrected ratio}/4.0437)^{-1}) \times 1000$$

The IMF based on independent analyses of IMt-1 averaged −40.7±0.4‰ (1σ S.E. of six analyses) over the analytical session (Table 1). If no matrix effects for analysis of the illite *vs.* glass were found, the same IMF (or α_{inst} correction) should give the correct isotopic ratios for both materials. Five analyses of BB-1, corrected by the α_{inst} determined using IMt-1 are listed in Table 1. The average value is −0.9±0.6‰ (1σ), which is within error of 0‰ ($\delta^{11}B$ of NIST 951 boric acid standard) and suggests that any matrix effects are at the sub-permil level. This finding is consistent with other studies. No matrix effects for B measurements by SIMS were found (Hervig *et al.*, 2002) when analyzing basalt and rhyolite glasses, metamorphic minerals, and diagenetic materials. No appreciable matrix effects between rhyolite and basalt were noted either (Rosner *et al.*, 2008). Boron isotopic analyses of various clay minerals were compared with different mineral standards and NIST standards and no matrix effects for B were found (Williams *et al.*, 2001). In addition, the instrumental drift over the analytical session was also found to be at sub-permil levels (Table 1).

Electron probe microanalysis (EPMA)

The *in situ* major-element composition of palagonite was determined using a Cameca SX-100 electron microprobe at the University of California, Davis. A conductive C-coating ~250 Å thick was applied to the samples prior to analysis. The electron-beam settings were 15 KeV accelerating voltage with 2 nA regulated current, and the beam was rastered over a 5 μm × 5 μm area. Peaks and backgrounds were typically counted for 10 s. Net intensities relative to oxide and silicate calibration standards were converted to concentrations using standard ZAF correction techniques (Schiffman and Roeske, 2002). Accuracy was evaluated by analyzing working reference standards as unknowns under the same analytical conditions.

Samples

In order to assess palagonite B composition variability, eight samples of palagonitized hyaloclastite representing three palagonitization environments (submarine volcaniclastic, seafloor volcanic, and marine phreatomagmatic) were selected for this study. These

Table 1. $\delta^{11}B$ analyses of borated basalt glass (BB-1) by SIMS using IMt-1 as the reference material. BB-1 analyses were pre- and post-bracketed with IMt-1 analyses to monitor and calculate average instrumental mass fractionation (IMF) during BB-1 analyses.

	SIMS measurements					Calculated Values	
Sample	$^{11}B/^{10}B$	S.E. (ratio)	raw $\delta^{11}B$ (‰)	S.E. (‰)	$\alpha_{inst.}$	corrected $^{11}B/^{10}B$	corrected $\delta^{11}B$ (‰)
IMt-1	3.8453	0.0029	−49.1	0.8	0.9597	4.0069	−9.1
	3.8435	0.0026	−49.5	0.7	0.9592	4.0069	−9.1
	3.8398	0.0030	−50.4	0.8	0.9583	4.0069	−9.1
Average	3.8429		−49.7		0.9591	4.0069	
Std. Dev.	0.0028		0.7		0.0007		
BB-1	3.8722	0.0013	−42.4	0.3		4.0377	−1.5
	3.8772	0.0015	−41.2	0.4		4.0430	−0.2
	3.8751	0.0013	−41.7	0.3		4.0408	−0.7
	3.8733	0.0016	−42.1	0.4		4.0389	−1.2
	3.8790	0.0015	−40.7	0.4		4.0448	+0.3
Average	3.8754						−0.9
Std. Dev.	0.0028						0.6
IMt-1	3.8479	0.0028	−48.4	0.7	0.9603	4.0069	−9.1
	3.8396	0.0022	−50.5	0.6	0.9582	4.0069	−9.1
	3.8389	0.0027	−50.6	0.7	0.9581	4.0069	−9.1
Average	3.8421				0.9589		
Std. Dev.	0.0050				0.0012		
IMt-1: Session							
Average	3.8432		−49.8		0.9590		
Std. Dev.	0.0037		0.9		0.0009		

S.E. = standard error
$\alpha_{inst.}$ = SIMS $^{11}B/^{10}B$ / TIMS $^{11}B/^{10}B$
Corrected $^{11}B/^{10}B$ = measured ratio / $\alpha_{inst.}$
Bulk $\delta^{11}B$ measured using TIMS (positive and negative; n = 5) (Williams *et al.*, 2001):

$^{11}B/^{10}B$	S.E. (ratio)	$\delta^{11}B$ (‰)	S.E. (‰)
4.0069	0.0024	−9.1	0.6

samples were described by Pauly *et al.* (2011). Boron is a ubiquitous contaminant in nature, common in water and airborne particles and it can easily contaminate lab samples, therefore. A major issue with any trace-B analytical study is the prevention of B contamination during sample handling. Great care was taken, therefore, during this experiment, to avoid sample contact with B-bearing lab materials such as borosilicate glass lab ware, unfiltered water, and dust.

One-inch (25.4 mm) diameter, 100 μm-thick, polished sections of each sample were prepared. A ~30 nm gold coating was applied to each sample, and then the B content and $\delta^{11}B$ were analyzed using SIMS as described above at selected spots within palagonitized areas on all eight samples. Exact analysis-spot locations were recorded photographically. Two of the eight samples, with relatively wide palagonitized rims, were chosen for cation-exchange experiments allowing evaluation of the potential for quantitative removal of exchangeable B from thin-sectioned palagonite. Both samples were analyzed for major-element composition using EPMA as close as possible to the previously recorded analytical craters. The C coat required for EPMA was removed by polishing. The samples were then rinsed with nominally B-free distilled, de-ionized water that had been filtered through an Amberlite resin column (Tonarini *et al.*, 1997), then washed with 0.1 M mannitol, a polyhydric alcohol which has been shown to bind and remove adsorbed B contaminants from exterior mineral surfaces (Hingston, 1964; Tonarini *et al.*, 1997; Williams *et al.*, 2001). Both samples were then soaked in a 1 M NH_4Cl exchange solution (prepared using B-free distilled, de-ionized water and 99.7% pure NH_4Cl) for 20 h. The samples were then re-analyzed using EPMA at the same spots (relocated as precisely as possible using back scattered electron images) as had been analyzed previously. These steps were repeated as necessary until a steady-state elemental composition of major exchangeable cations (Na, K, and Ca) was reached. Because neither of the major aqueous B species is a cation, the total soak duration required for complete Na, K, and Ca exchange was assumed to be greater than or equal to the total soak time required for complete B exchange. The other six samples were then soaked in 1 M NH_4Cl for the determined soak duration.

Table 2. Effect of soaking polished thin sections on palagonite major-element composition (EPMA measurements). The averages of four analyses prior to soaking and after three successive 20-h exposures to NH_4Cl solutions are shown for two different samples. The purpose of this process was to remove B from the palagonite exchangeable sites. These data are summarized in Figure 3.

Sample	Cum. soak Time (h)	SiO_2	Al_2O_3	TiO_2	FeO	MnO	MgO	CaO	Na_2O	K_2O	P_2O_5	Total
		Wt.% oxide										
R0777-17.4	0	42.13	7.94	4.69	14.56	0.09	1.87	9.47	0.88	0.58	0.11	82.35
R0777-17.4	20	47.70	8.64	5.49	16.95	0.06	2.14	4.91	0.03	0.05	0.10	86.10
R0777-17.4	40	48.90	8.33	5.48	17.09	0.19	2.14	4.25	0.06	0.04	0.06	86.62
R0777-17.4	60	48.31	8.66	5.43	16.64	0.12	2.25	4.00	0.05	0.02	0.12	85.61
S708-9	0	38.81	8.51	4.04	16.72	0.10	2.75	5.10	2.35	1.19	0.10	79.76
S708-9	20	42.66	9.40	4.24	18.05	0.10	2.73	3.97	0.23	0.09	0.07	81.64
S708-9	40	44.09	9.51	4.32	18.74	0.12	2.65	3.60	0.06	0.03	0.06	83.30
S708-9	60	44.63	9.64	4.16	18.83	0.13	2.50	3.62	0.14	0.09	0.07	83.90

All eight samples were then rinsed and washed as above. IMt-1 was re-applied to the samples as a B reference material, the sections were re-coated with ~30 nm of gold, and palagonitized areas of the samples were then re-analyzed for B content and $\delta^{11}B$ using SIMS at the same spots as had been analyzed previously.

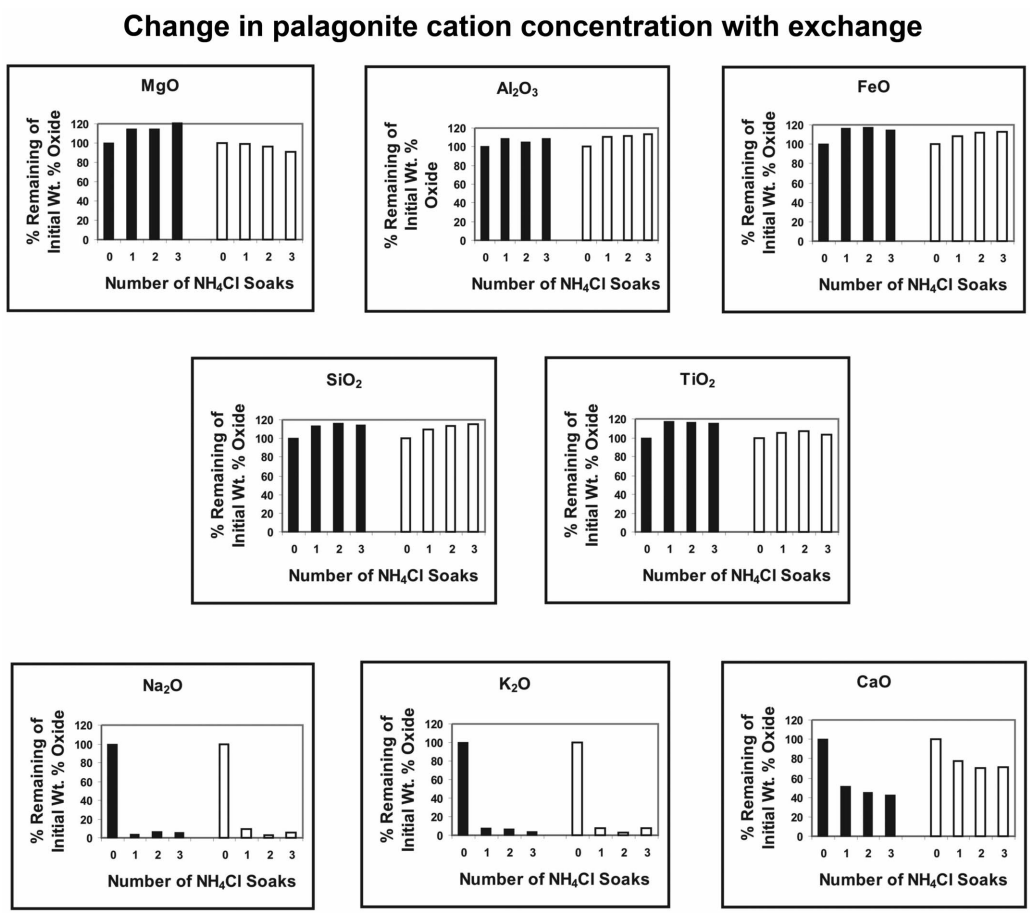

Figure 3. Percentage of original cation concentration remaining after exchange with 1 M NH_4Cl solution. Shaded bars are for sample R0777-17.4; non-shaded bars are for sample S708-9. Soak 0 values are pre-exchange (100%), shown for reference. The duration of each soak was 20 h. Al, Fe, Si, and Ti do not appear to have exchanged. Na and K concentration decreased relatively rapidly to essentially steady state with the first soak. Ca concentration decreased more slowly, reaching steady state with two soaks.

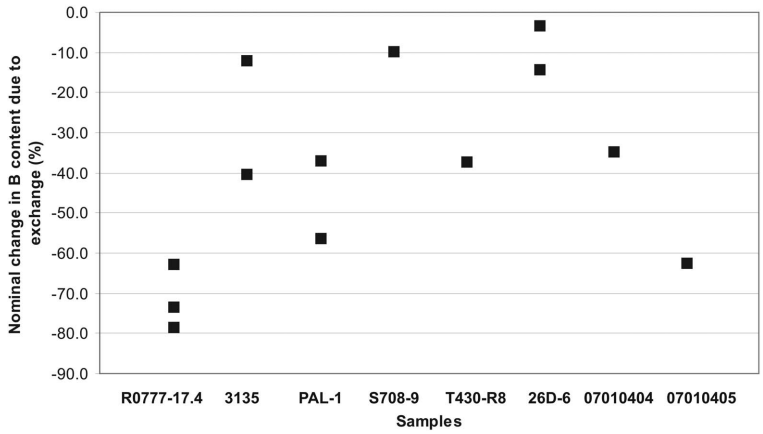

Figure 4. Nominal percentage change in B content (bulk minus tetrahedral) due to cation exchange for eight palagonite samples (the measured pre-and post-exchange B-content measurements are accurate within ±10%; see Table 3). The B content decreased for all samples; the percentage decrease was very variable over the sample set.

RESULTS

Major-element analyses (EPMA) for the two samples subjected to three 20-h soaks in 1 M NH_4Cl are summarized in Table 2 and changes in major exchange-cation chemistry with increasing exposure time is illustrated in Figure 3. The concentrations of framework cations were unchanged with NH_4Cl soak, as was Ti, demonstrating that no dissolution of glass occurred during the cation-exchange treatments. Concentrations of cations expected to occupy exchangeable sites (Na, K, Ca) decreased with increasing NH_4Cl treatment time. The Na and K concentrations declined dramatically and reached steady state during the first 20 h of treatment (essentially no change with the subsequent soaks); Ca concentration declined more slowly, reaching steady state during the second 20-h soak (essentially no change with the third 20 h treatment).

The measured pre- and post-exchange B content and $\delta^{11}B$ values are listed in Table 3. The B-content values decreased with NH_4Cl soak for all eight palagonite thin-section samples in the present study. The measured decrease in B content ranged from 3.1 to 78.1% of the original value (Figure 4). The $\delta^{11}B$ values also decreased with NH_4Cl treatment for all eight polished sections. The measured decrease in $\delta^{11}B$ values ranged from 1.9 to 27.9‰ (Figure 5).

DISCUSSION

Exchange-soak duration

The unchanged concentrations of Mg, Al, Fe, Si, and Ti with NH_4Cl exchange treatment (Table 2, Figure 3) confirm that these cations were all structurally bound and that no dissolution of the glass occurred. The significant decrease in the concentration of Na, K, and Ca indicate that these cations were held weakly in exchangeable sites of the palagonite. Neutral boric acid and negative borate anion, the two dominant aqueous B species, were similarly removed by the exchange solution (Table 3). The rapid decline in Na and K

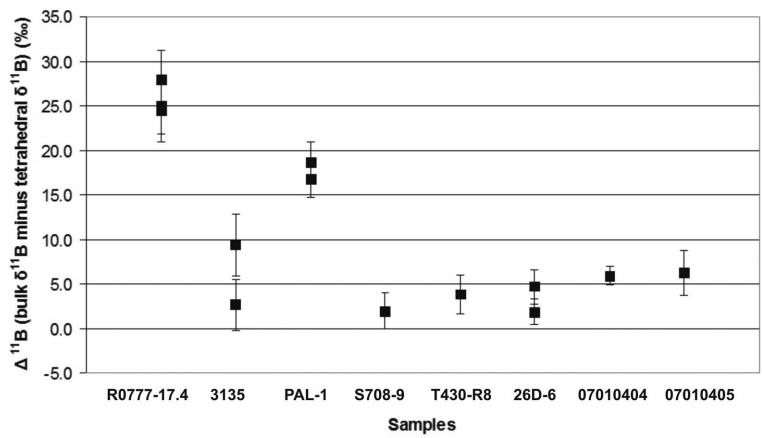

Figure 5. Change in $\delta^{11}B$ (bulk minus tetrahedral) due to cation exchange for eight palagonite samples (see Table 3). $\delta^{11}B$ decreased for all samples; the magnitude of the decrease was very variable over the sample set.

Table 3. Measured palagonite B content and $\delta^{11}B$ for the eight samples in the present study. Calculated changes in B content and $\delta^{11}B$ due to the cation exchange procedure are summarized in Figures 4 and 5, respectively.

Sample	Analysis	Measured Pre-exchange B content (ppm)	Measured Pre-exchange B content error, ±	Measured Post-exchange B content (ppm)	Measured Bulk B content minus Post-exchange B content error, ±	Calculated Bulk B content minus Tetrahedral B content (ppm)	Calculated Tetrahedral B content Error, ± (ppm)	Measured Pre-exchange $\delta^{11}B$ (‰)	Measured Pre-exchange S.E. (‰)	Measured Post-exchange $\delta^{11}B$ (‰)	Measured Post-exchange S.E. (‰)	Calculated $\Delta^{11}B$ (‰)	Calculated $\Delta^{11}B$ Error, ± (‰)
R0777-17.4	a	56	10%	15	10%	41	7.1	+17.3	1.1	-7.8	2.2	25.1	3.2
	b	40	10%	15	10%	25	5.5	+24.6	1.1	-3.3	2.2	27.9	3.3
	c	64	10%	14	10%	50	7.8	+20.4	1.1	-4.1	2.5	24.5	3.5
3135	a	17	10%	15	10%	2	3.2	+19.9	1.5	+10.5	2.0	9.4	3.5
	b	20	10%	12	10%	8	3.2	+16.6	1.2	+13.9	1.6	2.7	2.8
PAL-1	a	82	10%	36	10%	46	11.8	+35.6	1.0	+18.8	1.0	16.8	2.0
	b	71	10%	45	10%	26	11.6	+31.8	1.2	+13.1	1.1	18.7	2.3
S708-9	a	83	10%	75	10%	8	15.8	+36.1	0.9	+34.1	1.1	2.0	2.0
T430-R8	a	81	10%	51	10%	30	13.2	+9.7	0.9	+5.8	1.3	3.9	2.2
26D-6	a	255	10%	219	10%	36	47.4	-2.4	0.6	-4.3	0.9	1.9	1.5
	b	196	10%	190	10%	6	38.6	+7.6	0.9	+2.9	1.1	4.7	2.0
07010404	a	586	10%	384	10%	202	97	–0.9	0.6	-6.9	0.6	5.9	1.1
07010405	a	61	10%	23	10%	38	8.4	+5.7	1.0	-0.6	1.5	6.3	2.5

S.E. = Standard error
$\Delta^{11}B$: pre-exchange $\delta^{11}B$ (bulk $\delta^{11}B$) minus post-exchange $\delta^{11}B$ (tetrahedral $\delta^{11}B$)

concentrations with NH_4Cl exchange is consistent with relatively weak bonding in exchangeable sites due to the hydrated radius/charge ratio of these cations. Because the decreasing Ca concentration did not reach steady state until some point during the second 20-h exchange treatment, in order to be conservative, the soak duration in 1 M NH_4Cl assumed to be required for complete B exchange in the upper ~2.3 μm (Potts, 1987) of exposed surface, was 60 h. This method for exchangeable B extraction should be applicable to thin-section samples of sheet silicates and other clay-like minerals.

Significance of pre- and post-exchange B measurements

Determination of pre-exchange (bulk) and post-exchange (tetrahedral) B content and isotopic ratio allows the exchangeable B content and isotope ratios to be calculated by mass balance. In particular, the exchangeable B may not be in equilibrium with the B in the tetrahedral sheet, and this B may have a large influence on the bulk $\delta^{11}B$ analysis (Figure 5). The $\delta^{11}B$ of B in the tetrahedral sites of the palagonite ($\delta^{11}B_{tet}$) depends on temperature and the relative abundances of the two aqueous B species $^{10}B(OH)_4^-$ and $^{11}B(OH)_3$, which in turn depend on pH (Hemming and Hanson, 1992). Assuming a temperature, therefore, allows the composition of the fluid associated with palagonitization to be inferred from $\delta^{11}B_{tet}$ using the calibrated B-isotope fractionation equation for conditions of low pH (Williams *et al.*, 2007). This fractionation does not apply to high-pH conditions where $B(OH)_4^-$ dominates the fluid. Exchangeable B isotopic ratios ($\delta^{11}B_{ex}$) potentially give an indication of the most recent fluid composition, although $\delta^{11}B_{ex}$ values do not necessarily reflect $\delta^{11}B$ values of water in equilibrium with the silicate but rather fluids introduced after the initial stages of illitization (Williams *et al.*, 2007). Such isotopic differences may also be useful for the interpretation of changes in the B-isotope composition of palagonites and associated fluids over time due to changing environmental conditions (*e.g.* influx of meteoric or hydrothermal fluids into a previously seawater-dominated system) during palagonitization.

The wide variability in B content and $\delta^{11}B$ values (Table 3) suggests that future research could determine the significance of the variations, and how they are attributable to palagonitization conditions such as fluid composition, temperature, *etc*. For example, although samples R0777-17.4, PAL-1, 3135, and S708-9 are all from submarine volcaniclastic settings (Pauly *et al.*, 2011), $\delta^{11}B_{tet}$ values for these samples vary by nearly 40‰, suggesting that local chemical variables, more than temperature, affected palagonitization.

Evaluation of methods developed

The B-exchange and SIMS calibration methods for characterization of B content and isotopic composition of palagonite samples presented here provide a basis for analysis so long as care is taken to show that matrix effects are not a concern. Matrix effects have been noted between glass and minerals (Chaussidon and Jambon, 1994), and these methods may not be appropriate for palagonites formed from glasses not compositionally similar to the BB-1 glass used in this study. Because palagonite is no longer a glass and not yet a clay mineral, well established methods for measuring B isotopes in glass and clay minerals can serve only as guidance. This manuscript documents the first attempt at such measurements and will hopefully stimulate future work to improve and refine these methods.

CONCLUSIONS

(1) Use of IMt-1 (Silver Hill illite, <2 μm fraction) from the Source Clays Repository as a reference material allowed accurate SIMS analyses for B and its isotopes in both basaltic glass, the precursor of palagonite, and palagonitized intervals of eight samples. The B content and isotopic ratios measured in palagonite using IMt-1 as the reference material have a precision of <10% and ±2.5‰, respectively.

(2) Concentrations of Na, K, and Ca (occupying exchangeable sites) in two thin-section samples of palagonite decreased significantly after exchange with a 1 M NH_4Cl solution, indicating that these cations exchanged with NH_4^+. Of the three cation concentrations monitored using EPMA, Ca decreased most slowly, and reached steady state during the second 20-h soak.

(3) SIMS measurements of bulk B content, tetrahedral B content, bulk $\delta^{11}B$, and tetrahedral $\delta^{11}B$ showed that the B content and $\delta^{11}B$ of palagonite changed significantly after 60 h of exchange with NH_4Cl for all eight thin sections of palagonite, indicating that exchangeable B had been extracted. This method for extraction of exchangeable B should be applicable to thick or thin sections of sheet silicates and other clay-like materials, allowing calculation of exchangeable B content and $\delta^{11}B_{ex}$ using mass balance.

(4) The present study addressed calibration, matrix effects, and the removal of exchangeable B not equilibrated with the tetrahedral sites in palagonite. These sample-preparation procedures may now be applied to *in situ* SIMS microanalysis of B content and isotopic ratio in thin-section samples of palagonite by SIMS. Caution must be taken, however, to ensure that the composition of the palagonitized glass is similar to that of the reference material, as shown for the BB-1 glass used here to demonstrate that there are no matrix effects. Some compositional variations have been reported to cause matrix effects on B measurements, especially where large variations in Fe and Mg contents exist (Chaussidon and Jambon, 1994). The present study does not prove unambiguously the absence of matrix effects for all palagonites, but for the samples studied, significant trends which are greater than such possible

analytical artifacts were found. The matrix composition must be evaluated when measuring glasses. The present study demonstrated, however, that with attention to such details, meaningful measurements of the B composition of palagonite are possible.

ACKNOWLEDGMENTS

Dave Clague, Alicé Davis, Michelle Coombs, Mike Garcia, Don Thomas, and Jose Honnorez are thanked for providing some of the samples used in this study. Sveinn Jakobsson and Hjalti Franzson supported sample-collection fieldwork. This research was supported by NSF-EAR grant 0125666 as well as by the NSF-supported SIMS Facility and the Center for Solid State Science at Arizona State University. Klaus Franzreb is also thanked for providing technical support on the Cameca 3f SIMS. Two Editors in Chief (J.W. Stucki and M.A. Velbel) and three anonymous reviewers helped to improve the manuscript with thoughtful comments which are much appreciated.

REFERENCES

Bishop, J.L., Schiffman, P., and Southard, R. (2002) Geochemical and mineralogical analyses of palagonitic tuffs and altered rinds on pillow basalts in Iceland and applications to Mars. Pp. 371–392 in: *Volcano-Ice Interaction on Earth and Mars* (J.L. Smellie and M.G. Chapman, editors). Special Publication, **202**, Geological Society, London.

Brindley, G.W. and Brown, G. (1980) Crystal structures of clay minerals and their X-ray identification. Monograph **5**, Mineralogical Society, London.

Catanzaro, E.J., Champion, C.E., Garner, E.L., Malinenko, G., Sappenfeld, K.M., and Shields, W.R. (1970) Boric acid, isotopic, and assay standard reference materials, U.S. National Bureau Standards Special Publication, **260**, pp. 17–70.

Chaussidon, M. and Jambon, A. (1994) Boron content and isotopic composition of oceanic basalts: geochemical and cosmochemical implications. *Earth and Planetary Science Letters*, **121**, 277–294.

Crovisier, J.-L., Advocat, T., and Dussossoy, J.-L. (2003) Nature and role of alteration gels formed on the surface of ancient volcanic glasses (natural analogs of waste containment glasses). *Journal of Nuclear Materials*, **321**, 91–109.

Drief, A. and Schiffman, P. (2004) Very low temperature alteration of sideromelane in hyaloclastites and hyalotuffs from Kilauea and Mauna Loa volcanoes: implications for the mechanism of palagonite formation. *Clays and Clay Minerals*, **52**, 623–635.

Eggleton, R.A. and Keller, J. (1982) The palagonitization of limburgite glass – a TEM study. *Neues Jahrbuch für Mineralogie Monatshefte*, **7**, 321–336.

Fisher, R.V. and Schmincke, H.-U. (1984) *Pyroclastic Rocks*. Springer-Verlag, New York.

Hay, R.L. and Iijima, A. (1968a) Petrology of palagonite tuffs of Koko craters, Oahu, Hawaii. *Contributions to Mineralogy and Petrology* **17**, 141–154.

Hemming, N.G. and Hanson, G.N. (1992) Boron isotopic composition and concentration in modern marine carbonates. *Geochimica et Cosmochimica Acta*, **56**, 537–543.

Hervig, R.L. (1996) Analysis of geological materials for boron by secondary ion mass spectrometry. Pp. 789–803 in: *Boron Mineralogy, Petrology, and Geochemistry* (E.S. Grew and L.M. Anovitz, editors). Reviews in Mineralogy, **33**, Mineralogical Society of America, Washington, D.C.

Hervig, R.L., Moore, G.M., Williams, L.B., Peacock, S.M., Holloway, J.R., and Roggensack, K.R. (2002) Isotopic and elemental partitioning of boron between hydrous fluid and silicate melt. *American Mineralogist*, **87**, 769–774.

Hingston, F.J. (1964) Reactions between boron and clays. *Australian Journal of Soil Research*, **2**, 83–95.

Hoefs, J. (2004) *Stable Isotope Geochemistry*. Springer-Verlag, Berlin.

Jercinovic, M.J., Keil, K., Smith, M.R., and Schmitt, R.A. (1990) Alteration of basaltic glasses from north-central British Columbia, Canada. *Geochimica et Cosmochimica Acta*, **54**, 2679–2696.

Lerman, A. and Clauer, N. (2007) Stable isotopes in the sedimentary record. Pp. 1–55 in: *Treatise on Geochemistry*, **7** (H.D. Holland and K.K Turekian, editors). Elsevier, Amsterdam.

Moore, D.M. and Reynolds, R.C. (1991) *X-ray Diffraction and the Identification and Analysis of Clay Minerals*. Oxford University Press, Oxford, UK.

Palmer, M.R. and Swihart, G.H. (1996) Boron isotope geochemistry: an overview. Pp. 709–744 in: *Boron Mineralogy, Petrology, and Geochemistry* (E.S. Grew and L.M. Anovitz, editors). Reviews in Mineralogy, **33**, Mineralogical Society of America, Washington, D.C.

Pauly, B.D., Schiffman, P., Zierenberg, R.A., and Clague, D.A. (2011) Environmental and chemical controls on palagonitization. *Geochemistry Geophysics Geosystems*, **12**, paper number 2011GC003639.

Potts, P.J. (1987) *A Handbook of Silicate Rock Analysis*. Blackie, Glasgow, UK.

Rosner, M., Wiedenbeck, M., and Ludwig, T. (2008) Composition-induced variations in SIMS instrumental mass fractionation during boron isotope ratio measurements of silicate glasses. *Geostandards and Geoanalytical Research*, **32**, 27–38.

Schiffman, P. and Roeske, S. (2002) Electron microprobe analysis of minerals. Pp. 293–306 in: *Encyclopedia of Physical Sciences and Technology*, **5**, Elsevier, Amsterdam.

Schiffman, P. and Southard, R.J. (1996) Cation exchange capacity of layer silicates and palagonitized glass in mafic volcanic rocks: A comparative study of bulk extraction and *in situ* techniques. *Clays and Clay Minerals*, **44**, 624–634.

Schiffman, P., Walton, A.W., Thompson, N., and Watters, R.J. (2006) Hyaloclastite alteration and the slope stability of Hawaiian volcanoes: Insights from the Hawaiian Scientific Drilling Project's 3-km drill core. *Journal of Volcanology and Geothermal Research*, **151**, 217–228.

Singer, A. (1974) Mineralogy of palagonitic material from the Golan Heights, Israel. *Clays and Clay Minerals*, **22**, 231–240.

Sposito, G., Skipper, N.T., Sutton, R., Park, S.-H., Soper, A.K., and Greathouse, J.A. (1999) Surface geochemistry of the clay minerals. *Proceedings of the National Academy of Sciences, USA*, **96**, 3358–3364.

Stroncik, N.A. and Schmincke, H.-U. (2001) Evolution of palagonite: crystallization, chemical changes and element budget. *Geochemistry Geophysics Geosystems*, **2**, paper number 2000GC000102.

Tonarini, S., Pennisi, M., and Leeman, W.P. (1997) Precise boron isotopic analysis of complex silicate (rock) samples using alkali carbonate fusion and ion-exchange separation. *Chemical Geology*, **142**, 129–137.

Walton, A.W. and Schiffman, P. (2003) Alteration of hyaloclastites in the HSDP 2 Phase 1 Drill Core: (I) description and paragenesis. *Geochemistry Geophysics Geosystems*, **4**, paper number 2002GC000368.

Walton, A.W., Schiffman, P., and Macpherson, G.L. (2005) Alteration of hyaloclastites in the HSDP 2 Phase 1 Drill Core: 2. Mass balance of the conversion of sideromelane to palagonite and chabazite. *Geochemistry Geophysics*

Geosystems, **6**, paper number 2004GC000903.

Williams, L.B. and Hervig, R.L. (2005) Lithium and boron isotopes in illite-smectite: The importance of crystal size. *Geochimica et Cosmochimica Acta*, **69**, 5705–5716.

Williams, L.B. and Hervig, R.L. (2006) Crystal-size dependence of illite-smectite isotope equilibration with changing fluids. *Clays and Clay Minerals*, **54**, 531–540.

Williams, L.B., Hervig, R.L., Holloway, J.R., and Hutcheon, I. (2001) Boron isotope geochemistry during diagenesis: Part I. Experimental determination of fractionation during illitization of smectite. *Geochimica et Cosmochimica Acta*, **65**, 1769–1782.

Williams, L.B., Turner, A., and Hervig, R.L. (2007) Intracrystalline boron isotope partitioning in illite-smectite: Testing the geothermometer. *American Mineralogist*, **92**, 1958–1965.

Williams, L.B., Clauer, N., and Hervig, R.L. (2012) Light stable isotope microanalysis of clays in sedimentary rocks. Pp. 55–74 in: *Quantitative Mineralogy and Microanalysis of Sediments and Sedimentary Rocks* (P. Sylvester, editor). Short Course **42**, Mineralogical Association of Canada, Quebec.

Zhang, L., Chan, L.H., and Gieskes, J.M. (1998) Lithium isotope geochemistry of pore waters from Ocean Drilling Project Sites 918 and 919, Irminger Basin. *Geochimica et Cosmochimica Acta*, **62**, 2437–2450.

Zielinski, R.A. (1980) Stability of glass in the geologic environment: some evidence from studies of natural silicate glasses. *Nuclear Technology*, **15**, 197–200.

Zhou, Z. and Fyfe, W.S. (1989) Palagonitization of basaltic glass from DSDP site-335, LEG-37 – textures, chemical-composition, and mechanism of formation. *American Mineralogist*, **74**, 1045–1053.

(*Received 12 February 2011; revised 6 June 2014; Ms. 633; AE: J.W. Stucki*)

Clays and Clay Minerals, Vol. 62, No. 3, 235–242, 2014.

THE DISSOLUTION OF AMORPHOUS SILICA IN THE PRESENCE OF TROPOLONE UNDER ACIDIC CONDITIONS

MAYUMI ETOU[1], YUTAKA TSUJI[2], KENJI SOMIYA[3], YOSHIHIRO OKAUE[1], AND TAKUSHI YOKOYAMA[1,*]

[1] Department of Chemistry, Faculty of Science, Kyushu University, 6-10-1, Hakozaki, Higashi-ku, Fukuoka, 8128581, Japan
[2] Kurume National College of Technology, Komorino, Kurume, Fukuoka, 8308555, Japan
[3] JFE Engineering, Suehiro-cho, Tsurumi-ku, Yokohama, Kanagawa, 2308611, Japan

Abstract—Dissolution of amorphous silica or silicate is an important reaction to release silicic acid in natural water and this reaction is affected by several factors. The existence of a natural organic compound, tropolone, because of its abundance, is of particular importance. In the present study, the dissolution of amorphous silica in the presence of tropolone (HL) was investigated in an aqueous solution under acidic conditions. The dissolution is controlled by the reaction between silicic acid and tropolone ($Si(OH)_4 + 3HL + H^+ \rightleftharpoons SiL_3^+ + 4H_2O$), where the conditional formation constant $K = [SiL_3^+]/[Si(OH)_4][HL]^3[H^+]$). The solubility of amorphous silica in the presence of tropolone was significantly greater than that in pure water due to the formation of the Si-tropolonate complex in the solution. The acceleration of silica dissolution by tropolone depends on the reaction pH and tropolone concentration. The solubility of the amorphous silica in the tropolone solution at pH 1 was approximately ten times greater than in the 0.1 mol/dm^3 HCl used as a reference. This increase in the solubility correlates to a K value of the Si-tropolone complex at each pH. From the solubility experiments, the conditional formation constants (log K) of the Si-tropolonate complex at each reaction pH 1, 2, and 3 were 6.39, 5.88, and 5.77, respectively. The significant acceleration of the dissolution of amorphous silica by tropolone at pH 1 can be attributed to the large formation constant of the Si-tropolonate complex.

Key Words—Amorphous Silica Dissolution, Dissolution Rate Constant, Solubility, Tropolone.

INTRODUCTION

Silicon (Si) is the second most abundant element in the Earth's crust and exists as silicate, crystalline silica such as quartz, and amorphous silica. Although the form of Si in natural water depends on the pH, temperature, and coexisting compounds, Si typically dissolves as monosilicic acid ($Si(OH)_4$) in natural water due to the dissolution of silicate and silica. The dissolution reaction is expressed in equation 1 (Iler, 1979):

$$SiO_2 + 2H_2O \rightleftharpoons Si(OH)_4 \quad (1)$$

Previous studies of the dissolution of silica have been conducted on (1) the solubility of silica and (2) the dissolution rate of silica. The solubility of amorphous silica in water is only slightly dependent on pH within the range 2−8.5, and is ≈1.8 mM (50 ppm Si) at 25ºC (Iler, 1979). Kinetic analysis of the dissolution of amorphous silica (Plettinck *et al.*, 1994) revealed a well defined effect of pH on the dissolution rate, on both sides of a minimum rate at pH 2−3, in accord with the point of zero charge (pzc) of amorphous silica. From pH 2 to 8.5, silicic acid is present as neutral monosilicic acid ($Si(OH)_4$); on the other hand, $Si(OH)_4$ begins to dissociate H^+ with increasing pH above pH 8.5 to form a silicate ion (*e.g.* $SiO(OH)_3^-$). The solubility of amorphous silica between pH 2 and pH 8.5 is equal to the concentration of $Si(OH)_4$, while, above pH 8.5, it increases. The solubility above pH 8.5 corresponds to the sum of the concentrations of $Si(OH)_4 + SiO(OH)_3^-$ (silicate ions). Below pH 2, only a few studies on the solubility of amorphous silica have been conducted.

Based on the two independent research directions regarding the dissolution of silica, the effect of coexisting components on the dissolution of amorphous silica has also been investigated. Because silica and silicate are abundant, the effects of coexisting compounds such as metal ions and organic compounds on their dissolution have been investigated. The effect of organic compounds, in particular, has been investigated widely. Since the formation of etch pits in quartz grains in peat-bog groundwaters with high organic-compound concentrations was reported by Bennett and Siegel (1987), the influence of oxalic, acetic, lactic, and formic acids, which are produced by bacteria or fungi in the lithosphere, on the dissolution of amorphous silica has been investigated (Dandurand and Schott, 1987; Bennett *et al.*, 1988; Öhman *et al.*, 1991; Poulson *et al.*, 1997). Although the dissolution of amorphous silica or quartz is thought to be accelerated by such organic acids, Poulson *et al.* (1997) concluded that the oxalic acid has no effect on the dissolution of quartz. Recently, the effect of amino acid on the dissolution rate of amorphous silica

* E-mail address of corresponding author:
yokoyamatakushi@chem.kyushu-univ.jp
DOI: 10.1346/CCMN.2014.0620307

has also been investigated. Basic amino acids such as histidine, lysine, and arginine interact more with the negatively charged surface of amorphous silica than other amino acids and accelerate the dissolution of amorphous silica (Kawano and Obotake, 2007). In addition, those authors also reported the enhancement of dissolution of amorphous silica in the presence of bovine serum albumin and the functional molecules of basic amino acids (Kawano and Hwang, 2010a, 2010b). Although these basic amino acids can increase the dissolution rate of amorphous silica, the solubility of amorphous silica in the presence of amino acids has not been investigated. On the other hand, Tiron (disodium catechol-3, 5-disulfonate), a catechol derivative, can form a stable 1:3 Si-Tiron complex in solution and the solubility of amorphous silica in the Tiron solution can reach ~100 ppm (as Si), according to Bai *et al*. (2008). These results suggest strongly that the contribution of organic compounds that can interact with silicic acid (or a silica surface) can notably increase the Si concentration in natural water. To reveal the effects of organic compounds on the dissolution of amorphous silica, an investigation that combines both the equilibrium discussion and kinetic analysis is essential. In the present study, the focus was on tropolone (2-hydroxy-2,4,6-cycloheptarien-1-one, HL) as the organic compound because some derivatives of tropolone are abundant in more evolved plants (*e.g.* conifers such as cedar and pine). For example, *thujaplicine* (4-isoprophyl tropolone, *thpl*) has been found in many conifers and can be isolated from those trees as a cationic Si-*thpl* complex (Weiss and Herzog, 1978). Based on potentiometric titration and ^{29}Si nuclear magnetic resonance (NMR) measurements, tropolone has been reported to form a stable 1:3 Si-tropolonate complex under acidic conditions (Sjöberg *et al.*, 1985), though any investigation of the effect of tropolone on the dissolution of silica or silicate has been insufficient.

In addition to the solubility of amorphous silica in the presence of tropolone, the dissolution-rate constant of the amorphous silica in acidic conditions was also evaluated because the investigation is not viable other than in the presence of hydrogen fluoride.

EXPERIMENTAL METHODS

Materials

All reagents used were of analytical grade. All solutions were prepared with ultra pure water (Milli-Q Reference, Millipore). A Wako gel® C-200 for column chromatography (BET surface area: 450 m^2/g, 75−150 μm in size) was purchased from Wako Pure Chemical Industries, Ltd. (Osaka, Japan) as the source of amorphous silica. Prior to the dissolution experiment, the Wako gel was immersed in pure water (pH 5.5−5.6) and shaken for 5 h and then washed with ultra-pure water at least three times to remove any ultrafine particles. The tropolone was purchased from Tokyo Chemical Industry Co., Ltd (Tokyo, Japan). For the ^{29}Si NMR measurements, a sodium silicate solution prepared by dissolving ^{29}Si-enriched SiO_2 (98.7% ^{29}Si, Cambridge Isotope Laboratories, Inc. (Massachusetts, USA)) in the sodium hydroxide solution was used. Hydrochloric acid (HCl) (Wako Pure Chemical Industries, Ltd.) was used to adjust the pH.

Dissolution experiments

The dissolution experiment in the presence of tropolone was conducted not only for the determination of the solubility but also for the estimation of the dissolution rate constant. The 0.1 mol/dm^3 (M) tropolone solution (200 or 500 cm^3) was prepared by the dissolution of solid tropolone in water. The pH in the tropolone solution was adjusted to pH between 1 and 3 by adding HCl. Silica gel powder (2 or 5 g) was added to the tropolone solution and the suspended solution was shaken by a shaker (100 min^{-1}) at 30±0.2ºC. Aliquots of the suspended solution were taken at adequate intervals and filtered with a 0.45 μm membrane filter. The silicic-acid concentration in the filtrates was measured by inductively coupled plasma atomic emission spectroscopy (ICP-AES) (Optima 5300 DV, Perkin Elmer: Shelton, Connecticut, USA). The solubility of amorphous silica in HCl was used as a control. The effect of tropolone concentration on the dissolution of amorphous silica was examined by the same procedure − the amount of tropolone adsorbed on the surface of amorphous silica was measured by elemental analysis (Total Organic Carbon Analyzer TOC-V_E, Shimadzu, Japan).

NMR measurements

After the dissolution experiment, the ^{13}C NMR spectra for the filtrates were measured. The ^{13}C NMR spectra were recorded using a JEOL JNM-AL 400 FT NMR spectrometer (JEOL, Japan) with a 5 mm multinuclear probe head. All measurements were conducted at a resonance frequency of 100.40 MHz. The pulse delay and transients were 17.6 s and 17,000, respectively. Chemical shifts were recorded with respect to $Si(CH_3)_4$ (tetramethylsilane, TMS) using $C_6H_{15}NaO_3SSi$ (sodium 3-(trimethyl-silyl)-1-propanesulfonate, DSS) as a secondary liquid reference. The NMR measurements were carried out at room temperature.

To elucidate the effect of pH on the complexation between silicic acid and tropolone, the mixed solutions of silicic acid (1.8 mM) and tropolone (18 mM) were prepared at various pH values. ^{29}Si NMR spectra of the mixed solutions were also recorded using the same instrument as previously. This time, all measurements were conducted at a resonance frequency of 79.30 MHz. The pulse delay and transients were 30.0 s and 9000, respectively. Chemical shifts were recorded with respect to external TMS.

Electron-spray ionization mass spectroscopy (ESI-MS) measurements

Electron-spray ionization mass spectroscopy measurements were carried out to examine the stoichiometry of the Si-tropolonate complex. The sample solution contained 1.8 mM silicic acid and 18 mM tropolone at pH 1. The ESI-MS measurements were performed using a Waters Quattromicro API mass spectrometer in the positive ionization mode. The solutions were introduced into the spectrometer at a flow-rate of 2 μL/min. The operating conditions were as follows: capillary voltage 3.0 kV, sample cone voltage 50 V, RF lens 0 V, source temperature 120ºC, desolvation temperature 150ºC, cone gas flow rate 50 L/h, and desolvation gas flow rate 600 L/h.

RESULTS AND DISCUSSION

Formation of the Si-tropolonate complex under acidic conditions

The ^{29}Si NMR spectra of mixed solutions containing silicic acid (1.8 mM) and tropolone (18 mM) of pH 1−3 were measured (Figure 1) to reveal the complexation between silicic acid and tropolone under acidic conditions. The peak at −72 ppm is due to the free monosilicic acid ($Si(OH)_4$) and that at −141 ppm, to a 6-coordinated Si in the Si-tropolonate complex. This chemical shift is similar to that found by Sjöberg *et al.* (1985). The formation of the Si-tropolonate complex depends heavily on the reaction pH. To confirm the stoichiometry of the Si-tropolonate complex, a positive-mode ESI mass spectrum for the mixed solution was obtained (Figure 2). The concentration of silicic acid and tropolone in the sample solution was identical to that used for the ^{29}Si NMR measurement. The peak at *m/z* 121.1 was assigned to free protonated tropolone (H_2L^+). A dominant peak at *m/z* 393.1 corresponded to a Si-tropolonate complex. From the *m/z* value, the composition of this complex is a 1:3 Si-tropolonate complex.

The formation constant (log K) of the Si-tropolonate complex, which forms according to the following reaction (equation 2), was reported by Sjöberg *et al.* (1985):

$$Si(OH)_4 + 3HL + H^+ \rightleftharpoons SiL_3^+ + 4H_2O \quad (2)$$

$$K = [SiL_3^+]/[Si(OH)_4][HL]^3[H^+] \quad (3)$$

The formation constants of the Si-tropolonate complex (SiL_3^+) (log K (M^{-4})) were reported from potentiometric titration to be log K = 7.08±0.03 (Sjöberg *et al.*, 1985). In the present study, each conditional formation constant (log β (M^{-4})) was determined from the integrated ^{29}Si NMR spectra (Figure 1) at pH 1 and 2 and estimated to be 7.40 and 6.16, respectively.

Solubility of amorphous silica in the presence of tropolone

When the formation of a silicic acid−organic compound complex in aqueous solution is considered, the solubility of amorphous silica can be represented as the sum of the free $Si(OH)_4$ and the complex concentrations (equation 4).

$$2SiO_2 + 4H_2O + \text{ligand} \rightleftharpoons Si(OH)_4 + [Si(OH)_4\text{−ligand complex}] \quad (4)$$

Using this reaction, Tiron was found (Bai *et al.*, 2008) to form a Si-Tiron complex and can increase the solubility of amorphous silica at pH 6.

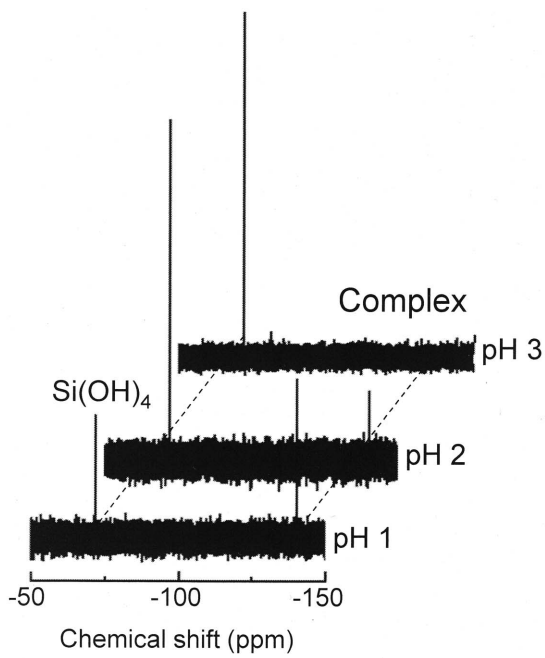

Figure 1. ^{29}Si NMR spectra of mixed solutions containing silicic acid (1.8 mM) and tropolone (18 mM) under acidic conditions. Notice that the horizontal scale is offset for each pattern for clarity.

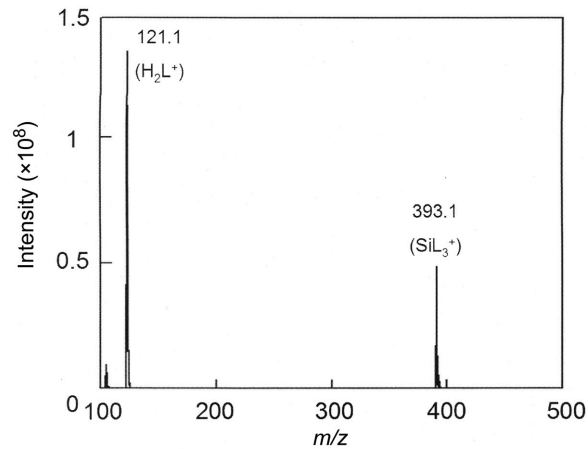

Figure 2. ESI-MS spectrum of a mixed solution containing silicic acid (1.8 mM) and tropolone (18 mM) at pH 1.

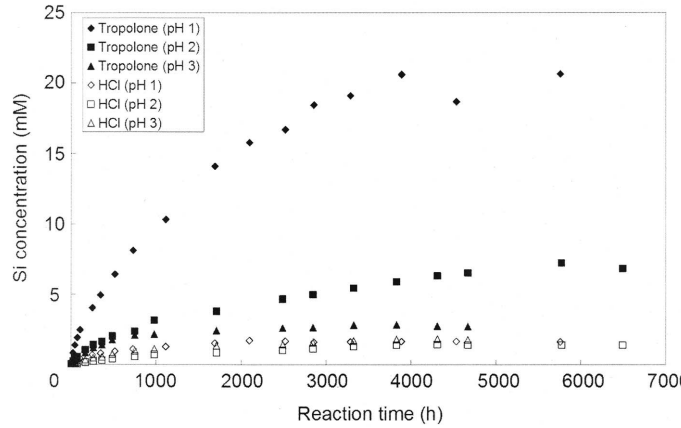

Figure 3. Time course of dissolution of amorphous silica in the presence of tropolone under acidic conditions. Initial tropolone concentration: 0.1 M; volume: 500 cm^3; silica gel powder: 5 g.

The time course of Si concentration during the solubility experiment in the presence of tropolone (Figure 3) revealed that tropolone increased the dissolution rate at all pH values and that the rate at pH 1 was much greater than at pH 2 or 3. The solubility was defined as the point at which the Si concentration in solution reached a constant value (Figure 3, Table 1). These findings also agree with the results from ^{29}Si NMR spectra of silicic acid and tropolone mixed solutions (Figure 1).

The possible formation of the Si-tropolonate complex (SiL_3^+) during the solubility experiments was probed using ^{13}C NMR spectroscopy of the filtrate. Results from the pH 1 treatment at equilibrium confirmed the formation of SiL^{3+} in solution. The ^{13}C NMR spectrum of the filtrate is shown in Figure 4. The peak prime symbol indicates a peak assigned to SiL^{3+} and the peak without the prime symbol indicates the free ligand. Integration of ^{13}C NMR peaks (total ligand concentration: 0.1 M) revealed that the molar ratio of $[ligand]_{free}$ to $[ligand]_{complex}$ was 1−1.3 at equilibrium and the calculated concentration of $[SiL_3^+]$ was 18.1 mM. Considering this molar ratio of ligand to the total silicic acid concentration (19.8 mM) at equilibrium, the calculated concentration of $[Si(OH)_4]$ in the solubility experiment at equilibrium was 1.7 mM. Therefore, at the end of this experiment, the concentration of monosilicic acid almost reached the solubility of amorphous silica. Because the sample solutions at pH 2 and pH 3 have a relatively low Si-tropolonate complex content compared with those at pH 1, the peak due to the Si-tolopolonate complex was not observed on the ^{13}C NMR spectra (not shown here). However, the formation of the Si-tropolonate complex should occur even at pH 2 and 3 because the dissolution of amorphous silica was accelerated. The ^{13}C NMR peak due to the complex was apparently not detected because of low sensitivity. In particular, the solubility in tropolone solution at pH 1 was approximately ten times greater than that of the 0.1 M HCl as control. The values of log β for the Si-tropolonate complex at each reaction pH were calculated using the solubility of amorphous silica in the presence of tropolone and are summarized in Table 1.

Basic amino acid increases the dissolution rate (according to Kawano and Obotake, 2007) by the formation of monodentate outer-sphere complexes on the surface of amorphous silica. The greater reactivity of

Table 1. The solubility and dissolution-rate constants of amorphous silica in the presence of tropolone under acidic conditions.

Reaction pH	Solubility of amorphous silica (mM)		Log β* of	Rate constants (k) (mM/min)	
	HCl system	Tropolone system	Si-tropolonate complex	HCl system	Tropolone system
1	1.67	19.8	6.39	4×10^{-4} (**r^2 = 0.9989)	3.7×10^{-3} (r^2 = 0.9733)
2	1.39	6.86	5.88	1×10^{-4} (r^2 = 0.9980)	1×10^{-3} (r^2 = 0.9995)
3	1.78	2.78	5.77	8×10^{-5} (r^2 = 0.9960)	5×10^{-4} (r^2 = 0.9985)

* Log β: conditional formation constant of Si-tropolonate complex calculated from the solubility of amorphous silica in tropolone solution.
** r^2: The correlation coefficient of each result in the kinetic analysis.

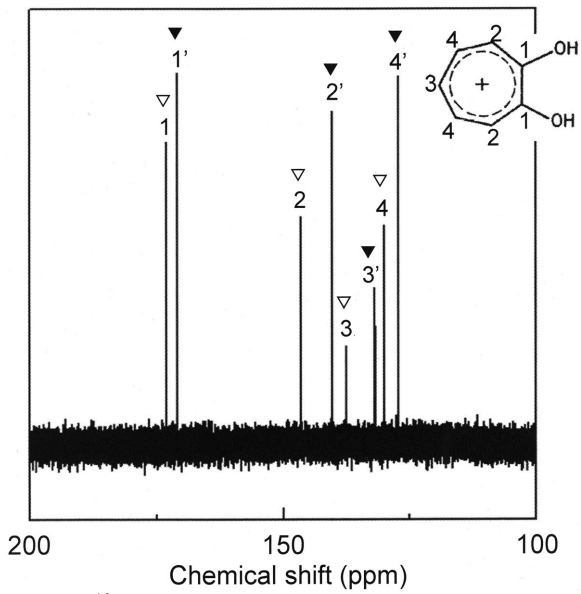

Figure 4. ^{13}C NMR spectrum of the filtrate after the solubility experiment at pH 1 (Figure 3). The number on each carbon atom in the molecular structure of tropolone in the figure indicates the chemical state of carbon atoms. The numbers with prime symbols indicate that the peaks are due to Si-tropolonate complex. The numbers without prime symbols indicate that the peaks are due to free tropolone.

such amino acids is due to the formation of cationic amino acid species (Kawano and Obotake, 2007). On the other hand, the adsorption of tropolone on the surface of amorphous silica was not observed. Therefore, the acceleration mechanism of tropolone is considered to be different from such amino acids. Because the pK_{a1} and pK_{a2} values of tropolone are –0.52 and 6.7, almost all of tropolone exists as HL under the present experimental condition and the adsorption of tropolone on the surface of amorphous silica did not occur as described above.

In addition, due to the relatively large formation constant of the Si-tropolonate complex in aqueous solution, the dissolved monosilicic acid can easily form a 1:3 Si-tropolonate complex and the concentration of monosilicic acid decreases to the lower concentration than the solubility of amorphous silica by the complexation. As a consequence, the dissolution reaction (equation 1) was accelerated. From the complexation reaction represented in equation 2, the H^+ concentration in the system is also important for the complexation between silicic acid and tropolone. Thus, strong pH dependence was observed.

The solubility of amorphous silica in Tiron solution can reach 100 ppm (as Si) due to the formation of stable 1:3 Si-Tiron complex, according to Bai *et al*. (2008). In addition, the conditional formation constant (log β) of the Si-Tiron complex was estimated to be ~0.3−0.6 (M^{-1}) (Bai *et al.*, 2011). The solubility of amorphous silica in tropolone solution was approximately six times greater than the result for Tiron due to the difference in the log β values between the Si-Tiron complex (log β: 0.3−0.6) and the Si-tropolonate complex (log β: 5.8−6.9) (see Table 1).

From a model calculation using the K value of SiL_3^+, Sjöberg *et al.* (1985) concluded that the acceleration of the dissolution of quartz and amorphous silica scarcely occurs at pH 2 and 3. However, in the present study, tropolone was revealed to accelerate dissolution of amorphous silica even at pH 2 and 3.

The dissolution of amorphous silica at pH 1 also depended on the tropolone concentration (Figure 5). When the concentration of tropolone was 0.001 M, the dissolution rate was similar to that of the HCl system used as a control, whereas the rate at 0.1 M was much greater.

Dissolution rate of amorphous silica in the presence of tropolone

A kinetic analysis was applied to the dissolution of amorphous silica in the presence of tropolone for the initial 5 h period (Figure 6). The analysis was performed using the method described by Bird *et al.* (1986). The calculation scheme is summarized briefly below. The equation for the dissolution kinetics of amorphous silica can be defined using equations 5 and 6 when the dissolution and deposition reactions are considered simultaneously as shown in equation 1.

$$(dC/dt)_{\text{forward}} = k_+(A/M) \quad (5)$$

$$(dC/dt)_{\text{backward}} = k_-C(A/M) \quad (6)$$

where C indicates the monosilicic acid concentration, t is reaction time, and k_+ and k_- are rate constants for the dissolution and deposition reactions of amorphous silica, respectively. The term A represents the surface area of the silica and M is the mass of the water. From equation 1,

$$K_{eq} = [Si(OH)_4]/\{[SiO_{2solid}][H_2O]^2\} \quad (7)$$

The activity coefficients for SiO_2 (solid) and H_2O were assumed to be unity and $(dC/dt) = 0$ was also assumed at equilibrium.

$$k_+/k_- = K_{eq} = C_{eq} \quad (8)$$

K_{eq} and C_{eq} represent the equilibrium constant and the equilibrium concentration (solubility), respectively. If (A/M) can be constant during the dissolution experiments, from equations 5 to 8, then equation 9 is obtained ($k_+(A/M)$ was replaced by N)

$$-C_{eq}\ \ln[1-C/C_{eq}] = Nt \quad (9)$$

By analyzing the results of the initial 300 min (Figure 6), a linear relationship was obtained (Figure 7). The dissolution-rate constant in each solution, k_+, can be estimated from the slope of each straight line. The dissolution-rate constants for each experimental condition and the correlation coefficient of each result (r^2) are summarized in Table 1.

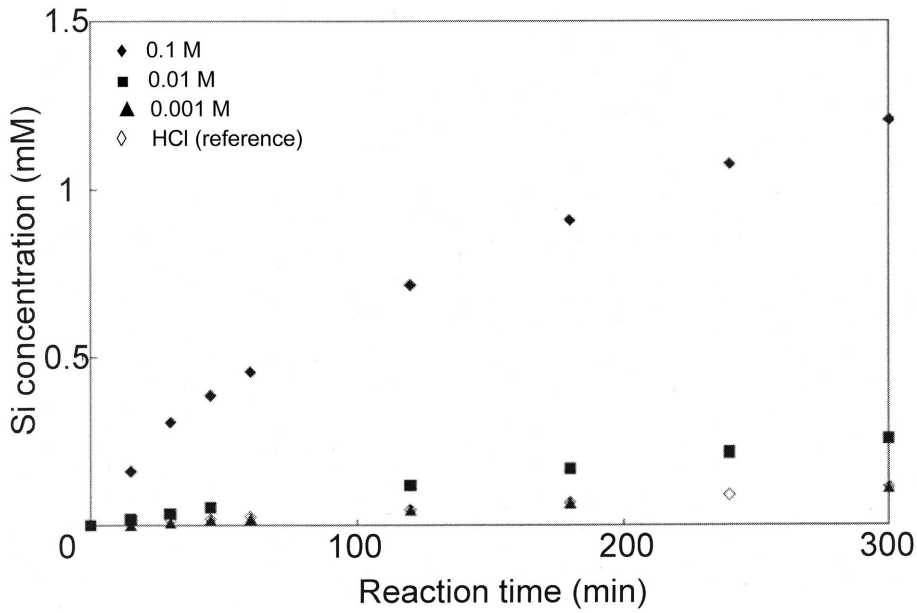

Figure 5. Effect of tropolone concentration on the dissolution of amorphous silica at pH 1. Initial tropolone concentrations: (◆) 0.1 M, (■) 0.01 M, and (▲) 0.001 M. (◇) HCl was used as a control. Volume: 200 cm^3; silica gel powder: 2 g; reaction time: 300 min.

Characteristically, in HCl systems, the dissolution-rate constant at pH 1 was greater than those at pH 2 and 3. The dissolution rate of amorphous silica at pH 1 was reported by Plettinck *et al*. (1994) to be larger than those at pH 2 and pH 3, which is in agreement with the present results. The dissolution rate of quartz increases with activity of the proton at 0 < pH < 3 (Pokrovsky *et al*., 2006), which suggests the adsorption of H^+ on the mineral surface, leading to polarization of Si−O bonds and detachment of the silicon atom from the structure. In the present study, a protonated silanol group ($SiOH_2^+$) may be formed by the adsorption of H^+ at pH 1 and the electron density of the silica framework may decrease and the detachment of a silicon atom from the structure may occur more easily. As well as the solubility of amorphous silica, the dissolution rate constant in the

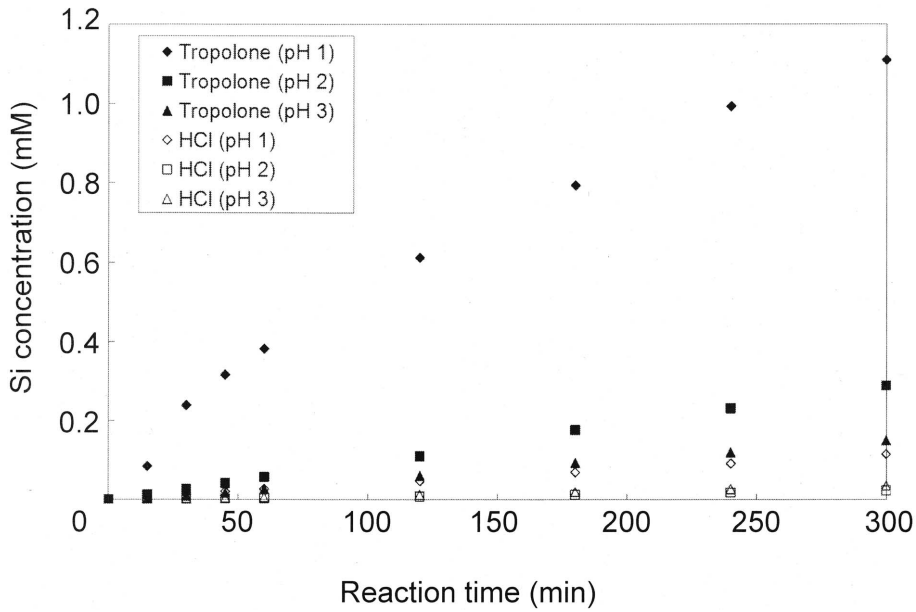

Figure 6. Time course of dissolution of amorphous silica during an initial 300 min in the presence of tropolone under acidic conditions. Initial tropolone concentration: 0.1 M; volume: 200 cm^3; silica gel powder: 2 g; reaction time: 300 min.

tropolone solution was greater than those in the HCl system and have a clear pH dependence. The dissolution rate constant in tropolone solution was ~10 times greater than that of the reference. In addition, the plots (◆ in Figure 7) deviate slightly from the straight line. Approximately 3−5% of protonated tropolone (H_2L^+) species exist at pH 1 and H_2L^+ can interact more easily with silicic acid because of positive charge. At the early stage of dissolution of amorphous silica at pH 1, therefore, the reaction between silicic acid and H_2L^+ may have an effect on the dissolution of amorphous silica. Considering the percentage of H_2L^+ species involved, this effect is less than that of the reaction between silicic acid and HL.

Tropolone and its derivatives are naturally abundant in leaves of conifers. The present results suggest strongly that the Si concentration in natural water can increase due to the organic compound which can interact with silicic acid through the formation of Si-organic compound complexes. From the present results, natural organic compounds such as humic substances which exist abundantly in nature may release Si in nature.

CONCLUSIONS

The dissolution of amorphous silica in the presence of tropolone under acidic conditions was investigated. The dissolution was strongly accelerated over that in HCl due to the formation of the Si-tropolonate complex in the solution. The solubility of amorphous silica in the tropolone solution was approximately ten times greater than that in HCl (the control) at pH 1. According to NMR measurements, the increase in the Si concentration at equilibrium is due to the formation of a Si-tropolonate complex. The effect of tropolone on the dissolution of amorphous silica depends heavily on the reaction pH and tropolone concentration. The solubility in the tropolone solution was significantly greater than that in solutions of other organic compounds such as Tiron which can form Si complexes in solution. The significant acceleration of the dissolution by tropolone is due to the large formation constant of the Si-tropolonate complex. These results suggest strongly that the acceleration of the dissolution of silica through the interaction between the organic compounds and silicic acid is an important

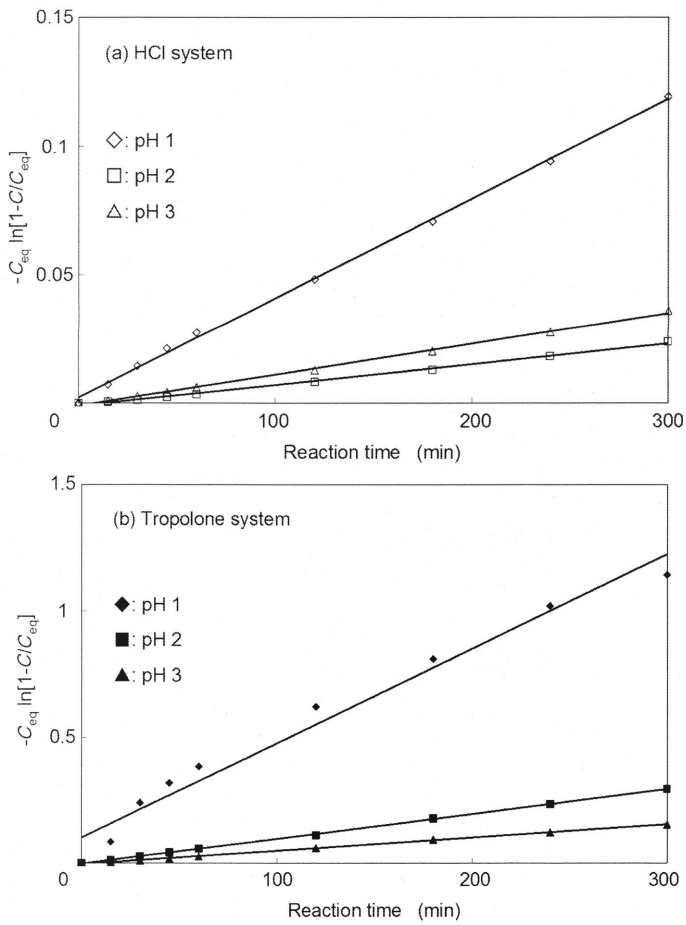

Figure 7. Relationship between $-C_{eq}\ln(1-C/C_{eq})$ and reaction time obtained from Figure 6. C: monosilicic acid concentration at time t; C_{eq}: solubility of amorphous silica in each system (see Table 1).

reaction for release of silica as silicic acid into solution in the lithosphere.

REFERENCES

Bai, S., Tsuji, Y., Okaue, Y., and Yokoyama, T. (2008) First detection of a silicic acid complex with a catechol derivative under natural conditions. *Chemistry Letters*, **37**, 1168–1169.

Bai, S., Tsuji, Y., Okaue, Y., and Yokoyama, T. (2011) Complexation of silicic acid with tiron on aqueous solution under near natural conditions. *Journal of Solution Chemistry*, **40**, 348–356.

Bennett, P.C. and Siegel, D.I. (1987) Increased solubility of quartz in water due to complexation by dissolved organic compounds. *Nature*, **326**, 684–687.

Bennett, P.C., Melcer, M.E., Siegel, D.I., and Hassett, J.P. (1988) The dissolution of quartz in dilute aqueous solutions of organic acids at 25ºC. *Geochimica et Cosmochimica Acta*, **52**, 1521–1530.

Bird, G., Boon, J., and Stone, T. (1986) Silica transport during stream injection into oil sands 1. Dissolution and precipitation kinetics of quartz: new results and review of existing data. *Chemical Geology*, **54**, 69–80.

Dandurand, J. and Schott, J. (1987) New data on the solubility of amorphous silica in organic compound-water solutions and a new model for the thermodynamic behavior of aqueous silica in aqueous complex solutions. *Journal of Solution Chemistry*, **16**, 237–256.

Iler, R.K. (1979) *The Chemistry of Silica: Solubility, Polymerization, Colloid and Surface Properties and Biochemistry*. Wiley, New York.

Kawano, M. and Hwang, J. (2010a) Enhancement of dissolution rates of amorphous silica by interaction with bovine serum albumin at different pH conditions. *Clays and Clay Minerals*, **58**, 272–279.

Kawano, M. and Hwang, J. (2010b) Influence of guanidine, imidazole, and some heterocyclic compounds on dissolution rates of amorphous silica. *Clays and Clay Minerals*, **58**, 757–765.

Kawano, M. and Obokata, S. (2007) The effect of amino acids on the dissolution rates of amorphous silica in near-neutral solution. *Clays and Clay Minerals*, **55**, 361–368.

Öhman, L., Nordin, A., Sedeh, I.F., and Sjöberg, S. (1991) Equilibrium and structural studies of silicon(IV) and aluminium(III) in aqueous solution. 28. Formation of soluble silicic acid-ligand complexes as studied by potentiometric and solubility measurements. *Acta Chemica Scandinavica*, **45**, 335–341.

Plettinck, S., Chou, L., and Wollast, R. (1994) Kinetics and mechanisms of dissolution of silica at room temperature and pressure. *Mineralogical Magazine*, **58A**, 728–729.

Pokrovsky, O.S., Golubev, S.V., and Mielczarski, J.A. (2006) Kinetics evidence of the existence of positively charged species at the quartz–aqueous solution interface. *Journal of Colloid and Interface Science*, **296**, 189–194.

Poulson, S.R., Drever, J.I., and Stillings, L.L. (1997) Aqueous Si-oxalate complexing, oxalate adsorption onto quartz, and the effect of oxalate upon quartz dissolution rates. *Chemical Geology*, **140**, 1–7.

Sjöberg, S., Ingri, N., Nenner, A., and Öhman, L. (1985) Equilibrium and structural studies of silicon(IV) and aluminium(III) in aqueous solution. 12. A potentiometric and ^{29}Si-NMR study of silicon tropolonates. *Journal of Inorganic Biochemistry*, **24**, 267–277.

Weiss, A. and Herzog, A. (1978) Isolation and characterization of a silicon-organic complex from plants. Pp. 109–125 in: *Biochemistry of Silicon and Related Problems* (G. Bendz and I. Lindqvist, editors). Plenum, New York.

(*Received 5 December 2013; revised 22 April 2014; Ms. 823; AE: H. He*)